INFERENCE FROM MODELLING THE CHEMODYNAMICAL EVOLUTION OF THE MILKY WAY DISC

JAN RYBIZKI

Printed in October 2015
Cover picture: *Several Circles*, Wassily Kandinsky (1926)

Dissertation
submitted to the
Combined Faculties of Natural Sciences and Mathematics
of the Ruperto-Carola-University of Heidelberg, Germany
for the degree of
Doctor of Natural Sciences

Put forward by
Jan Rybizki
born in: Rüdersdorf
Oral examination: December 8th, 2015

INFERENCE FROM MODELLING THE CHEMODYNAMICAL EVOLUTION OF THE MILKY WAY DISC

Referees: Prof. Dr. Andreas Just
Prof. Dr. Norbert Christlieb

ZUSAMMENFASSUNG - RÜCKSCHLÜSSE AUS DER MODELLIERUNG DER CHEMODYNAMISCHEN ENTWICKLUNG DER MILCHSTRASSENSCHEIBE

In der vorliegenden Arbeit werden die anfängliche Massenfunktion (IMF) von Feldsternen und Parameter zur chemischen Anreicherung der Milchstraße, unter Verwendung von Bayesscher Statistik und Modellrechnungen, hergeleitet.
Ausgehend von einem lokalen Milchstraßenmodell [Just and Jahreiss, 2010] werden, für verschiedene IMF-Parameter, Sterne synthetisiert, die dann mit den entsprechenden Hipparcos [Perryman et al., 1997] (Hipparcos) Beobachtungen verglichen werden. Die abgeleitete IMF ist in dem Bereich von 0.5 bis 8 Sonnenmassen gegeben durch ein Potenzgesetz mit einer Steigung von -1.49 $\pm$ 0.08 für Sterne mit einer geringeren Masse als 1.39 $\pm$ 0.05 $M_\odot$ und einer Steigung von -3.02 $\pm$ 0.06 für Sterne mit Massen darüber.
Im zweiten Teil dieser Arbeit wird die IMF für Sterne mit Massen schwerer als 6 $M_\odot$ bestimmt. Dazu wurde die Software *Chempy* entwickelt, mit der man die chemische Anreicherung der Galaktischen Scheibe simulieren und auch die Auswahl von beobachteten Sternen nach Ort und Sternenklasse reproduzieren kann. Unter Berücksichtigung des systematischen Effekts der unterschiedlichen in der Literatur verfügbaren stellaren Anreicherungstabellen ergibt sich eine IMF-Steigung von -2.28 $\pm$ 0.09 für Sterne mit Massen über 6 $M_\odot$.
Dies zeigt, dass die von der chemischen Entwicklung abgeleitete IMF, ähnlich wie die Ergebnissen aus hydrodynamischen Simulationen der Milchstraße, für hohe Massen der Salpeter [1955] IMF entspricht. Aufgrund der geringen Anzahldichte von massereichen Sternen kann dies durch Sternzählungen nur schwer nachgewiesen werden.

ABSTRACT - INFERENCE FROM MODELLING THE CHEMODYNAMICAL EVOLUTION OF THE MILKY WAY DISC

In this thesis, the field star Initial Mass Function (IMF) and chemical evolution parameters for the Milky Way (MW) are derived using a forward modelling technique in combination with Bayesian statistics.
Starting from a local MW disc model [Just and Jahreiss, 2010], observations of stellar samples in the Solar Neighbourhood are synthesised and compared to the corresponding volume-complete observational samples of Hipparcos [Perryman et al., 1997] (Hipparcos) stars. The resulting IMF, derived from observations in the range from 0.5 to 8 $M_\odot$, is a two-slope broken power law with powers of -1.49 $\pm$ 0.08 and -3.02 $\pm$ 0.06 for the low-mass slope and the high-mass slope, respectively, with a break at 1.39 $\pm$ 0.05 $M_\odot$.
In order to constrain the IMF for stars more massive than 8 $M_\odot$, a fast and flexible chemical enrichment code, *Chempy*, was developed, which is also able to reproduce spatial and stellar population selections of observational samples. The inferred high-mass slope for stellar masses above 6 $M_\odot$ is -2.28 $\pm$ 0.09, accounting for the systematic effects of different yield sets from the literature.

This shows that constraints from chemical modelling, similarly to hydrodynamical simulations of the Galaxy, demand a Salpeter [1955] high-mass index. This is hard to recover from star count analysis given the rareness of high-mass stars.

OVERVIEW AND PUBLICATIONS

In this thesis, the mass distribution of stars and the evolution of elements in the Milky Way (MW) are investigated. For this, physically motivated models are constructed, their input parameters are changed, and the outcome is compared to observational data of discriminative power. This forward modelling approach is combined with the concept of Bayesian inference. Central to this technique is the construction of a likelihood function in order to sample the posterior probability distribution, which is performed by means of Markov Chain Monte Carlo (MCMC) methods.
The thesis is organised in the following way. The first chapter is an introduction to the evolution of the MW, with a focus on the processes governing the synthesis of the chemical elements.
The statistical methodology will be introduced in chapter 2. The first example of Bayesian model inference, where the true distance of a star will be inferred from a parallax measurement, is taken in great detail from Bailer-Jones [2015]. This leads to the question of determining stellar number densities in a specific volume, which will be discussed in the second part of chapter 2. The ideas presented in section 2.2.3 have been published in Just et al. [2015] with a contribution from the author.
In chapter 3, the Initial Mass Function (IMF) parameters are inferred from Solar Neighbourhood stars, using a local MW disk model. Most of this chapter has been published in Rybizki and Just [2015].
In chapter 4, a chemical evolution model of the local MW disc is presented and important model parameters, constraining the high-mass IMF, the infall and the SuperNova of type Ia (SN Ia), are inferred from abundances of Solar Neighbourhood stars. Section 4.3 of this chapter contains results, which are submitted as conference proceedings [Just and Rybizki, 2015].
The thesis will be concluded with a summary and a concise outlook.

ACKNOWLEDGEMENTS

First and foremost I would like to thank Prof. Andreas Just for his confidence in my work and his guidance. The generous financial support and the freedom to ponder ideas are very much appreciated as well as his positive supervision style.
I am much obliged to PD Coryn Bailer-Jones and Dr. Ewan Cameron for their help with statistical questions, which I came across frequently, and for nurturing my fascination of Bayesian statistics.
For most enjoyable lunch breaks and for partaking in my science and non-science related challenges I wish to express my deep gratitude to Dr. Robert Schmidt. His presence made the Astronomisches Rechen-Institut (ARI) feel more like a home for me.
I am very grateful to Prof. Norbert Christlieb for readily agreeing to referee this thesis. Furthermore I wish to thank Prof. Eva Grebel and Prof. Luca Amendola for willingly joining my examination committee.
I also want to mention the highly valued advice and helpful strategic planning from my thesis committee consisting of Prof. Eva Grebel, Dr. Glenn van de Ven and Prof. Andreas Just.
Special thanks go to PD Christian Fendt who coordinated the International Max Planck Research School (IMPRS) activities that formed a sociable community out of our IMPRS generation.
At ARI, I would like to thank Hendrik Heinl for caring about the social activities and for his support especially towards the end of my thesis writing.
For numerous entertaining lunch breaks I want to thank Dr. Markus Demleitner and Aksel Alpay who also helped me to master the computationally expensive MCMC simulations.
In the same respect Dr. Peter Schwekendiek and Sven Weimann always provided me with helpful computing advice and maintained the excellent *Perseus* machine.
I want to thank the whole ARI administration, especially mentioning Martina Buchhaupt for thoroughly taking care of my administrative issues and Stefan Leitner for mocking me for my poor hand crafting skills.
I enjoyed the scientific and non-scientific exchange with Dr. Corrado Boeche with whom I could lament about the intriguing complexity of selection functions.
Last but not least I would like to thank Alex Hygate, Carolin Wittmann, Clio Bertelli, PD Coryn Bailer-Jones, Dr. Corrado Boeche, Daniel Haydon, Dr. Frederik Schönebeck, Dr. Gernot Burkhardt, Hendrik Heinl, Peter Zeidler, Reza Moetazedian, Dr. Robert Schmidt, Timo Hirscher and Tina Gier for proof reading this thesis and for making the ARI a sociable workspace.

My PhD project was funded by SFB 881 *The Milky Way System*.
I would also like to acknowledge financial support from the Heidelberg Graduate School of Fundamental Physics and the IMPRS which allowed me to participate in several interesting summer schools and useful workshops giving me the opportunity to learn from the best in the field and be an active part of the international community.

CONTENTS

LIST OF FIGURES

LIST OF TABLES

ACRONYMS

2MASS The Two Micron All Sky Survey at IPAC [Skrutskie et al., 2006] . . . 36

ABC Approximate Bayesian Computation . . . 30

AGB Asymptotic Giant Branch star (late evolutionary state of stars with masses $0.8\,M_\odot < m < 8\,M_\odot$) . . . 93

AGN Active Galactic Nuclei (a super massive black hole sitting in the center of a galaxy and accreting gas) . . . 6

AMR Age Metallicity Relation . . . 42

APOGEE APO Galactic Evolution Experiment [Alam et al., 2015] . . . 93

AVR Age Velocity-dispersion Relation . . . 42

BAO Baryonic Acoustic Oscillations . . . 6

BB Big Bang . . . 5

BD Brown Dwarf . . . 58

Besançon model Besançon Galaxy model (first version from Robin et al. [2003] updated in Robin et al. [2012] latest update in Czekaj et al. [2014] and Robin et al. [2014]) . . . 38

Besançon B default model B of Czekaj et al. [2014] . . . 55

BF Bayes Factor (used for Bayesian model comparison) . . . 62

BH Black Hole . . . 73

CDM Cold Dark Matter . . . 65

CEM Chemical Enrichment Model . . . 43

Chabrier 03 Chabrier [2003] . . . 70

CMB Cosmic Microwave Background . . . 5

CMD Colour-Magnitude Diagram . . . 44

CNO cycle Carbon-Nitrogen-Oxygen cycle (main fusion reaction to form helium from hydrogen for stars above 1.3 $M_\odot$ and with an initial abundance of at least carbon) 9

CNS Catalogue of Nearby Stars - version 5 (used here but not yet published) is an update of version 4 [Jahreiss and Wielen, 1997] . . . 42

CO Carbon-Oxygen White Dwarf (remnant of Asymptotic Giant Branch stars) . . . 11

COROT COnvection ROtation and planetary Transits [Baglin and COROT Team, 1998] (asteroseismic mission) . . . 20

Δmag Δmagnitude (magnitude difference of stars in a binary system) . . . 47

DM Dark Matter (which comes in different flavours but we assume it to be 'cold') . . . 6

DTD Delay Time Distribution (the time it takes a statistical ensemble of different SuperNova of type Ia (SN Ia) progenitors to go supernova) . . . 73

FH 06 Flynn et al. [2006] disc mass model . . . 58

Gaia Gaia [Lindegren et al., 2008] (astrometric satellite mission) . . . 93

GES Gaia-ESO [Gilmore et al., 2012] (spectroscopic follow-up of Gaia) . . . 93

GALAH GALactic Archeology with HERMES [Anguiano et al., 2014] (spectroscopic survey) . . . 19

Galaxia Galaxia [Sharma et al., 2011] (a tool to synthesise observations) . . . 42

GCS Geneva Copenhagen Survey [Nordström et al., 2004] . . . 44

HB Horizontal Branch . . . 10

Hipparcos Hipparcos [Perryman et al., 1997] satellite, also the derived astrometric catalogue. Revised parallaxes from van Leeuwen [2007] . . . 91

HN HyperNova (Feedback process of stars with mass > 20 $M_\odot$) . . . 71

HRD Hertzsprung-Russel Diagram (a plot of effective temperature vs. the luminosity of a star, which is the theoretical counterpart of the CMD) . . . 9

IR infrared (electromagnetic waves with $1000\mu\text{m} > \lambda > 0.7\mu\text{m}$) . . . 65

IMF Stellar Initial Mass Function . . . 93

IRA Instantaneous Recycling Approximation . . . 68

ISM InterStellar Medium . . . 68

JJ-model MW disc model [Just and Jahreiss, 2010] . . . 42

Kepler Kepler [Borucki et al., 1997] (asteroseismic mission) . . . 20

KTG 93 Kroupa et al. [1993] . . . 70

ΛCDM Lambda Cold Dark Matter (cosmological standard model) . . . 6

LF Luminosity Function . . . 41

MCMC Markov Chain Monte Carlo (an iterative sampling technique) . . . 91

MS Main Sequence . . . 41

MW Milky Way . . . 93

NGP North Galactic Pole . . . 41

NIR Near-InfraRed (photons with a wavelength of $0.8\,\mu\text{m} < \lambda < 2.5\,\mu\text{m}$) . . . 15

NS Neutron Star (a type of stellar remnant) . . . 8

pp Proton-Proton chain (main fusion reaction to form helium from hydrogen for stars below $1.3\,M_\odot$) . . . 9

PS 1 Pan-STARRS 1 (the Panoramic Survey Telescope & Rapid Response System [Hodapp et al., 2004]) . . . 36

PDF Probability Density Function . . . 91

PDMF Present-Day stellar Mass Function . . . 42

PN Planetary Nebula (the end stage of an Asymptotic Giant Branch (AGB) star) . . . 57

paper I Just and Jahreiss [2010] . . . 41

paper II Just et al. [2011] . . . 41

quasar Quasi-stellar object (the radiation of an active galactic nuclei from an early galaxy looking like stellar point sources with peculiar spectra) . . . 7

RAVE The Radial Velocity Experiment [Steinmetz et al., 2006] (spectroscopic survey) . . . 19

RC Red-Clump (overdensity in the giant branch of the CMD) . . . 91

RGB Red Giant Branch . . . 9

r-process Rapid-neutron-capture-process element (produced in massive stars and in neutron star merger) . . . 8

SDSS Sloan Digital Sky Survey [York et al., 2000] . . . 41

SEGUE Sloan Extension for Galactic Understanding and Exploration [Yanny et al., 2009] (low-resolution spectroscopic survey of $\approx 240,000$ stars) . . . 17

SFR Star Formation Rate . . . 67

SFH Star Formation History . . . 71

SGP South Galactic Pole

s-process Slow-neutron-capture-process element (produced in Asymptotic Giant Branch and also in massive stars) . . . 11

SN Ia SuperNova of type Ia . . . 91

SN II SuperNova of type II . . . 69

SMBH Super Massive Black Hole (sitting in the center of massive galaxies and sometimes being the engine of an Active Galactic Nuclei (AGN)) . . . 8

SSP Simple Stellar Population . . . 44

Tycho 2 Tycho 2 catalogue [Hoeg et al., 2000] . . . 42

VMag Absolute V magnitude . . . 43

Vmag Apparent V magnitude . . . 19

WD White Dwarf . . . 74

ZAMS Zero-Age Main Sequence (star begins to burn hydrogen) . . . 10

Part I

INTRODUCTION

"Wenn man in dem unermeßlichen Raume, darinn alle Sonnen der Milchstrasse sich gebildet haben, einen Punkt annimmt, um welchen durch, ich weiss nicht was vor eine Ursache, die erste Bildung der Natur aus dem Chaos angefangen hat; so wird daselbst die größte Masse, und ein Körper von der ungemeinsten Attraction, entstanden sein, der dadurch fähig geworden, in einer ungeheuren Sphäre um sich alle in der Bildung begriffene Systeme zu nöthigen, sich gegen ihn, als ihren Mittelpunkt, zu senken, und um ihn ein gleiches System im Ganzen zu errichten, als derselbe elementarische Grundstoff, der die Planeten bildete, um die Sonne im Kleinen gemacht hat."

Immanuel Kant (1755)
Universal Natural History and Theory of Heaven (p. 102)

Figure 1: Milky Way from Earth, credit: ESO/S. Brunier

1 THE MILKY WAY GALAXY

1.1 ETYMOLOGY

The ancient Greeks referred to the dim band visible across the sky on a clear night, depicted in figure 1, as *galaxias kuklos* (γαλαξίας κύκλος), meaning *milky circle*. Today, the word *Galaxy* is still a synonym for *Milky Way*, which is a translation from the Latin *via lactea*, itself coming from the Greek *galaxias*. The Greek mythology explains the glowing appearance of the Milky Way with spilled milk from goddess Hera's breast, who pushed back Heracles, not being her own son, but from her husband Zeus and the mortal woman Alkmene. Zeus had put the baby to sleeping Hera's breast, in order for his child to gain divine powers as illustrated in Jacopo Tintoretto's oil painting on canvas, shown in figure 1.1.

Figure 1.1: *The Origin of the Milky Way*, Jacopo Tintoretto (ca. 1575 - 1580)

1.2 HISTORY

Greek philosophers like Democritus already speculated about the nature of the Milky Way (MW), proposing that it is composed of a huge number of distant stars. Actual proof had to wait until the invention of the Dutch telescope (from Greek τηλεσκόπος, teleskopos "far-seeing"), and Galileo Galilei improving its magnifying power one year later in 1609. Observing the MW, he realised that it was composed of a huge number of individual stars, which was published in the pamphlet *Sidereus Nuncius* in 1610.
Immanuel Kant, more renown for his work as philosopher, speaks of the MW as a gravitationally bound rotating system, in his treatise *Universal Natural History and Theory of Heaven* from 1775, building up on the work by Thomas Wright. From the regular elliptical shape of some 'nebulous' stars, Kant also derived that they should be distant *galaxies* on their own. Evidence for this correct assumption accumulated in the early 20th century. The period-luminosity relation for Cepheid variable stars was found by Leavitt [1908] and

Galaxy is written capitalised if referring to the MW and lowercase, when referring to external galaxies

Figure 1.2: Milky Way-like galaxy NGC 6744. Single stars on this image are not part of NGC 6744, but foreground stars from our own Galaxy. Credit: ESO

was calibrated by Shapley [1918], using parallactic motions[1]. This relation was used by Hubble [1925], who could determine the period of cepheids in the Andromeda nebula with the 2.5 meter Hooker telescope at the Mount Wilson Observatory, thus placing them well outside the sphere of the MW. After presenting these findings, the idea of the MW being a galaxy among others was generally accepted, although already Slipher [1917] had inferred from the radial velocity measurements of nebulae that they should have extragalactic origin, and also Curtis [1917] had come to the same conclusion from apparent magnitudes of novae associated with nebulae.

The term nebulae *is no longer referring to* galaxies *but to interstellar gas or dust instead*

Nowadays, the MW is believed to be a barred spiral galaxy, similar to the one depicted in figure 1.2. Due to the fact that we can only observe the current evolutionary state of our Galaxy from its inside, the formation history and actual structure are not well constraint and still a matter of ongoing research, which this thesis would like to contribute to.
In order to give an overview over the present-day knowledge of the MW, we need to place it within the evolution of the Universe, before painting a more detailed picture of its substructure.

1.3 COSMOLOGY

The basis for the development of models describing the evolution of the Universe was set by Einstein [1915], when he published his field equations and the theory of general relativity, describing gravitational processes comprehensively, e.g. by the idea of spacetime being curved by matter and energy. In the following years Friedman [1922]; Lemaître [1927]; Robertson [1929]; Walker [1935] independently studied a set of homogeneous and isotropic models for the evolution of the Universe, which would expand (or contract), when applied to Einstein's field equations. Lemaître [1927] was the first to conclude that the increas-

1 Harley Shapley used the period-luminosity relation to measure the distribution of globular clusters within the MW and rightly located the Solar system in the outer regions of our Galaxy. During the *Great Debate* in 1920 he was an opponent of the idea of nebulae being galaxies like the MW.

ing recessional velocity of observed galaxies with distance is due to the expansion of the Universe [Livio, 2011]. With more data at hand, Hubble [1929] found a linear relationship between the redshift[2] of an object and its distance. Consequently, if going back in time the whole Universe must have started from a hot and dense state [Lemaître, 1931], which is why these universe models were later termed *Big Bang* cosmology.
This theory was widely accepted when the predicted signature of radiation decoupling from matter[3] was serendipitously found by Penzias and Wilson [1965] and identified by Dicke et al. [1965] as the Cosmic Microwave Background (CMB), with an almost perfect black body radiation. The anisotropies in the CMB were indeed so small, that pure-*baryonic* universe models could hardly explain the formation of galaxies [Peebles and Yu, 1970; Sunyaev and Zeldovich, 1970]. Already earlier Zwicky [1933] had found, when studying the Coma galaxy cluster, that a large amount of dark matter was necessary to explain the observed internal velocity dispersion when applying the virial theorem. It was not until Rubin and Ford [1970] rigorously analysed the galactic rotation curve of the Andromeda galaxy that dark matter became a topic of active research. Peebles [1982] could reconcile the low CMB anisotropies with the Big Bang (BB) cosmology assuming that a large mass fraction of the Universe is composed by dark matter. Dark matter was further constraint to be *cold* by Davis et al. [1985], whose simulations showed that the cosmological structure formation could only be explained if the velocity distribution of dark matter particles was already non-relativistic in the early Universe. The discovery of the predicted CMB anisotropy with the COBE satellite [Smoot et al., 1992] lent further strong evidence to dark matter.

baryons are interacting with all fundamental forces, i.e. gravitationally, strongly, weakly and especially electromagnetically and are therefore visible, in contrast to dark matter, which only interacts gravitationally and maybe weakly

The expansion rate of BB models is governed by the matter and radiation density, the curvature of space and the cosmological constant Λ, which was originally introduced by Einstein [1917] to obtain a static Universe from his field equations. Λ can be interpreted as the *energy density of vacuum space* that exerts a negative pressure, thus driving space apart. The *curvature* of the Universe seems to be *zero*[4], so that only the matter and radiation density are counteracting the dark energy. Since space, and therefore the total vacuum energy is growing, but the matter content of the Universe stays the same, the expansion rate should be accelerated, which was confirmed by SuperNova of type Ia (SN Ia) observations of Riess et al. [1998] and Perlmutter et al. [1999] and was awarded with the Nobel Prize in 2011.

vacuum energy density is also called dark energy

Although on scales larger than $\sim 100\,M$*pc* the matter distribution in the Universe seems to be homogeneous and isotropic, on the scales of Galaxy clusters and smaller, considerable structure can be found, which must have originated from primordial density fluctuations, growing non-linearly through gravitation. To set the initial conditions for this phenomenon and, more importantly, to account for the CMB being nearly constant over the full sky and also the flatness of space, an elegant explanation was proposed and developed by Guth [1981]; Linde [1982, 1983]; Albrecht et al. [1982] and is referred to as *inflation*. It was a short period, right after the BB, in which the inflaton field dominated and inflated

1 pc is approximately 3.26 *light-years or* $3,1 \times 10^{16}$ *m*

2 The light, being send out by an object moving away from us, is red-shifted due to the Doppler shift. This can be superimposed on the redshift caused by the expansion of the Universe. These two causes of redshift can be observationally distinguished [Davis and Lineweaver, 2004].

3 When the expanding Universe cools and its electrons and protons become bound in neutral hydrogen, radiation is not constantly scattered by electrons and can travel freely.

4 A universe with zero curvature is called flat, meaning that space is Euclidean.

the microscopic Universe together with its quantum fluctuations, to macroscopic scales. To date, the described Lambda Cold Dark Matter (ΛCDM) model with inflation is the simplest cosmological model able to explain the bulk of observational evidence, among which the most spectacular is probably the mapping of the small anisotropies of the CMB onto the Baryonic Acoustic Oscillations (BAO) of the galaxy distribution in the Universe [Eisenstein et al., 2005]. Together with the precise distance measurement of standard candles at high redshift [Freedman et al., 2001], all the parameters of this model can be well determined [Planck Collaboration, 2015]. Traces of the structure and evolution of the Universe are also found in weak lensing signals [Mandelbaum et al., 2013] and in the *Lyman-α forest* [Borde et al., 2014], giving us independent measurements to verify the ΛCDM model.

Lyman-α forest is a spectroscopic trace of interstellar hydrogen, seen in objects with high redshift

Since baryons form structure within the Cold Dark Matter (CDM) halos, physical feedback processes of baryonic matter, such as supernova explosions of stars or jets from Active Galactic Nuclei (AGN) complicate the picture, because the inferred mass function of galaxies will not be an exact, downscaled representation of the CDM halo mass function. Hydrodynamical simulations that are based on the ΛCDM model, and include baryonic feedback processes reproduce the observable Universe in an increasingly accurate way. Still, deviations between observations and simulations exist, for example the *missing satellite problem* [Klypin et al., 1999]. It is not clear whether this is a problem in the cosmological model, in the prescription of physical feedback processes, or (but less likely) in the observations. For the missing satellite problem, it might be solved by decreasing the assumed virial mass of the MW [Wang et al., 2012] or by satellite halos, being stripped off their baryons [Simon and Geha, 2007]. Based on these discrepancies, a few alternative theories have been put forward [Kroupa, 2012; Famaey and McGaugh, 2012], but generally these are not seriously challenging the overwhelming evidence for the ΛCDM model, such that we assume this cosmology for the purpose of this thesis.

How can such a diverse structure, like the MW, differentiate out of such a simple model? The answer lies in the interplay of baryons with the gravitational force of the CDM and hierarchical structure growth. The structure of today's Universe started from tiny fluctuations in the CDM density distribution, which grew gravitationally and hierarchically (through mergers and accretion) to form CDM halos on different scales, the biggest of which are just about able to withstand cosmic expansion. At the same time, baryons (able to cool faster than Dark Matter (DM) due to radiative cooling) could settle deep into the potential wells of the DM halos and thus form stars and galaxies. Since the gravitational collapse is anisotropic, tidal forces lead to the distribution of angular momentum, which can produce disc-like structures and will leave dynamical imprints. The feedback processes from stars and AGNs will regulate star formation and the build-up of structure. Its effect depends on the baryonic mass available, on the mass of the surrounding DM halo, and on the halo environment [Dressler, 1980].

Before coming to the description of the present-day picture of the MW, we will introduce the concepts of the matter cycle of the Universe, which will give us an understanding of the element synthesis thus providing a powerful tool to analyse the MW and its evolution.

1.4 ELEMENTAL SYNTHESIS AND STELLAR EVOLUTION

The production of chemical elements, of which the world around us consists, took almost 8 Gyr, when our Solar system formed. Imprints of the evolution of our Universe, as well as the formation history of our Galaxy, can be deduced from the elemental abundances. We will find that the nucleosynthesis is strongly entwined with the evolution of stars and the ending of their lives. Historically von Weizsäcker [1937], Bethe [1939] and the seminal Burbidge et al. [1957] developed an understanding of nuclear fusion in stars. A good overview is given in Ryan and Norton [2010].
To trace the elemental synthesis, we need to go to the beginning of our Universe, right after the BB. A good overview and the historical development of cosmological nucleosynthesis are given in Weinberg [2008], with Gamow [1946], Hayashi [1950] and Alpher et al. [1953] laying the foundations.

1.4.1 PRIMORDIAL NUCLEOSYNTHESIS

In the ΛCDM framework, the first elements condensated out of the cooling plasma of the expanding Universe. One second after the BB, the temperature of the Universe was below 10^9 K and protons could no longer be transformed into neutrons via weak interaction. Therefore the neutron to proton ratio dropped, which is one parameter determining the final elemental abundance. From ten seconds to about three minutes the temperature allowed neutrons and protons to fuse into deuterium and helium. Because of the high binding energy of helium and no stable nuclei with mass number five and eight, only light elements up to a *mass number* of seven could form. In stars, usually the triple-α process would overcome this barrier, but the density was not high enough for three-body reactions and also the time scale too short. In the end, 76 % of the mass was in hydrogen and 24 % in Helium, with traces of deuterium, tritium, helium-3 and small amounts of beryllium- and lithium-isotopes. Left-overs of neutrons, that did not find a reaction partner, decayed away, together with beryllium and tritium, fixing the primordial elemental composition. Since element abundance measurements of very early intergalactic gas has become feasible from Quasi-stellar object (quasar) spectra [Kirkman et al., 2003], primordial element abundances are a further constraining observational test for ΛCDM.

mass number of an element is the added number of neutrons and protons it consists of

1.4.2 FIRST STARS

For a long period of time, the Universe expands and its plasma cools. 380,000 yr after the BB, neutral hydrogen forms and the thermal radiation runs freely, for the first time, producing the CMB. As already outlined in the previous section, the baryons settle as proto-galactic clouds in overdense DM regions, which grow non-linearly from tiny anisotropies to a filamentary structure. Those proto-galactic gas clouds are immense and contract, so that the gas in their inner cores clumps, heats up and produces pressure to resist gravitational collapse. Radiative cooling is necessary, for further compression of the gaseous clumps. At the same time, angular momentum needs to be dissipated away, for the contraction to proceed, forming accretion discs, until a runaway collapse can form the first stars. They are supposed

to have higher masses than present-day stars, since line cooling via hydrogen and helium is less efficient than *metal-* or dust-cooling, so that higher Jeans masses [Jeans, 1902] are required. These stars are purely hypothetical[5], because yet no population III stars, as the first stars with no metals are called, have been observed. This is probably due to their high masses, resulting in very short (on the order of $3 - 5$ Myr) lifetimes[6]. Indeed, they must have been extremely heavy, compared to present-day stars, with masses between 100 and 1000 $M_\odot$ of pure hydrogen and helium and also with high rotational velocities, giving them special properties. Some of the first stars might have been so heavy during their formation, that they collapsed directly into a Black Hole (BH), forming the seed for the first Super Massive Black Hole (SMBH), powering the first quasars [Larson, 2000].

metals are all elements heavier than helium

iron-peak elements are formed during the last burning stage in nuclear statistical equilibrium, where nuclei with the highest binding energy per nucleus are favoured (Ti, V, Cr, Mn, Fe, Co, Ni, Cu, Zn)

These heavy population III, stars would have fused elements up to the *iron peak* in their inner cores, after which their energy source, delaying the gravitational pull, runs dry. This is the star's end stage, when it consists of successive layers of different burning products from hydrogen, helium at the surface over carbon, neon, oxygen, silicon up to iron in the core. With the fading pressure, provided by the fusion, the core contracts over the limit of electron degeneracy[7], loosing energy via photodisintegration and electron-capture (also called neutronization) and then approaching Neutron Star (NS) densities, which suddenly stops the contraction. Most of the infalling outer layers is rebounded and expelled into the InterStellar Medium (ISM) during this event called SuperNova of type II (SN II) [Ryan and Norton, 2010, Chapter 7.1].

α-elements are all stable elements, that can be build up from ^{4}He nuclei (C, O, Ne, Mg, Si, S, Ar, Ca)

The interstellar gas is mainly enriched with *α-elements*, a bit of iron-peak elements, together with traces of heavier elements, which use the explosion energy and the abundant neutrons to produce Rapid-neutron-capture-process (r-process) elements, from iron seed nuclei, in an endothermic nuclear reaction. The cores of the stars will end as stellar remnants, which can be either NSs or BHs.

1.4.3 REIONIZATION

These first stars, with their intense radiation, are reionizing the ISM and ending, together with the igniting galactic machinery, the dark ages of the Universe. Since the gas is less dense, than during recombination, the opaqueness of the Universe decreases. The view onto the first galaxies is disclosed, and they are observable from a redshift of about $z \approx 7$ [Mortlock et al., 2011]. The first stars are believed to have formed around $150 - 400$ Myr, also depending on the strength of the overdensity in that region of the Universe. The abundance pattern of the oldest observed stars, could have come from only one single SN II event, giving us insight on the properties of the first stars [Frebel et al., 2005; Chiappini et al., 2011; Keller et al., 2014].

metallicity is the metal mass fraction, with the Sun having an approximate value of about 1.4 %

With the ISM metallicity increasing and the distribution of gas getting more inhomogeneous, the mass range of stars of the upcoming generations, goes down and is assumed to be between $0.08\,M_\odot < m < 150\,M_\odot$. The number distribution of stars being born, is

5 What we know of population III stars, comes from hydrodynamical simulations and from abundances of very old stars, that are assumed to be the second generation of stars.

6 If they fragmented, which might not have been possible during formation, low-mass population III stars could have survived until the present day.

7 In very densely packed electron gas, the Pauli exclusion principle prohibits the overlapping of electrons in the same quantum state.

called Initial Mass Function (IMF) and is a stochastic average, well described by a lognormal or broken power-law at small masses and a steep power-law at high masses, making massive stars comparatively rare. Depending on the overall mass and to a lesser degree also on the helium mass fraction and the metallicity, the stellar evolution can be quite different and we will trace it and the contribution towards the chemical evolution from small- to high-mass stars. Beside the mass, the helium fraction and the metallicity, also rotation, binarity and elemental abundances will have an effect on the evolution and the feedback of a star.

1.4.4 LOW-MASS STARS

The lower mass limit, $0.08\,M_\odot$, for stars is determined by the heat and pressure that is generated in the core of a compact object, consisting mainly of hydrogen and helium, which needs to be high enough to start the Proton-Proton (pp)-chain. In objects smaller than about $0.08\,M_\odot$, called Brown Dwarf (BD), the temperature needed for fusion is not reached, because of the onset of electron degeneracy, prohibiting a further increase in temperature (for the same reasons the lower mass limit for helium burning in stars is $0.5\,M_\odot$). Up to about $0.8\,M_\odot$, stars remain on the Main Sequence (MS), meaning that they quiescently burn hydrogen in their core, for longer than a *Hubble time*. From a matter-cycle point of view, these low-mass stars are a sink, binding material in them and not contributing by releasing newly formed elements. Stars above $0.3\,M_\odot$ will enter the Red Giant Branch (RGB) phase, which will be described in the next subsection.

Hubble time is the inverse of the Hubble parameter, $H_0 = 67.80 \pm 0.77\,\frac{km}{s}Mpc^{-1}$ [Planck Collaboration, 2015], which describes the expansion rate of the Universe. The inverse is the time, when a constant expansion would have started, which is a simple approximation for the age of the Universe, $H_0^{-1} = 14.4\,Gyr$ and only slightly off the fiducial value of $t_0 \approx 13.8\,Gyr$

Most of the formed stars are actually low-mass stars. Since the radiation pressure from photons, released by nuclear fusion, equates the gravitational pull and this hydrostatic equilibrium is highly temperature- and therefore mass-dependent, low-mass stars, contrary to high-mass stars, lead quiescently dim and long lives. This leads to the effect, that when looking at a stellar population, most of its mass will be contained in low-mass stars and most of its light will be emitted by a few, very bright high-mass (and also evolved) stars.
The main reaction powering a star on the MS changes with mass. Up to about $1.3\,M_\odot$ the pp chain dominates. In more massive stars the Carbon-Nitrogen-Oxygen cycle (CNO cycle), using C, N and O as catalysts, becomes more efficient in turning hydrogen into helium (though population III stars would not have had this option). Independent of the initial composition of these three catalyst elements, the CNO cycle will alter their abundances in the core, which will have an influence on the nucleosynthesis of intermediate-mass stars.

1.4.5 INTERMEDIATE-MASS STARS

1.4.5.1 Asymptotic Giant Branch

Stars with masses between $0.8\,M_\odot$ and $8\,M_\odot$ are heavy enough to use up the hydrogen fuel in their inner cores within a Hubble time. When around 10 % of the star's hydrogen has been turned into helium, it leaves the MS. Since the core is full of helium, but not yet hot enough to burn it, hydrogen will fuse in a shell around the core, leading to an expansion of the whole star, though the luminosity stays the same. This results in the cooling of the photosphere, moving the star horizontally across the Hertzsprung-Russel Diagram (HRD), as can be traced in figure 1.3. Until it reaches the Hayashi-limit, where the increase of the

outer convection zone[8], inhibits further cooling and marks the end of the subgiant branch and the beginning of the RGB.

The core keeps growing , increasing its temperature and connectedly the efficiency of the

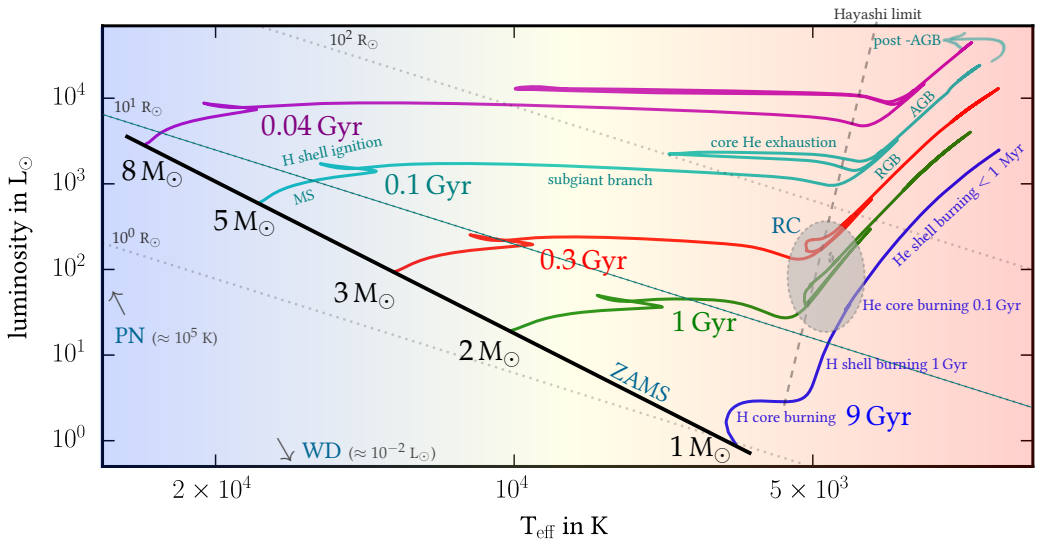

Figure 1.3: Hertzsprung-Russel diagram with stellar effective surface temperature in Kelvin on the x-axis and luminosity in Solar luminosity on the y-axis. The evolutionary tracks of stars in the range of $1\,M_\odot$ to $8\,M_\odot$ and with a sub-Solar metallicity of $Z = 0.01$ from Bressan et al. [2012] are shown, beginning with their Zero-Age Main Sequence (ZAMS). The end of the MS is marked with the colour-coded age of the corresponding track. This is where the contraction of the core heats the surface, until the ignition of the hydrogen burning shell cools it again, resulting in the zigzag for stars heavier than $2\,M_\odot$. Timescales of the different fusion processes are indicated for the $1\,M_\odot$ track. Different phases of the stellar evolution are shown for the $5\,M_\odot$ track. The area of the Red-Clump (RC) is indicated, as well as the position of Planetary Nebula (PN) and White Dwarf (WD), which are outside of this diagram. In dashed grey the Hayashi limit is indicated and in dotted grey the stellar radii are indicated qualitatively. Main features of this figure are taken from Ryan and Norton [2010, Fig. 4.5, 5.5, 6.3].

hydrogen burning shell, thereby increasing the luminosity and the radius of the star. For stars with around Solar mass the shell burning only ignites while already on the RGB (see $1\,M_\odot$ stellar evolutionary track in figure 1.3). Once the core reaches 10^8 K, a temperature high enough to ignite helium burning[9], the core will increase, lowering the energy output of the hydrogen burning shell, which leads to an overall contraction of the star. The position in the HRD of the quiescent phase of helium burning is called Red-Clump (RC), for metal-rich stars (*population I*), and Horizontal Branch (HB) for metal-poor stars (*population II*). Stars of mass lower than $2\,M_\odot$ will have a completely degenerate core, before starting helium burning, so that the fusion ignites in a degenerate gas, leading to the so called *helium flash*, increasing the energy output of the core by several orders of magnitude. More massive stars will have a smoother transition into the helium burning phase and also move further blue-wards, as their cores are non-degenerate, which decreases their radius, resulting in a hotter surface.

population I & II stars was termed by Baade [1944]

8 Eventually the convection can go so deep, that signatures of the hydrogen fusion, like decreased $^{12}C/^{13}C$ and C/N ratios, as well as depleted lithium and beryllium abundances, can be exposed at the surface of the star. This effect is called first dredge-up and needs to be taken into account when interpreting stellar spectra.

9 To turn helium into carbon, via the triple-α process, and also helium and carbon into oxygen.

Once helium is depleted in the core, a similar process to the first ascend of the RGB will happen, now with two shells, one burning hydrogen and one burning helium. That again drives an expansion of the star, taking a similar route in the HRD, only in a much shorter period of time and now called Asymptotic Giant Branch (AGB) phase. With the outer layer getting convective again, a second thermal dredge-up takes place (but only in stars heavier than $\approx 3.5\,M_\odot$), increasing the helium and nitrogen abundances and decreasing the carbon and oxygen abundance in the photosphere of the star. Once the helium shell used up its fuel (increasing the Carbon-Oxygen (CO) core) and the hydrogen shell becoming the major energy source, the AGB star starts pulsing thermally. This happens, because the star switches consecutively from hydrogen to helium fusion, with the hydrogen shell producing new fuel for the helium shell to re-ignite. The back and forth of burning layers results in strong convective movements between the two shells and can also bring material to the outer layers, which is referred to as third dredge-ups. These can further increase the helium abundance and will also bring freshly synthesised carbon and Slow-neutron-capture-process (s-process) elements to the surface. s-process elements are produced during these pulses, when iron seeds *grow* to heavier elements, via successive neutron-capture under moderate flux and β-decay. Neutrons are mainly provided from the $^{13}C + {}^{4}He \rightarrow {}^{16}O + n$ reaction, fuelled by the convective mixing. In AGB stars the main s-process produces heavy elements from strontium up to lead. There is also a *weak* s-process occurring in massive stars, after their helium- and carbon-burning, producing elements beyond iron up to yttrium.
The thermal pulses of the AGB phase become stronger each time, increasing the probability of moving material to the surface of the star. Due to the increased luminosity and molecules forming in the outer layers, strong stellar winds expel almost all of the envelope of the AGB star into the ISM, contributing to the chemical enrichment. The contracting CO-core becomes hotter and starts to ionize the surrounding material, upon reaching $10^4\,K$, which illuminates the Planetary Nebula (PN). The star moves blue-wards in the HRD, following the post-AGB arrow in figure 1.3, until it leaves the boundary of the figure, with the PN position indicated at the bottom left. The electron-degenerate remnant has a typical mass range of $0.5\,M_\odot$ to $1.2\,M_\odot$, is called CO-White Dwarf (WD) and will slowly radiate its thermal energy away. This is called WD cooling sequence, which also exceeds the figure limits and is indicated in the bottom left.
The evolution timescales of stars are strongly mass-dependent, as can be seen from their MS-lifetimes in figure 1.3. The relative durations of subsequent burning phases are also written for the $1\,M_\odot$ evolutionary track, which shows that a star spends most of its life on the MS. Stars with $8\,M_\odot$ have a MS lifetime of about 40 Myr and stars of $0.8\,M_\odot$ have one of 13 Gyr, which distributes the feedback from intermediate-mass stars over a long time.

1.4.5.2 SuperNova of type Ia

Another very important mechanism, especially for the iron production, is supposed to occur mainly in binary systems of intermediate-mass stars. There are two main progenitor models for SN Ia, depending on the number of CO-WDs involved. They are called *single-* or *double-degenerate* channel. For the former, the primary star is already an electron-degenerate CO-WD and the secondary starts donating material to the other, most likely because it enters the RGB phase. The mass of the WD will exceed the *Chandrasekhar mass*, $m \approx 1.38\,M_\odot$, igniting a thermonuclear runaway of carbon burning, which was first proposed by Hoyle and Fowler [1960] as a possible origin for SN Ia. In the latter case, the two stars are already

Chandrasekhar mass *is the maximum stellar mass that can be supported by degenerate electron pressure [Chandrasekhar, 1931]*

CO-WDs and spiral into each other, loosing angular momentum due to gravitational waves. When they coalesce, they exceed the Chandrasekhar limit and explode as a SN Ia. A successful model, reproducing the observed abundances, was calculated by Nomoto et al. [1984] using C-deflagration[10] and refined by Iwamoto et al. [1999]. It synthesises around 0.27 $M_\odot$ of silicon to calcium elements and 0.21 $M_\odot$ of carbon to aluminium (with 0.14 $M_\odot$ of oxygen). Iron-peak elements make up 0.90 $M_\odot$, with 0.75 $M_\odot$ in the form of ^{56}Ni, subsequently decaying to iron, giving the SN Ia light curves their characteristic shape. Chemical evolution models predict that around 30 % – 50 % of the overall iron in the Galaxy is produced from SN Ia.
The two progenitor models of SN Ia also have different Delay Time Distribution (DTD) functions, depending on the stellar evolution and the angular momentum loss. A mix of both functions is usually assumed in chemical evolution models, with a peak at approximately 1 Gyr.

1.4.6 HIGH-MASS STARS

Stars more massive than 8 $M_\odot$ retain enough mass during hydrogen- and helium-burning in order to ignite subsequent fusion processes, though up to a mass of 11 $M_\odot$, the core mass is not sufficient to fuse all elements up to iron. These stars will end their lives as oxygen-neon-magnesium WDs, with typical masses between 1.2 $M_\odot$ and 1.4 $M_\odot$.
Cores of stars with an initial mass heavier than 11 $M_\odot$ will exceed the Chandrasekhar mass limit and are able to fuse iron-peak elements, in nuclear statistical equilibrium at the end of their lives. With the energy source ceasing, a core-collapse supernova, SN II, will ignite, as already outlined in section 1.4.2. This enriches the ISM, mainly with synthesised α-elements, a bit of iron-peak elements and r-process-elements, leaving behind a NS or a stellar-mass BH.

1.4.7 CHEMICAL ENRICHMENT – A SIMPLE MODEL

The elemental feedback from massive stars occurs on the order of $\sim$ 10 Myr after their formation, enriching the ISM via SN II on relatively short time scales. Intermediate mass stars, on the other hand, take on the order of $\sim$ 100 Myr for AGB feedback or $\sim$ 1,000 Myr for SN Ia explosions. Since the synthesised elements differ for each process, the signature of the *delayed* enrichment can be detected in the chemical composition of subsequent stellar generations.
When talking about elemental abundances, there are two choices of how to communicate those, either by mass or by abundance. The composition of the Solar photosphere in mass fraction for example is $X_\odot = 73.9\,\%$ hydrogen, $Y_\odot = 24.69\,\%$ helium and $Z_\odot = 1.41\,\%$ metals using abundance determinations from Lodders et al. [2009]. The most abundant metals are oxygen $Z_{O,\odot} = 0.63\,\%$, carbon $Z_{C,\odot} = 0.22\,\%$, neon $Z_{Ne,\odot} = 0.17\,\%$ and iron $Z_{Fe,\odot} = 0.12\,\%$, already making up 80 % of all the metals in mass.
The observables in spectroscopic analysis are more related to number ratios of different elements. That is why observers usually express abundances via the elements logarithmic relative number ratio to hydrogen:

$$A(\text{Element}) = \log_{10}\left(\frac{N_{\text{Element}}}{N_H}\right) + 12. \tag{1}$$

10 The flame speed of the explosion propagating with subsonic speed.

Oxygen for example has an abundance of $A(O)_\odot = 8.73$, meaning that for every oxygen atom there are $1,862$ hydrogen atoms in the photosphere of the Sun. To relate the abundance to the mass fraction, we need to multiply each atom by its nucleon number, $m_H = 1$ for hydrogen and $m_O = 16$ for oxygen:

$$\frac{N_{O,\odot} m_O}{N_{H,\odot} m_H} = m_O 10^{A(O)_\odot - 12} = \frac{16}{1,862} = \frac{Z_{O,\odot}}{X_\odot}. \tag{2}$$

Abundances of other stars are usually given in the *bracket* notation, which is given in units of *dex*, with the Sun as reference

$$[Fe/H] = A(Fe) - A(Fe)_\odot \quad \left(\simeq \log_{10} \left(\frac{Z_{Fe}}{Z_{Fe,\odot}} \right) \right). \tag{3}$$

dex means decimal exponential *and if a star has a [Fe/H] of* -1 *(or* -2*) then its iron atoms are 10 (or 100) times less abundant than in the Sun*

This is the iron abundance relative to Solar (with the equation in brackets only being exact for stars that have hydrogen mass fraction similar to Solar, $X_\odot = 0.739$, which is a good approximation for most of the stars). Since iron lines are easy to observe, [Fe/H] is often used to indicate the metallicity of a star.

As an illustrative example for the signatures of chemical evolution, which can be traced by stellar elemental abundances, we will now consider the time-dependence of the oxygen to iron ratio

$$[O/Fe] = [O/H] - [Fe/H] \tag{4}$$

in the Galactic ISM.
Neither of those elements is produced during the primordial nucleosynthesis. After a short eruptive period of first stars - which we do not consider -, the Galaxy settles and forms new stars at a - more or less - constant rate. The feedback from the SN II, of short-lived massive stars, consists mainly of α- and iron-peak-elements, producing a constant oxygen to iron ratio of about $[O/Fe] = 0.5$. Substituting equation 3 in equation 4, we can calculate the corresponding mass fraction.

$$0.5 = \log_{10} \left(\frac{Z_O}{Z_{O,\odot}} \right) - \log_{10} \left(\frac{Z_{Fe}}{Z_{Fe,\odot}} \right) \Leftrightarrow \frac{Z_O}{Z_{Fe}} = 10^{0.5} \frac{Z_{O,\odot}}{Z_{Fe,\odot}} \tag{5}$$

With the Solar ratio being $\frac{Z_{O,\odot}}{Z_{Fe,\odot}} \approx 5$, it follows that $\frac{Z_{O,SN\,II}}{Z_{Fe,SN\,II}} \approx 16$ in SN II feedback, and equivalently $\frac{N_{O,SN\,II}}{N_{Fe,SN\,II}} \approx 56$.
With some time delay, the SN Ia start exploding, with iron being their bulk contribution to the chemical enrichment. In fact, from section 1.4.5.2 we know that $\frac{Z_{O,SN\,Ia}}{Z_{Fe,SN\,Ia}} \approx \frac{1}{5}$. This decreases the oxygen to iron abundance asymptotically towards the Solar value, $[O/Fe] = 0$, and produces a *knee* in the $[O/Fe]$ over $[Fe/H]$ distribution. The onset of the *knee* occurs at higher $[Fe/H]$ values for larger systems, as they produce more SN II and can retain most of their ejecta (contrary to smaller systems like dwarf galaxies). Since AGB feedback is not significantly altering the oxygen to iron ratio in the ISM, α-enhancement can be used as an age indicator for stars.

α-enhancement is measured from the abundance of an α-element or an average of several α-elements relative to iron, e.g. [O/Fe]

What follows is a list of issues that complicate this simple model and the interpretation of chemical abundance data in general:

- The relative abundance of intermediate- to high-mass stars is not fully constrained nor its dependence on metallicity and environmental effects.

- The exact feedback from various enrichment processes is not known and they vary with stellar mass, metallicity, binary evolution and rotation.
- The DTD of SN Ia is not precisely known and might also vary with metallicity and environment.
- Neither the Star Formation History (SFH) nor the available gas mass at a given time (infall, outflow, gas at start) is well constrained.
- The dynamics of stars and gas need to be considered.
- The Galactic gravitational potential is not fully known.
- Further exotic feedback processes probably contribute, like neutron star mergers producing lots of the early r-process elements.
- Synthesising abundance data to compare the model to observations has several caveats:
  - The selection function of the stars needs to be reproduced.
  - Usually, stars are assumed to preserve the abundance of the ISM from which they were formed in their photospheres, but it can change, due to dredge-up events.
  - Stellar ages can only be roughly constrained from the commonly available data.

As can be seen from that list, chemical, as well as dynamical, processes need to be taken into account, in order to constrain the evolution of our Galaxy. The field is guided by high-redshift observations of MW-like spiral galaxies and also benefits from cosmological simulations, becoming able to reproduce observations. The interplay of all those fields, is constraining a consistent picture of the MW-evolution and is called Galactic archaeology. In this introduction recent advances in the field will be summarised.

1.5 STRUCTURE OF THE MILKY WAY

The MW disc sits in a CDM halo, which extends out to about 200 kpc and dominates the mass budget, with $\sim 10^{12}\,M_\odot$ [McMillan, 2011]. Satellite galaxies orbit through its gravitational potential, with the most prominent being the two Magellanic clouds, at a distance of 55 kpc, and the Sagittarius dwarf, 15 kpc away from the Galactic centre, which produces the prominent Sagittarius stream. Most of the baryonic mass is within 15 kpc radius, where the outer stellar halo is separated from the inner stellar halo. The inner structure, depicted in figure 1.4 and containing most of the MW's stars and cold gas, is composed of a disc and a central bulge with a bar.
This thesis will mainly focus on the disc, but here I will briefly discuss the other major components as well. The interested reader is referred to Sparke and Gallagher [2007] for an introduction to the MW and to Scheffler and Elsässer [1992] for a comprehensive overview on Galactic astronomy. Galactic dynamics are thoroughly covered in Binney and Tremaine [2008] and a further reference for chemical evolution is Pagel [2009].

1.5.1 HALO

The Galactic stellar halo envelopes the disc and the bulge and reaches out to 150 kpc, with a stellar mass content of about $4 \times 10^8\,M_\odot$ [Bell et al., 2008]. It is an important diagnostic for

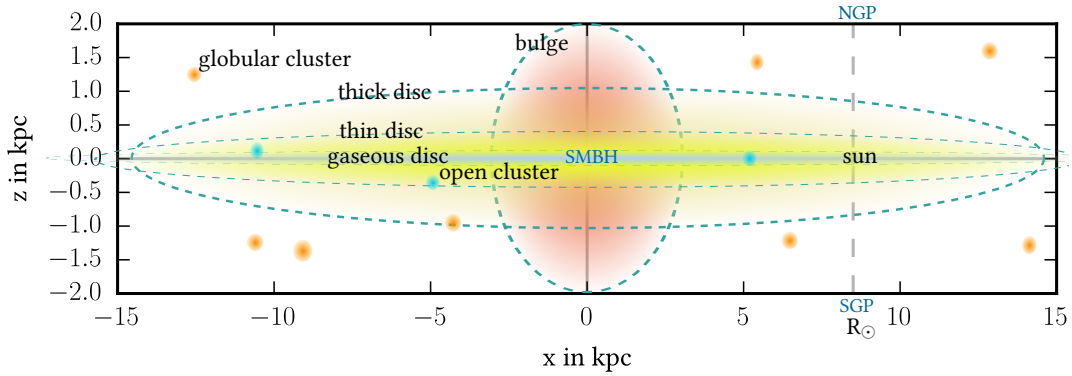

Figure 1.4: Schematic Milky Way

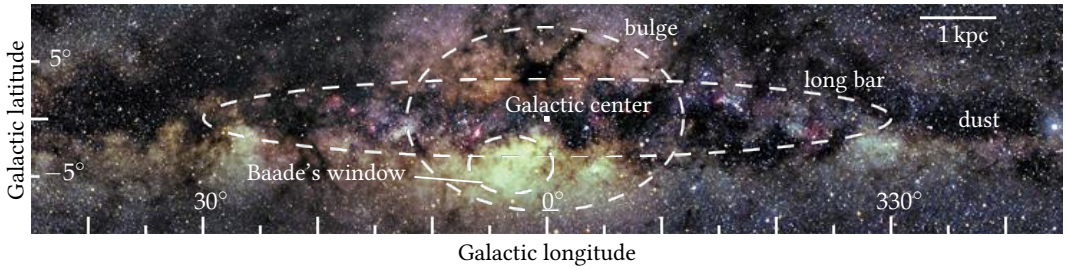

Figure 1.5: Milky Way centre in the optical with Galactic coordinates. Bulge. Credit: NASA / A. Mellinger

the MW evolution, with its old field star population and the globular clusters. It can roughly be dissected into an inner oblate spheroidal halo, comprising mainly in-situ formed stars and an outer spherical halo, where accreted stars, from satellite galaxy debris, are prevalent [Carollo et al., 2007]. The orbits around the Galactic centre are not ordered, with the outer halo showing a slight retrograde rotation, with respect to the disc rotation. Stars have a broad range of metallicities, with the bulk of stars being between $-3 < [\mathrm{Fe/H}] < -1$. The outer halo is more metal-poor and has a negative metallicity gradient with Galactocentric distance. There is no dust or ongoing star formation in the halo, though high velocity clouds are observed, which contribute to the gas infall of the disc [Putman et al., 2012].

1.5.2 BARRED BULGE

The bulge is the stellar nucleus of our Galaxy, with a boxy shape and a radius of about 3 kpc [Wegg et al., 2015]. It is hard to observe the inner part in the optical, because of heavy extinction by dust in the Galactic plane, which absorbs selectively, with shorter wavelengths being stronger absorbed [Trumpler, 1930]. This is clearly visible in the dark patches of figure 1.5, which is an optical image into the direction of the Galactic centre. The first to observe the bulge was Baade [1946], using a dust-free window, classifying the stars as population II stars. Subsequent observations, in the Near-InfraRed (NIR) and radio, revealed that the very centre of the bulge hosts an SMBH, named Sagittarius A*, with a mass of about $4 \times 10^6\,\mathrm{M}_\odot$ [Balick and Brown, 1974; Gillessen et al., 2009]. The overall stellar mass of the bulge region is approximately $10^{10}\,\mathrm{M}_\odot$ [Kafle et al., 2014]. It rotates ,but not

as ordered as the disc and with a high velocity dispersion. The metallicity distribution of surveyed stars peaks at the Solar value and they are usually α-enhanced, indicating a rapid chemical enrichment [Zoccali et al., 2007]. An elongated bar, made up of a variety of stable stellar orbits, has been detected [Blitz and Spergel, 1991] and is believed to rotate rigidly at a pattern speed of $\sim 50\,\mathrm{km\,s^{-1}\,kpc^{-1}}$, corresponding to a corotation radius of $\sim 4\,\mathrm{kpc}$ [Gerhard, 2011]. The bar induces orbital resonances in the disc and its outer Lindblad resonance, which is just inside the Solar Galactocentric radius, $R_\odot$, is believed to be responsible for several moving groups in the Solar Neighbourhood [Dehnen, 2000]. Together with the spiral arms, they induce radial migration of stars through the disc, facilitating mass inflow, chemical homogenisation and triggering star formation. Both structures seem to be dynamically decoupled, since the pattern speed of the spiral waves are much slower, with a corotation radius slightly outside of $R_\odot$ [Gerhard, 2011].
The bulge seems to be a pseudo-bulge, meaning that it mainly consists of an in-situ formed bar [Shen et al., 2010], contrary to a classical bulge, which would have build up from mergers. Hammersley et al. [2000] even detected a second thinner and longer bar structure, which is indicated in figure 1.6. The bar, together with the spiral density waves, probably have profound effects on the Galactic evolution and might also be responsible for the molecular ring, the biggest reservoir of molecular gas, which is necessary for star formation [Ragan et al., 2009], observed at 4 kpc from the Galactic centre.

1.5.3 DISC(S)

The disc is the main baryonic component of the MW, with a mass of around $10^{11}\,M_\odot$ [Kafle et al., 2014]. It is of almost circular shape, with a radius $\sim 15\,\mathrm{kpc}$ and the Sun sitting at $R_\odot \sim 8.5\,\mathrm{kpc}$ to the Galactic centre. That it is a system of its own and has an ordered rotation was discovered by Lindblad [1927]; Oort [1927, 1928]. It has a flat rotation curve, rotating clockwise when viewed from the North Galactic Pole (NGP), with a circular rotation speed of $v_c \sim 240\,\frac{\mathrm{km}}{\mathrm{s}}$ at the Solar radius [Reid et al., 2014], so that the Galactic year takes about 220 Myr. The orbits of the disc stars have only small deviations, with respect to the *local standard of rest*, with the Sun having an offset of about $U_\odot = 10\,\frac{\mathrm{km}}{\mathrm{s}}$, $V_\odot = 3\,\frac{\mathrm{km}}{\mathrm{s}}$ and $W_\odot = 7\,\frac{\mathrm{km}}{\mathrm{s}}$ [Aumer and Binney, 2009; Golubov et al., 2013].

a good approximation is $\frac{\mathrm{km}}{\mathrm{s}} \approx \frac{\mathrm{pc}}{\mathrm{Myr}}$, with a deviation $< 3\,\%$

New stars are formed from the inhomogeneous gas and dust layer, which is closely confined to the Galactic plane. Therefore groups of young stars, usually have a small velocity dispersion and they are called dynamically *cold*. Spiral arms are small overdensities in the form of transient waves, where star formation is preferentially taking place, which gives them their bluish glow (from massive and therefore hot, bright and short-lived stars), when seen in external face-on galaxies. In the outskirts of the disc a warp has been detected [May et al., 1993], bending the disc down from its plane at Galactic longitude $l = 0°$ and bending it up close to the anticentre. Another observed effect is called flaring [Momany et al., 2006], describing an increase in scale height with increasing Galactocentric distance.

When inspecting the density distribution of disc stars, Gilmore and Reid [1983] found that the disc can be decomposed into two components, with different scale heights. The thin disc with a scale height of about 300 pc and the thick disc with $\sim 1300\,\mathrm{pc}$. Already in his PhD thesis Oort [1926] saw kinematic traces of both discs, with the thick disc having a higher velocity dispersion, being dynamically hotter and therefore older than the

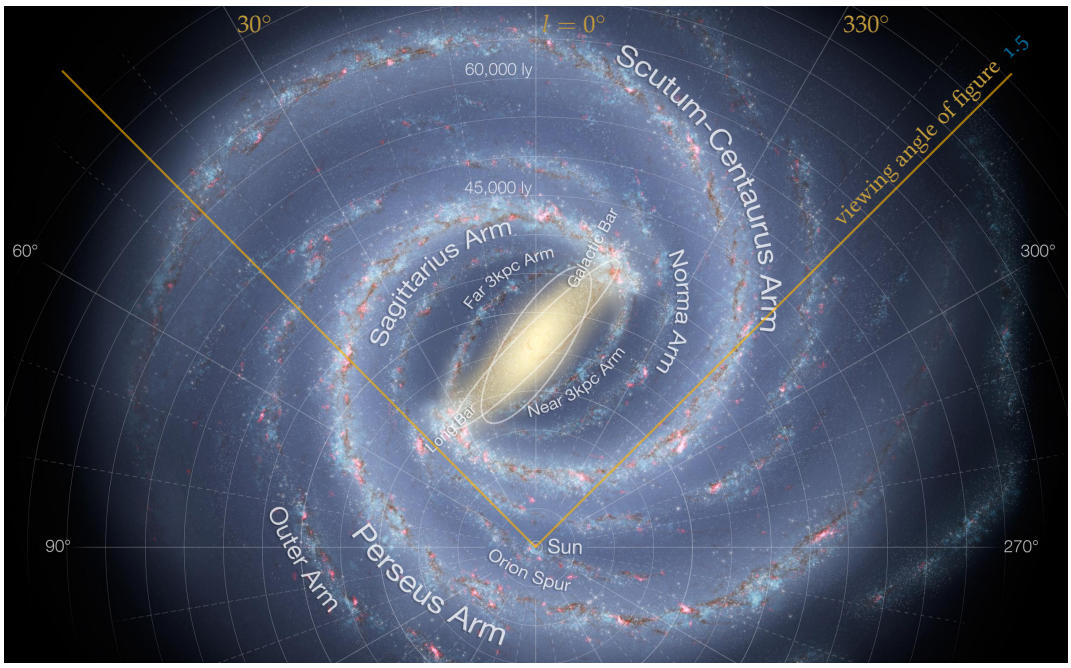

Figure 1.6: Milky Way face-on view from above the plane with Galactic latitude in degrees and distances in light years. The viewing angle from figure 1.5 is indicated in orange. Known spiral structure is annotated and was traced by H I, H II and CO surveys. The two bars have been constrained by infrared (IR) and microlensing surveys. References are given in Churchwell et al. [2009] from which the picture is taken. Credit: NASA/ JPL-Caltech/ ESO/ R. Hurt

thin disc stars. Similarly, in chemical abundance space the thick disc population shows a lower metallicity and higher α-enhancement compared to the thin disc [Gratton et al., 1996; Fuhrmann, 1998].

The stellar density of the discs drop exponentially vertically, as well as radially, with controversial results for the scale-length. Jurić et al. [2008] finds from Sloan Digital Sky Survey [York et al., 2000] (SDSS), using M-dwarfs that the thick disc has a larger scale-length than the thin disc, which is usually also observed in edge-on views of external spiral galaxies (see for example the MW analogue NGC 891 [Ibata et al., 2009]). When dissecting in abundance space, like Bensby et al. [2011], the thick disc scale-length seems to be shorter compared to the thin disc. Bovy et al. [2012] even finds that, using Sloan Extension for Galactic Understanding and Exploration [Yanny et al., 2009] (SEGUE) mono-abundance[11] populations, a smooth transition from old and spherical to young and elongated, takes place without the necessity of a distinct thick disc. The oldest population (with $[\mathrm{Fe/H}] = -1$ and $[\alpha/\mathrm{Fe}] = 0.5$), having a scale-length of 2 kpc and a scale height of 1 kpc and the youngest population (with about Solar abundances), having ≈ 4.5 kpc and ≈ 0.2 kpc respectively. Recent MW modelling approaches, combining chemistry and dynamics, are also able to produce an apparently bimodal distribution from a simple one-disc model by kinematic selection effects [Schönrich and Binney, 2009b; Minchev et al., 2013]. The question arising is how both discs formed and whether or not they share a common formation mechanism.

M-dwarfs are stars of spectral type M, the spectral type sequence being O, B, A, F, G, K, M, L, T from hot to cold, with the last two already being Brown Dwarfs

11 Stellar populations binned in [Fe/H] and [α/Fe].

1.5.4 FORMATION SCENARIOS

As already mentioned, traces of the formation history of the MW are imprinted in the chemical abundances and the kinematic information of its stars. When formed in the gaseous disc with low velocity dispersion, stars are believed to be randomly perturbed during their lifetime and to deviate increasingly from their initial nearly circular orbit. This makes their orbits more eccentric and also increases their deviations from the Galactic plane. The relation between the age of a stellar population and its kinematic state is called *Age Velocity-dispersion Relation (AVR)*. Because of the difficulty to determine stellar ages, it is observationally not clear if the velocity dispersion increases infinitely with time [Wielen, 1977] or already saturates after $\sim 5\,\mathrm{Gyr}$ of heating [Soubiran et al., 2008].
The seminal Eggen et al. [1962] proposed a monolithic and very short collapse of a protogalaxy as a formation scenario of the MW, which they derive from thorough analysis of stellar orbits and their correlations with infrared (IR)-excess (metal-abundance). Searle and Zinn [1978] investigated the globular cluster metal abundances in the outer halo and concluded that fragment accretion for a longer period is necessary to reproduce their distribution. Another paradigm, supported by the upcoming CDM cosmology, is hierarchical clustering, with mergers of smaller structures accumulating to larger systems [White and Rees, 1978].
The true evolution will most likely be a mixture of all those scenarios. But how important are those mechanisms and at which epochs do they dominate? How is the secular evolution of the individual parts of the MW and how do they interact with each other?

1.6 DECIPHERING THE MILKY WAY EVOLUTION

1.6.1 EXTRAGALACTIC OBSERVATIONS

Because of our perspective from the inside of our Galaxy and the fact that we can only observe its present-day state, galaxy surveys can help us to gain insight into the formation history of the MW. Not only that we can distinguish the different galaxy components easier from outside of a galaxy, but we can also look into the past of MW-like galaxies when targeting high-redshift progenitors. van Dokkum et al. [2013] found that 90% of the stellar mass of their MW-like galaxy sample is build up after redshift of 2.5 and that bulges and discs form in lockstep until redshift ≈ 1, when the bulge mass assembly ceases.

1.6.2 SIMULATIONS

The laboratory experiment in galaxy evolution can only be done via hydrodynamical N-body simulations. The *Millenium runs* [Springel et al., 2005; Boylan-Kolchin et al., 2009], which are purely gravitational cosmological simulations, were able to show the success of ΛCDM cosmology in reproducing the cosmic web, represented in the filamentary structure of galaxy distribution. Meanwhile, with development of codes, which allow for solving fluid dynamic equations, for the purpose of dealing with gas, and also significant improvements of our understanding about baryonic physics, the *Illustris* simulation [Vogelsberger et al.,

2014], was able to implement baryons and their feedback processes in their cosmological calculation. The obtained galaxy morphologies and their frequency distribution quite successfully reproduces the observed ones [Genel et al., 2014].
Specialised simulations that reproduce MW-like galaxies within realistic DM halos are also able to synthesise structural parameters of our Galaxy [Stinson et al., 2010; Guedes et al., 2011]. The bulge to disc ratio and the chemical evolution seem notoriously hard to reproduce. As these simulations are computationally demanding, they can not easily test a large parameter space.

1.6.3 ANALYTICAL MODELS

The exploration of a large parameter space can be better done with fast to compute (analytical) models that concentrate on a few major physical processes, which can be tested with discriminating observations, that are easy to synthesise. Usually these models are quite specialised, so that they only use chemical [Chiappini et al., 1997] or dynamical constraints [Just and Jahreiss, 2010] or target a specialised topic, as for example radial migration [Schönrich and Binney, 2009a]. Recently also a hybrid approach by Minchev et al. [2013], combining an N-body simulation [Martig et al., 2012] with a chemical evolution model, was very successful in reproducing multiple chemodynamical constraints.

1.6.4 MILKY WAY OBSERVATION

Future surveys are designed in order to pin down the assembly history of the MW and understanding the processes governing its evolution. In the following I will outline the major MW surveys, their specifications and prospective scientific yield from upcoming surveys.

1.6.4.1 ASTROMETRY

One major contribution will be from the astrometric satellite mission, Gaia [Lindegren et al., 2008] (Gaia). Gaia will deliver precise parallaxes, proper motions and photometry of all stars brighter than $G = 20$ mag. For a sub sample, of these 10^9 stars, it will also measure the radial velocity from low-resolution spectroscopy, mapping the complete phasespace distribution for an unprecedented number of stars, homogeneously. The precision will be about 15 μas for stars at 15 Apparent V magnitude (Vmag).
For comparison, the successful Hipparcos [Perryman et al., 1997] (Hipparcos) mission, which was magnitude limited at Vmag $\approx$ 7.5, yielded $\approx 10^6$ stars with a median precision of ~ 1 mas and had major impact on astronomy.

1.6.4.2 SPECTROSCOPY

Spectroscopic follow-up mission are under way with Gaia-ESO [Gilmore et al., 2012] (GES) and GALactic Archeology with HERMES [Anguiano et al., 2014] (GALAH). These will supplement the position and velocity data from Gaia with stellar parameters and chemical abundances from high-resolution spectroscopy for about $10^5 - 10^6$ stars. Significant statistical number of stellar spectra have been provided by the Geneva Copenhagen Survey [Nordström et al., 2004] (GCS), The Radial Velocity Experiment [Steinmetz et al., 2006] (RAVE), SEGUE and APO Galactic Evolution Experiment [Alam et al., 2015] (APOGEE). The RC sample

from the latter is very valuable when probing a large Galactic volume, because it provides almost $20,000$ stars with precise distances, stellar parameters, and abundances for up to 15 elements.

1.6.4.3 ASTEROSEISMOLOGY

In order to increase the accuracy of age determination asteroseismology can be facilitated, the major missions being Kepler [Borucki et al., 1997] (Kepler) and COnvection ROtation and planetary Transits [Baglin and COROT Team, 1998] (COROT). So far only $\sim 10^3$ stars with spectroscopic data benefit from added seismological data.

2

STATISTICAL INFERENCE WITH ASTRONOMICAL DATA

This chapter is about the interplay of models and data. In section 2.1 a Bayesian framework, to infer model parameters from observations, will be introduced and illustrated with the common problem of inferring distances from parallaxes. The second part will be on the construction of volume-complete stellar samples, in order to infer stellar number densities. It builds up on the results derived in the first section and discusses further complications, as the effect of interstellar extinction or binaries.

2.1 BAYESIAN INFERENCE

In this section the statistical framework will be introduced, which connects models with data in order to handle inference problems.
First, conditional probability will be illustrated with the Monty Hall problem. Then Bayes' theorem will be used for parameter inference and the involved steps will be elaborated. The section concludes with a short discussion of parameter space sampling and model comparison.

2.1.1 CONDITIONAL PROBABILITY

The concept of conditional probability, which will motivate Bayes' theorem, will be introduced by solving the famous *Monty Hall problem*:

> *Suppose you're on a game show, and you're given the choice of three doors: Behind one door is a car; behind the others, goats. You pick a door, say No. 1, and the host, who knows what's behind the doors, opens another door, say No. 3, behind which there is a goat. He then says to you, "Do you want to pick door No. 2?" Is it to your advantage to switch?*

this question to the "Ask Marilyn" column of Parade magazine in 1990 was seeking advice for the common situation a candidate would find him or herself in the show "Let's make a deal", hosted by Monty Hall

The questioner is looking for the conditional probability of the car being behind a door, given the host has opened another door with a goat, after the initial choice of the candidate. Before the host opens a door, the probability of the events (C_i) of the car being behind door $i \in 1, 2, 3$, are equally likely and sum up to unity,

$$P(C_1 \cup C_2 \cup C_3) = P(C_1) + P(C_2) + P(C_3) = 1. \tag{6}$$

Without loss of generality we follow the path of the question and want to know the probability of winning the car when switching from the chosen door one to door number two, in the event (H_3) that the host opens door three with a goat behind it. This is referred to as the conditional probability,

$$P(C_2|H_3) = \frac{P(C_2 \cap H_3)}{P(H_3)}, \tag{7}$$

which is defined as the *intersection* of both events normed by the probability of H_3, illustrated as the red rectangle in figure 2.1. Because these two events are not statistically independent, as the host would not open door three when the car is behind it, the conditional probability does not commute.

$$P(C_2|H_3) \neq P(H_3|C_2) = \frac{P(H_3 \cap C_2)}{P(C_2)}. \tag{8}$$

They can however be related to each other, when replacing the intersection from equation 7 with the conditional probability from equation 8.

$$P(C_2|H_3) = \frac{P(H_3|C_2)P(C_2)}{P(H_3)} \tag{9}$$

This is a simple form of Bayes' theorem. The probability of the host opening door three, $P(H_3)$ can be partitioned with help of the events C_i (because they are mutually exclusive and span the whole probability space)

$$P(H_3) = P(H_3 \cap C_1) + P(H_3 \cap C_2) + P(H_3 \cap C_3), \tag{10}$$

which can be transformed, using conditional probability (equation 7),

$$P(H_3) = P(H_3|C_1)P(C_1) + P(H_3|C_2)P(C_2) + P(H_3|C_3)P(C_3). \tag{11}$$

Plugging this into equation 9 leads to:

$$P(C_2|H_3) = \frac{P(H_3|C_2)P(C_2)}{P(H_3|C_1)P(C_1) + P(H_3|C_2)P(C_2) + P(H_3|C_3)P(C_3)}. \tag{12}$$

For the right hand side all probabilities can be deduced from the game rules. In the event of C_1 the host has free choice, whether to open door two or door three (equation 13a), if C_2, he has to chose door three (equation 13b), and if C_3 he can not open door three (equation 13c).

$$P(H_3|C_1) = \tfrac{1}{2} \tag{13a}$$
$$P(H_3|C_2) = 1 \tag{13b}$$
$$P(H_3|C_3) = 0 \tag{13c}$$

Therefore $P(C_2|H_3) = \frac{2}{3}$ and $P(C_1|H_3) = \frac{1}{3}$, as indicated in the green rectangles of figure 2.1, which doubles the chances to win the car for the changing candidate.

2.1.2 PARAMETER ESTIMATION USING BAYES' THEOREM

Bayes' theorem states in its general form:

> Fix a probability space and an event A. If the set $B_1, \ldots B_k$ are a partition, i.e. mutually exclusive events, spanning the whole probability space, then

$$P(B_i|A) = \frac{P(A|B_i)P(B_i)}{\sum_{j=1}^{k} P(A|B_j)P(B_j)} = \frac{P(A|B_i)P(B_i)}{P(A)}. \tag{14}$$

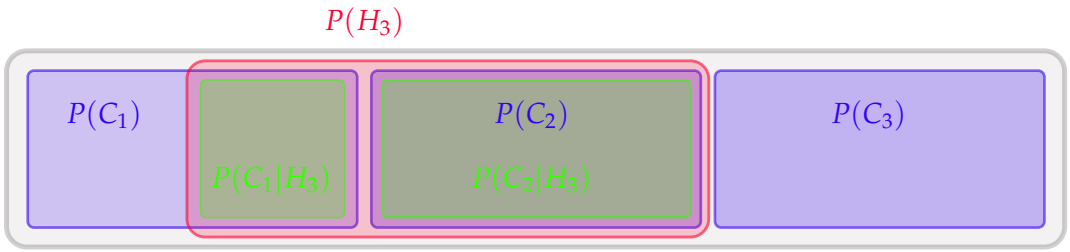

Figure 2.1: The conditional probability of the host opening door three when the candidate picked door one. It can be seen how the occurrence of event H_3 changes the probability space.

It can be facilitated to determine the best parameters (θ_i) for specific models (M_i) given some data (D),

$$P(\theta_i|D, M_i) = \frac{P(D|\theta_i, M_i)P(\theta_i|M_i)}{P(D|M_i)}. \tag{15}$$

The left-hand side is called *posterior* giving the probability distribution over the parameter space for the data assuming the given model M_i. Bayes' theorem is used to express the posterior as a product of *prior* and *likelihood*, divided by (what can be seen to be) a normalisation constant. The *prior*, $P(\theta_i|M_i)$, incorporates the a priori knowledge of the possible model parameter values, independent of the data. The *likelihood*, $P(D|\theta_i, M_i)$, representing the probability of the data given the model parameters, can also be referred to as *measurement model*. The denominator, $P(D|M_i)$, is called the *evidence* and gives the probability of observing the data assuming the model to be true. It is given by marginalizing (integrating) the nominator over the parameter space

$$P(D|M_i) = \int_{\theta_i} P(D|\theta_i, M_i)P(\theta_i|M_i)d\theta_i. \tag{16}$$

Generally, D and θ_i are vectors. Since the evidence is not depending on the parameter it can be seen as a normalization constant, Z, which is only a scaling factor that does not change the shape of the posterior but will get important when comparing different models in section 2.1.5.

2.1.3 AN EXAMPLE – INFERRING DISTANCES FROM PARALLAXES

On the following pages, the properties of the different terms in Bayes' theorem are illustrated using a common astrophysical inference problem presented in Bailer-Jones [2015]. The paper is on estimating the true distance, d in pc, from a measured parallax, ϖ in arcsec, and its associated error, σ_ϖ, for a single star, using a measurement model (likelihood) and prior information about distances.

$$P(d|\varpi, \sigma_\varpi, M_\varpi) = \frac{1}{Z}P(\varpi|d, \sigma_\varpi, M_\varpi)P(d|M_\varpi) \tag{17}$$

with Z being the evidence for our model

$$Z = P(\varpi|\sigma_\varpi, M_\varpi) = \int_{d=0}^{d=\infty} P(\varpi|d, \sigma_\varpi, M_\varpi)P(d|M_\varpi)\mathrm{d}d. \tag{18}$$

Since the physical model, M_ϖ, of the parallax is well understood and we are only interested in the distribution of the true distance, d, we will drop M_ϖ in the notation. The σ_ϖ is treated as independent data, which is always *given*, be it in the posterior, or in the likelihood, or in the evidence. This is possible because the parallax is independent of its error measurement and the variance of the error is negligible, compared to the parallax error.
Here the focus will be on the distance estimation for a *single* star. In section 2.2 the inference of distances for a sample of stars will be discussed. The following paragraphs until subsection 2.1.3.6 are using and summarising content from Bailer-Jones [2015].

2.1.3.1 DATA

Data are fundamentally some empirical evidence. In astronomy those are usually observations. It can be used to test or deduce hypotheses.
The observation (D), used to infer distances from, are parallaxes (ϖ), which are angle measurements that will ultimately be acquired from an interplay of optics and photodetectors. In automated surveys like Hipparcos [Perryman et al., 1997] (Hipparcos) and Gaia [Lindegren et al., 2008] (Gaia) a model of the optics and electrical signals will interpret the detections and yield two measurements, the parallax, ϖ, and the parallax error, σ_ϖ. These are independent as the error primarily depends on the number of photons arriving at the detector, which in turn depends on the star's apparent magnitude and on the position in the sky through the satellite's scanning law [de Bruijne, 2012; Arenou et al., 1995]. For an ensemble of stars the parallax and its associated error might be correlated since the more distant stars are also more likely to be fainter [Luri et al., 2014, fig. 9].
Because of the noise, σ_ϖ, in the parallax measurement, ϖ, we can never measure the exact distance of a star but can only derive a posterior Probability Density Function (PDF), $P(d|\varpi, \sigma_\varpi)$, on the possible distances, d, given a specific measured parallax and its associated error.
Since the error is Gaussian, negative parallaxes occur naturally [Lee, 1943] and with the inference model it will be possible to deduce valuable information from them (see figure 2.7 for an illustration).

2.1.3.2 MODEL

The physical model, M_ϖ, that we have in mind when deriving true distances, d, from measured parallaxes, ϖ, is simple geometry and based on the knowledge of Solar system mechanics.
A star which is observed will change its position on the sky with respect to a fixed background (e.g. quasars) with Earth's motion around the Sun as indicated in figure 2.2. The tangent of this parallax, $\tan(\varpi)$, equals the distance from the Earth to the Sun, $1AU$, divided by the distance from the Sun to the distant star, d. Because of the huge distances between stars in the Galaxy the small angle approximation applies and we can write

$$d^{-1} = \tan(\varpi) \approxeq \varpi \tag{19}$$

In reality there are possible complications, for example binaries, but to first-order it is sufficient to account for the star's proper motion and the parallax to incorporate its movement with respect to the background.

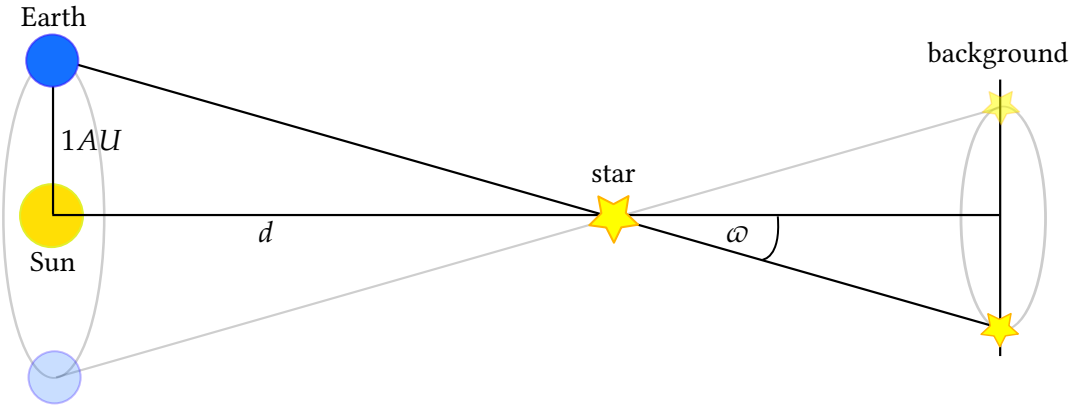

Figure 2.2: Geometry of parallax measurement. For $\varpi = 1\text{arcsec} \rightarrow d = 1\text{pc} \approxeq 2 \times 10^6 AU$. In the course of 6 month the baseline is 2 AU with the maximum angular shift being two times the parallax, ϖ.

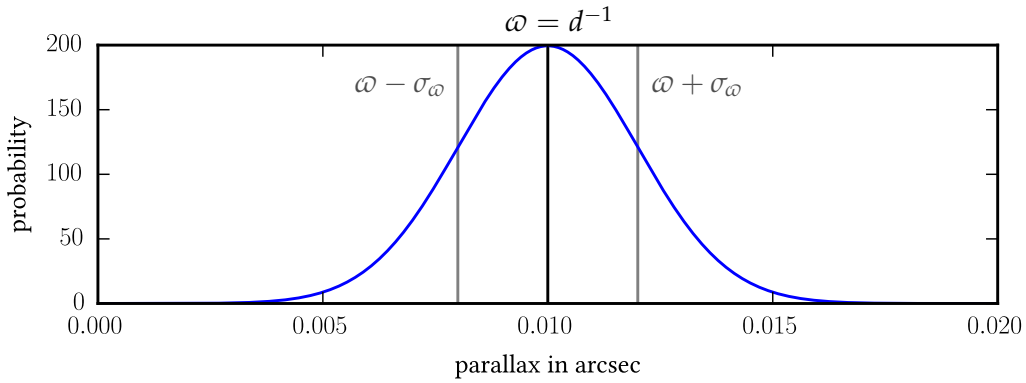

Figure 2.3: Probability distribution for true distance of 100 pc (equivalently a true parallax of 0.01 arcsec) and a relative error, $\frac{\sigma_\varpi}{\varpi}$, of 0.2

2.1.3.3 LIKELIHOOD

Because of the data acquired and the physics involved, a measurement distribution can be deduced for a specific true distance, d. The unknown true parallax would be $\frac{1}{d}$ and we assume the measurement of ϖ to be normally distributed according to the known positive parallax error[1], $\sigma_\varpi \geq 0$, around the true parallax, $\frac{1}{d}$,

$$P(\varpi|d,\sigma_\varpi) = \frac{1}{\sqrt{2\pi\sigma_\varpi^2}} \exp\left(-\frac{\left(\varpi - \frac{1}{d}\right)^2}{2\sigma_\varpi^2}\right). \tag{20}$$

This is the probability of observing a parallax for a specific true distance with our measurement model. With coordinate transformation we can transform the PDF per unit parallax, into a PDF per unit distance. Because of the inverse relation, $\varpi = \frac{1}{d}$, and the Jacobian, $\frac{1}{d^2}$, the resulting probability will no longer be normal but skewed as shown in figure 2.4. This probability function in units of distance, $f(d|\varpi,\sigma_\varpi)$, has the median in the same position as in equation 20 because the probability transforms monotonically but the mode (peak)

1 The error of the noise measurement is neglected (error in apparent magnitude), since its impact on the posterior is small compared to the parallax error.

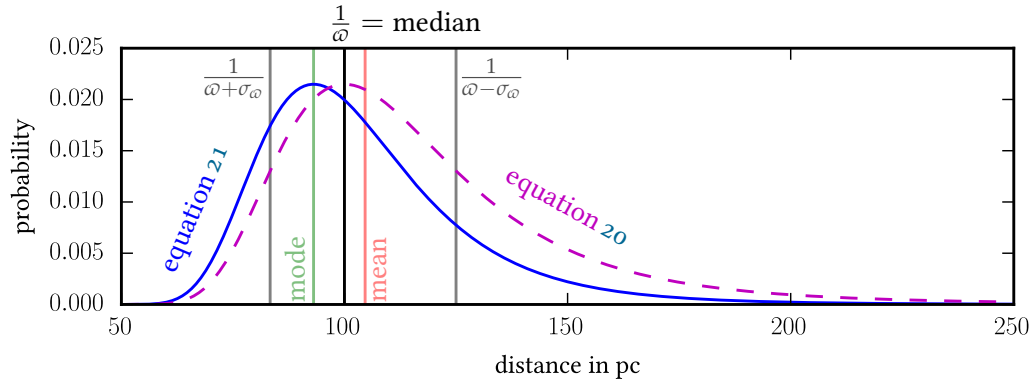

Figure 2.4: Likelihood (equation 20) in dashed magenta as a function of distance for a measured parallax $\varpi = 0.01$ and a parallax error $\sigma_\varpi = 0.002$. Since the likelihood as a function of distance is no longer a probability measure its mode is arbitrarily normalised to the mode of the transformed likelihood PDF (equation 21). For the transformed PDF the mode and the mean are given, with both no longer coinciding with the median as in figure 2.3. The inverted 1σ error intervals from figure 2.3 are also indicated to illustrate the loss of a symmetric error distribution when transforming the likelihood PDF from parallax to distance.

and the mean (expected value) are shifted. It can also be seen that the symmetric error in parallax transforms into an asymmetric error in distance

$$f(d|\varpi,\sigma_\varpi) = \frac{1}{d^2\sqrt{2\pi\sigma_\varpi^2}} \exp\left(-\frac{\left(\frac{1}{d}-\varpi\right)^2}{2\sigma_\varpi^2}\right). \tag{21}$$

However, this probability function of the distance, $f(d|\varpi,\sigma_\varpi)$, is not helpful in determining the posterior, because it is just the PDF of ϖ^{-1}.

It might be insightful to mention that Francis [2013, sec.2.3] is drawing samples from $f(d|\varpi,\sigma_\varpi)$ in order to correct for a bias referred to as *parallax bias*, which is attributed to the skewed probability distribution of equation 21 (see figure 2.4). A true parallax $\varpi_{\text{true}} = 0.01$ together with a fractional error are assumed. Since the resulting mean is higher than $\varpi_{\text{true}}^{-1}$ Francis [2013, eq.2.11] deduces that the distance $d = \varpi^{-1}$ needs to be decreased in order to have a better approximation of the true distance. Beside $\varpi_{\text{true}} \neq \varpi$, I would argue that starting from a measured parallax $\varpi = 0.01$, the inverted distance $d = \varpi^{-1}$ should be increased, since the mean of the PDF (over units of distance) is larger than 100 pc, as depicted in figure 2.4.
Probably this is more of a philosophical question, but definitely an interesting one, as the corrections are of opposite sign and it also illustrates the different approaches of Bayesian and frequentist statistics. In Bayesian statistics such a bias correction would not be applied, because it is considered in the prior. The prior contains all the information about the scale of d, for the purpose of integration, and translates the likelihood into the posterior, which is (after normalisation) a PDF over d.

2.1.3.4 PRIOR

The prior, $P(d)$, or $P(\theta_i, M_i)$, incorporates the assumption about the distribution of true distances, before a measurement is obtained (and it can also be updated with new measure-

ments or independent observations). All distances are positive, by definition. In order to normalise the prior we need to use a limiting distance, d_{lim} which could be the maximum distance for which we expect to observe a star,

$$P_1(d) = \begin{cases} \frac{1}{d_{\mathrm{lim}}} & \text{if} \quad 0 < d < d_{\mathrm{lim}} \\ 0 & \quad\quad d \leq 0 \vee d \geq d_{\mathrm{lim}}. \end{cases} \tag{22}$$

This flat prior incorporates implicitly the assumption that stellar density varies as d^{-2} because short distances have the same probability as large distances though more stars are expected at larger distances. An improvement is the constant volume density prior,

$$P_{\mathrm{d}^2}(d) = \begin{cases} \frac{3}{d_{\mathrm{lim}}^3} d^2 & \text{if} \quad 0 < d < d_{\mathrm{lim}} \\ 0 & \quad\quad d \leq 0 \vee d \geq d_{\mathrm{lim}}. \end{cases} \tag{23}$$

This has the highest expectation at d_{lim} with no probability of stars at larger distances, which is a discontinuity that results in a bias for measurements with large errors. An improved prior allows for arbitrarily large distances, has no (unphysical) sharp cut-off at d_{lim} and should still be normalisable.
An easy way to implement that mathematically is an exponentially decreasing volume density prior, which is also physically motivated (our instrument not being able to see faint/distant stars and the components of the Galaxy having exponentially decreasing stellar densities[2]),

$$P_{\mathrm{d}^2\mathrm{e}^{-d}}(d) = \begin{cases} \frac{1}{2L^3} d^2 e^{-\frac{d}{L}} & \text{if} \quad d > 0 \\ 0 & \quad\quad d \leq 0. \end{cases} \tag{24}$$

with $L > 0$ being a length scale though the mode of the prior PDF occurs at somewhat larger true distance values, as can be seen in figure 2.5 where all priors are depicted. This is just a short summary of possible priors for this inference problem, which is elaborated in greater detail in Bailer-Jones [2015].

The exponentially decreasing volume density prior, $P_{\mathrm{d}^2\mathrm{e}^{-d}}$, has the favourable properties of being simple, physically motivated, continuous and normalisable. This does not mean that it is necessarily the best prior, but without better knowledge about the distribution of stars or the survey selection function, it will yield robust estimates for the distance of a star, even when its associated parallax error is large.

2.1.3.5 EVIDENCE

In the distance inference problem the evidence, $P(\varpi|\sigma_\varpi)$, is hidden as the normalisation constant, Z, because a preferred model, M_ϖ, already exists and the unnormalised posterior already yields the probability distribution of the true distance. But when interested in calculating the evidence for model comparison, the likelihood and the prior would have to be marginalised over all possible distances (equation 18) and compared to the evidence of other models.

2 in principle the prior could also be dependent on Galactic latitude and Galactic longitude with a more sophisticated Galaxy model using independent data in the background

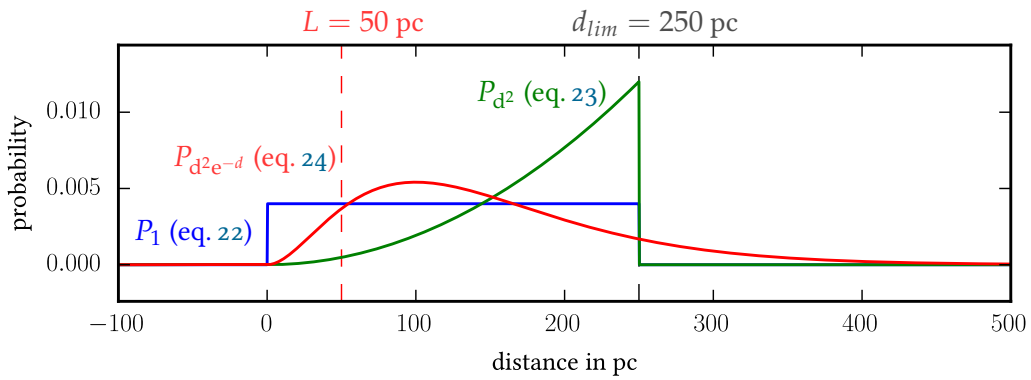

Figure 2.5: Normed distance priors

2.1.3.6 POSTERIOR

After obtaining the likelihood, $P(\varpi|d,\sigma_\varpi)$, and choosing a prior, $P_{d^2e^{-d}}(d)$, the posterior, $P(d|\varpi,\sigma_\varpi)$, can be calculated. By multiplying the likelihood, which is a probability measure of ϖ, with the prior, which contains all the a priori information about the scale of d, the posterior is yielded, which is an unnormalised PDF over distance. After normalisation with the evidence (which is not necessary, if only interested in the relative probability distribution of the true distance) the posterior is the (relative) probability of different true distances given a specific parallax measurement and its associated error.
In figure 2.6, the posterior is depicted for a parallax measurement $\varpi = 0.01$, associated error $\sigma_\varpi = 0.002$, and a length scale $L = 100\,\text{pc}$ for the prior $P_{d^2e^{-d}}(d)$. Beware that naively inverting the parallax would yield 100 pc. Compared to the median of the posterior $d \approx 115\,\text{pc}$, this is significantly less, which is mainly due to the error distribution not being taken into account.
As a summary of the posterior PDF, the mode or the median can be reported together with associated errors. Because in our case the posterior is asymmetric, it is preferable to give confidence intervals (as shown in figure 2.6) instead of a standard deviation.
In figure 2.7 the likelihood and the posterior are displayed for a negative parallax of $\varpi = -0.01$ and two different relative parallax errors of $\frac{\sigma_\varpi}{\varpi} = 0.1$ and 0.4. First, it should be noticed that, as a function of distance, the likelihood is no longer a probability measure. However, even though it is increasing steadily towards infinity (for negative parallaxes), the product with the prior yields a reasonable posterior distance distribution. Secondly, for larger parallax errors the likelihood in solid blue is broader and its corresponding posterior resembles more the prior, which makes sense as the measurement is less definite, so the prior knowledge is weighted stronger in the posterior PDF. And lastly, for increasing precision the negative parallax measurement indicates increasingly low true parallaxes, which shifts the posterior, in dashed red, to much higher distance values in figure 2.7.

2.1.4 SAMPLING THE PARAMETER SPACE

For models involving many parameters the evaluation of the posterior over the whole parameter space will become computationally expensive. In order to sample the posterior distribution efficiently Markov Chain Monte Carlo (MCMC) algorithms can be facilitated.

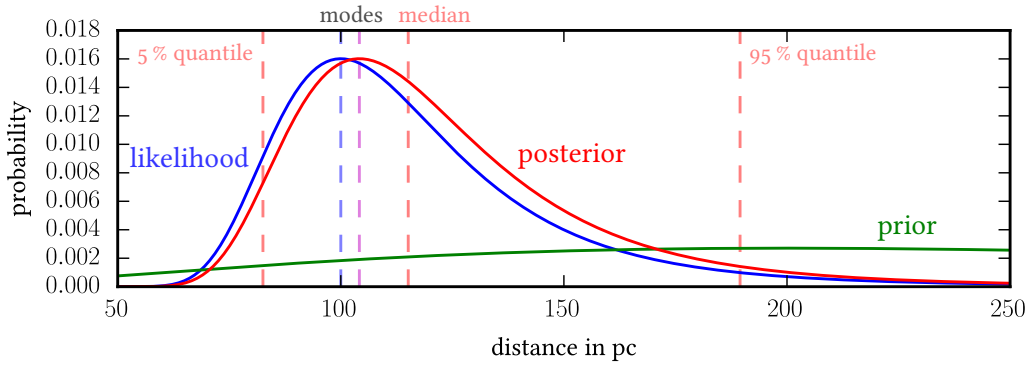

Figure 2.6: The prior, in green (with a length scale of $L = 100\,\mathrm{pc}$), multiplied by the likelihood, in blue, yields the unnormalised posterior over the distances, in red, for $\varpi = 0.01$ and $\sigma_\varpi = 0.002$. For the posterior the median and 90 % confidence intervals are indicated with red dashed lines. Only the posterior and the prior are probability measures and integrate to unity contrary to the likelihood over distance. Therefore the mode of the likelihood, marked by the dashed blue line, is normalised to the mode of the posterior, indicated in dashed magenta.

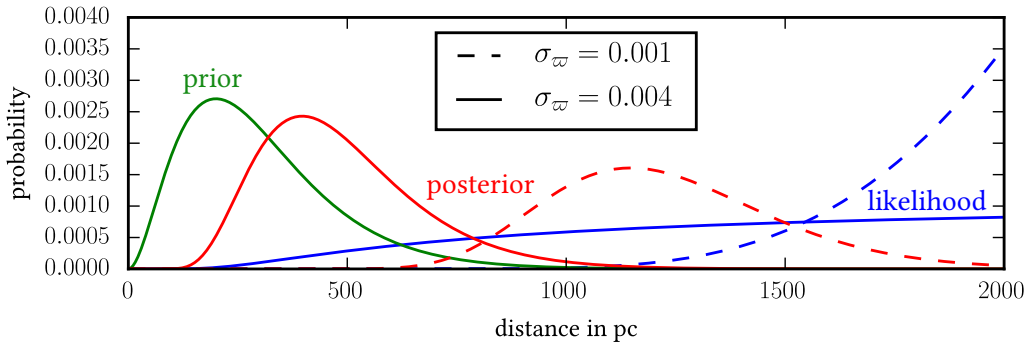

Figure 2.7: Likelihood in blue and posterior in red for negative parallax, $\varpi = -0.01$, and different relative parallax errors, $\frac{\sigma_\varpi}{\varpi} = 10\,\%$ in dashed lines and 40 % in solid lines. The prior in green stays unaffected. What is visible of the likelihoods as functions of distance is arbitrarily normalised to unity.

For an increasing number of steps, their sample density will converge towards the posterior probability density. The commonly used Metropolis-Hastings algorithm achieves this by doing a probability-guided random walk on the parameter space. It rejects proposed steps with a certain probability when the outcome is lower compared to the previous step, and accepts those steps that increase the outcome. Depending on the initial position in the parameter space, it can take a while until the algorithm finds the volume of highest density. This phase is referred to as burn-in and steps during that process should be thrown away, in order not to bias the inferred PDF. Once it has reached the volume of highest density, it will sample this space and the sampling density will converge towards the PDF. In order to test if this is the global maximum and not only a local maximum, the starting points should be varied and it should be checked whether each such Markov chain is equilibrating in the same volume of highest density.
With multiple chains exchanging step information the convergence towards the PDF can be accelerated and the probability evaluation of single steps can be distributed on different processors for each chain, which makes the calculation much faster on multi-core systems, especially when single probability evaluations take a lot of time. We will use an efficient algorithm with Python implementation in chapter 3.

Sometimes the likelihood is impossible to construct or computationally not feasible to evaluate. Still in astrophysics it is usually possible to simulate mock data sets through forward modelling. In that case an Approximate Bayesian Computation (ABC) MCMC method can be used, in order to approximate the posterior distribution. This is achieved by quantifying the differences of an observed data set, to simulated ones via distance metrics, which are usually applied on summary statistics of the data sets (see Robin et al. [2014] for an example). Summary statistics can be bins or quantiles of a distribution, which then can be measured using Euclidean distance or more sophisticated metrics. To compare one-dimensional cumulative distributions the Anderson-Darling test [Anderson and Darling, 1952] can also be used as a minimum-distance-estimate between two data sets, and should be preferred to the (less discriminative but more often used) Kolmogorov–Smirnov test.

2.1.5 MODEL COMPARISON

When interested in the probability of a specific model given the data, $P(M_i|D)$, the evidence ($P(D|M_i)$) from equation 15 needs to be evaluated. With Bayes' theorem it follows that

$$P(M_i|D) = \frac{P(D|M_i)P(M_i)}{P(D)}. \tag{25}$$

Using exhaustive and mutually exclusive models, $M_j, j \in 1...k$, the evidence for the data can be rewritten as

$$P(D) = \sum_{j=1}^{k} P(D|M_j)P(M_j). \tag{26}$$

Unlike in the simple Monty Hall problem, see equation 12, it usually is unfeasible to find an appropriate set of models covering all possibilities. Since $P(D)$ is a model-independent value (i.e. the same for all models) two models, M_1, M_2, can be compared to each other, by

the ratio of their probability given the data, $P(M_i, D)$ (equation 25). Under the assumption that no model is a priori preferred, $P(M_1) = P(M_2)$ (i.e. they cancel out in equation 27) this ratio is called *Bayes factor*, R, and involves the integration of the unnormalised posterior (i.e. likelihood, $P(D|\theta_i, M_i)$, times the prior, $P(\theta_i|M_i)$,) over the whole parameter space, θ_i

$$R = \frac{P(M_1|D)}{P(M_2|D)} = \frac{P(D|M_1)\cancel{P(M_1)}}{P(D|M_2)\cancel{P(M_2)}} = \frac{\int_{\theta_1} P(D|\theta_1, M_1)P(\theta_1|M_1)d\theta_1}{\int_{\theta_2} P(D|\theta_2, M_2)P(\theta_2|M_2)d\theta_2}. \tag{27}$$

As can be seen, the Bayes factor is comparing the ability of different models to explain a common dataset. Because it involves marginalising over the whole parameter space it inherently punishes complex models with many parameters, which will not be favoured for having a high maximum likelihood at a specific set of parameters (very small volume of the parameter space) but for their ability to explain the data over the whole parameter space[3]. Since the priors for the parameters, $P(\theta_i|M_i)$, are involved in the calculation of the evidence, $P(D|M_i)$, the sensitivity of the Bayes factor to different priors should be tested. Due to this and also the assumption of equal model priors, the preference of one model over the other should only be stated for sufficiently[4] large R. Given a large Bayes factor it can be concluded that one model is better than the other, but in order to state that *the* best model is found, the evidence has to be calculated for all possible models, or at least all plausible models.

2.2 STELLAR NUMBER DENSITIES FROM STAR COUNTS

In Galaxy modelling, an important parameter is the stellar mass density. To derive this quantity, a complete census of stars in a given volume is needed. In order to attribute stars to a specific volume accurate distances are required. As was argued in the previous section, parallaxes are well suited to infer distances from. Parallax measurements are most reliable for close-by stars. The best set of parallaxes to date was measured during the Hipparcos survey. Keep in mind that the methods described in section 2.1 do not allow the derivation of exact distances, but only a posterior probability distribution, whose width scales with the parallax errors. Another complication arises because stars of the same Absolute V magnitude (VMag) appear fainter the further they are away. At a certain distance they are no longer visible to the detectors depending on the apparent magnitude limit of the survey. In figure 2.8 this situation is depicted for the Hipparcos survey, which is only complete for stars brighter than $\text{Vmag}_{\text{lim}} = 7\text{mag}$[5]. This implies that a Sun-like star with VMag$= 4.83$ mag will be seen to a distance modulus, μ, of

$$\mu \equiv Vmag - VMag = 7 - 4.83 = 2.17, \tag{28}$$

where μ is a way of expressing distances in magnitudes. Equation 28 can be translated to a distance,

$$d = 10^{1+\frac{\mu}{5}} \approx 27pc, \tag{29}$$

3 More complex models should be motivated by more complex data.

4 What *sufficient* means is subjective and different authors state different values, $R > 10$ is an indication for the preference of one model over the other.

5 Though Hipparcos has no sharp cut-off, but rather a slow decline in completeness.

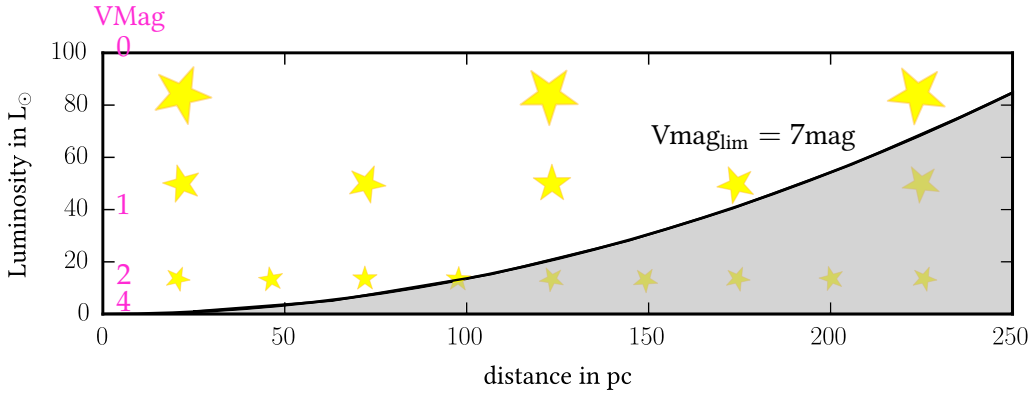

Figure 2.8: The Vmag limit is plotted in the luminosity distance plane for the Hipparcos 100 % completeness limit of 7 Vmag. The distance is given in pc and the luminosity in Solar luminosity, $L_{\odot}$. The relation to absolute V magnitude, VMag, is indicated on the left in magenta. It should be noted that the stellar density indicated in the figure represents a line of sight view for a homogeneous stellar distribution. If considering the whole volume, within a specific distance, the number of stars should increase with the distance squared.

corresponding to a limiting distance until which the Sun would be visible for a survey with a magnitude limit of $Vmag = 7$. Brighter stars, e.g. Vega with $VMag = 0$, will be visible up to a distance of approximately 250 pc. This means that for stars with different intrinsic brightnesses the limiting distances, up to which they will be observable, are also different, as shown by the inverse square law (black curve) in figure 2.8. Because of this the inferred mean luminosity of the visible stars in figure 2.8 will be overestimated, which is referred to as Malmquist bias.

In the following sections it is explained how to obtain volume-complete samples of stars, beginning with the approach used in Just and Jahreiss [2010] (paper I). The methods in sections 2.2.2 and 2.2.3 have been implemented by the author. The sections following thereafter can be seen as ideas or advises that could further increase the accuracy of stellar number density determinations. This is why the last sections are less elaborate and of a more conceptual nature.

2.2.1 MAGNITUDE AND DISTANCE CUTS

The method of distance and absolute magnitude cuts was applied in paper I. They used the vertical velocity distributions of volume-complete Main Sequence (MS) star samples, as observational constraint for their dynamical model. The local mass density, however, was taken from [Jahreiss and Wielen, 1997].
In their approach distances are derived directly from inverted parallaxes, $d = \frac{1}{\varpi}$, and stars with relative parallax error larger than 15 % are excluded, $\frac{\sigma_{\varpi}}{\varpi} > 0.15$, because their distance error becomes too large to assign them reliably to a volume[6]. In a next step Absolute

6 The number of stars, that do not fulfil these quality cuts, is usually below 2 % for stars brighter than the limiting Apparent V magnitude for completeness in the Hipparcos catalogue. Beware that stars with higher relative parallax errors are more likely to have faint apparent magnitudes and large distances. So a bias is introduced when throwing out these stars.

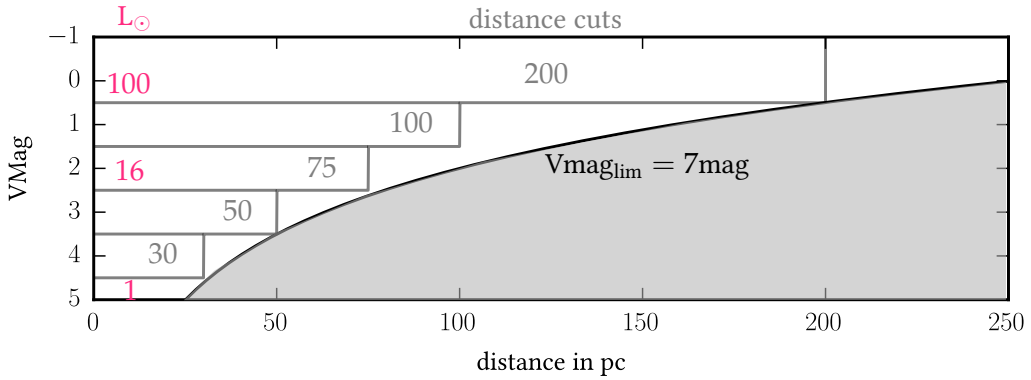

Figure 2.9: Same as figure 2.8 but now the Apparent V magnitude limit is plotted in the Absolute V magnitude over distance plane. 7 Vmag is the 100 % completeness limit of the Hipparcos catalogue. The distance cuts for the different absolute magnitude bins are indicated as boxes, it can be seen that the first magnitude bin has an relatively conservative distance cut. For reference the luminosity scale is given in magenta on the left.

V magnitudes are calculated from the measured distances and apparent magnitudes. Stars are binned in VMag and each bin has a specific distance cut, such that Vmag of the stars never fall below the Vmag-limit for which the Hipparcos survey is complete, Vmag= 7mag, as illustrated in figure 2.9.

2.2.2 BINARY SPLITTING AND ANALYTIC EXTINCTION CORRECTION

In Rybizki and Just [2015] we used volume-complete samples as observational constraint to infer Initial Mass Function (IMF) parameters from the MW disc model [Just and Jahreiss, 2010] (JJ-model). The method is basically the same as in the previous subsection but with the additional correction for binary systems and extinction.

The known binary systems, which have a magnitude difference entry in the Hipparcos input catalogue, were split up so that the formerly unresolved stellar systems changed their magnitudes. This can be seen in figure 2.10 where it is illustrated for an equal mass binary system with a VMag ≈ 0.15 at about 55 pc. When splitting the system we now have two stars each being half as bright as the combined binary system with approximately VMag ≈ 0.75 larger magnitude. As a consequence the unresolved binary system is lost from the 200 pc volume and two stars are added to the 100 pc volume. This is because the binary system in the depicted example of figure 2.10 is shown for a distance smaller than 100 pc. It should be mentioned that if the binary distance was between 100 and 200 pc then it would be lost from the 200 and the 100 pc volume. This happens more often than the case of figure 2.10, because the volume between 0 to 100 pc distance is seven times smaller than the volume between 100 and 200 pc distance.
The changes in star counts for each magnitude bin after correcting for binaries are on the two percent level (see table 3). This does not reflect the true magnitude of the effect, because binaries with a massive primary are hard to resolve, due to blurred lines from fast rotation, and are most likely not listed in the Hipparcos input catalogue and hence excluded from our

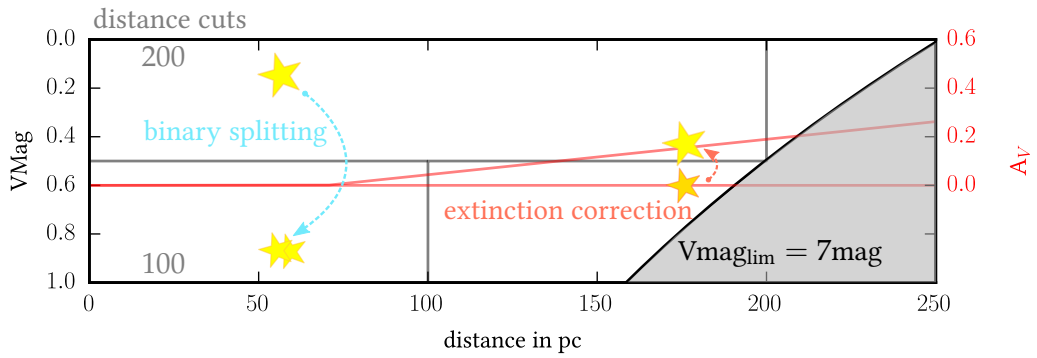

Figure 2.10: A zoom-in of figure 2.9 is shown. The stars' Absolute V magnitude is shown on the left y-axis and the extinction in V-Band on the right which is referring to the red curves illustrating our adopted extinction model. The upper red curve is the extinction for stars in the Galactic plane and the lower red curve has no extinction referring to stars with Galactic latitude larger 52°. The extinction correction is illustrated for a star in the Galactic plane with a distance of approximately 175 pc. On the left hand-side at about 55 pc the effect of splitting up an equally bright binary is shown.

correction.

For the extinction correction (dereddening) we used an analytical homogeneous dust model based on Vergely et al. [1998] with no dust in the local bubble up to 70 pc distance and a constant dust density within 55 pc distance from the Galactic plane. The extinction is depicted as red lines in figure 2.10. For stars above 52° it is zero (the lower red line) and for stars in the Galactic plane it linearly increases for stars with distances above 70 pc and reaches a maximum value of 0.26 A_V at 250 pc (the upper red curve). In figure 2.10 the extinction correction is illustrated for an hypothetical star with VMag $= 0.6$ (which was calculated from the Vmag and the distance without dereddening) and a distance of 175 pc in the Galactic plane. Because the true VMag would be around 0.15 mag brighter we increase its VMag by that amount, so that the star will be associated to the right VMag bin, when applying the magnitude and distance cuts. In our example, as depicted in figure 2.10, the star would not be included into our volume-complete sample without extinction correction. Since its true VMag is below 0.5 mag including it into the 200 pc sphere is more accurate. Overall, the star counts only change for the 200 pc sphere, however it should be noted that the 10 % increase is much more significant than the binary correction. The assumption of a homogeneous dust distribution is inaccurate, at least when considering the Solar Neighbourhood. Therefore extinction data should be preferred over simple analytical models when correcting the light absorbing effect of interstellar dust.

In order to get a local number density from the star counts in different VMag bins we divided each magnitude bin with the corresponding volume, $\frac{4}{3}\pi d_{lim}^3$ (cf. equation 30 and figure 3.1), and also correct for the scale height dilution (young stars being confined to the Galactic plane because they are formed from the gaseous disc which has a very low scale height). The correction for scale height dilution introduces a model-dependency, but otherwise the large 200 pc volume can not be correctly interpreted in terms of local stellar number densities. On larger scales, structures like the spiral arms or the radial density distribution of stars across the Galactic disc, need to be taken into account as well.

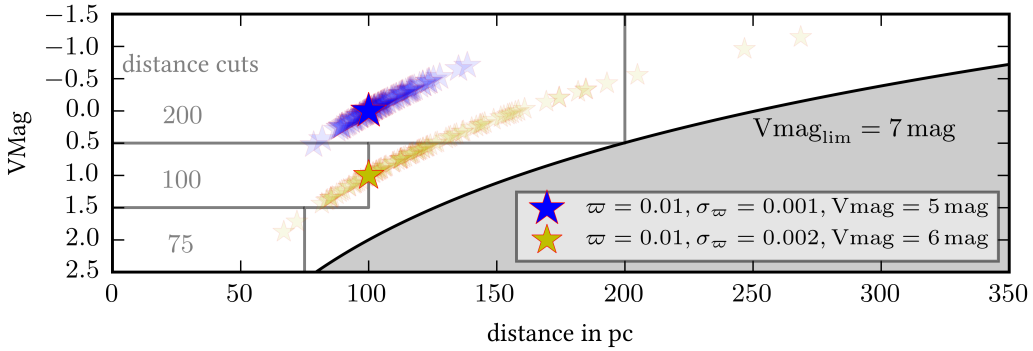

Figure 2.11: 100 realisations of two hypothetical stars with measured parallax of 0.01, associated error and Apparent V magnitude, are shown in the Absolute V magnitude and distance space. The blue star has a Vmag of 5 mag and a relative parallax error of 10%. The yellow stars is one magnitude fainter and its error is twice as large. The posterior PDF from which the samples are drawn were calculated using the exponentially decreasing volume density prior, $P_{\mathrm{d^2e^{-d}}}$ from equation 24, with a length scale of $L = 100$.

2.2.3 PROBABILISTIC DISTANCES

As argued in section 2.1, parallaxes are very useful measurements, when inferring distances, because they make no assumptions about the intrinsic properties of the observed object. Still, inferring distances can only be done probabilistically and the error is also propagated into the Absolute V magnitude[7]. Since distance and VMag are used to limit the star counts in the different volume-complete samples, it is important to account for the parallax error. The following method was used in Just et al. [2015] to assess the systematic error that was made compared to the previous two methods.

First, the posterior distance distribution is calculated for each star in the Hipparcos catalogue from the measured parallax and its associated error as described in section 2.1.
Then, in order to propagate the error to Absolute V magnitude, an appropriate number (we used 100) of sample distances is drawn from the posterior.
From each star's Apparent V magnitude and its 100 sampled distances 100 associated VMags are calculated (as depicted in figure 2.11 for two hypothetical stars with a measured parallax of 0.01, associated relative parallax errors of 10 and 20 % and Apparent V magnitudes of 5 and 6 mag).
In the next step the distance and Absolute V magnitude cuts are applied to the 100 times oversampled Hipparcos catalogue. Figure 2.11 illustrates that for stars with high relative error (like the yellow star) the 100 realisations are distributed across several magnitude bins with significant fractions falling into the second, first, zeroth Absolute V magnitude bin and considerable parts are even outside of the sample, either because they are too faint and (or) too far. In this context it is important to note that even for stars with relatively small relative error (blue star) the borders to other magnitude bins are easily crossed.
In a last step the star counts of each magnitude bin are divided by 100 in order to normalise

7 The error of the measured Apparent V magnitude should also be propagated into the distance error, however it is so small that its effect on the distance error can be neglected compared to the parallax error.

the star counts to the correct level.

The advantage of this method is that the sampled probability distribution of all stars is considered and weighted into the final result. There is no need to exclude stars with high fractional parallax error. Also the Trumpler and Weaver [1953] bias[8] is accounted for, because the error contribution from all stars of the Hipparcos catalogue (outside and inside the limiting distances) is sampled, and the catalogue does not have a sharp apparent magnitude limit[9].
This method can of course be combined with the binary and extinction correction from the previous subsection, but we will now show improved methods to account for these two effects.

2.2.4 USING INHOMOGENEOUS EXTINCTION DATA

Extinction maps have long been available [Schlegel et al., 1998], but in 3D only recently high resolution maps were published. An early attempt was a 3D map from Marshall et al. [2006] but they were interested mainly in the bulge so the sky coverage is confined to a small stripe along the Galactic plane and the local distance resolution is too coarse to be useful for our assessment. In Lallement et al. [2014] excellent 3D maps with high local resolution were presented but data were not published yet. A very good extinction data base was released recently by Green et al. [2015] and put up online. It uses the Pan-STARRS 1 (PS 1) photometry of 800 million stars and matches Two Micron All Sky Survey (2MASS) photometry of 200 million stars. The PS 1 survey covers three quarters of the sky with major parts of the Galactic plane (with most of the extinction) being included.
When combining this method with the probabilistic distances, the Absolute V magnitude of every realisation needs to be dereddened separately. Similarly, Green et al. [2015] is not giving single estimates of the extinction in a specific distance bin but samples of 100 or 500 from their posterior PDF.
In figure 2.12, the effect of light-absorbing dust clouds is illustrated on the visibility of a star. Usually, the hypothetical star of 0.3 VMag would be visible out to 200 pc distance for a magnitude limited survey with $\mathrm{Vmag}_{\mathrm{lim}} = 7$ mag. But because the light of the star is weakened, additionally to the inverse square law, by the extinction within dust clouds, the visibility volume for stars with 0.3 VMag shrinks below 180 pc, right before the second dust cloud. This loss of volume, which depends on the line of sight extinction (can be different in all directions), should be accounted for when determining stellar densities.
Another effect is indicated (by the reddened colour of the light ray) in the sketch at the bottom of figure 2.12, namely the differential extinction of dust [Scheffler and Elsässer, 1992, pp.187]. Shorter wavelength are preferentially scattered which is why light retains a larger fraction of red light when passing through a cloud of dust. This is why sometimes extinction and reddening are used synonymously in astronomy.

8 The bias is due to the error volume outside of the limiting distance being larger than inside. So more stars are scattered into the sample, if we assume constant stellar density, than out of it.

9 Otherwise, not many stars outside of the distance limit will be included in the catalogue data, which is why we encourage conservative distance cuts.

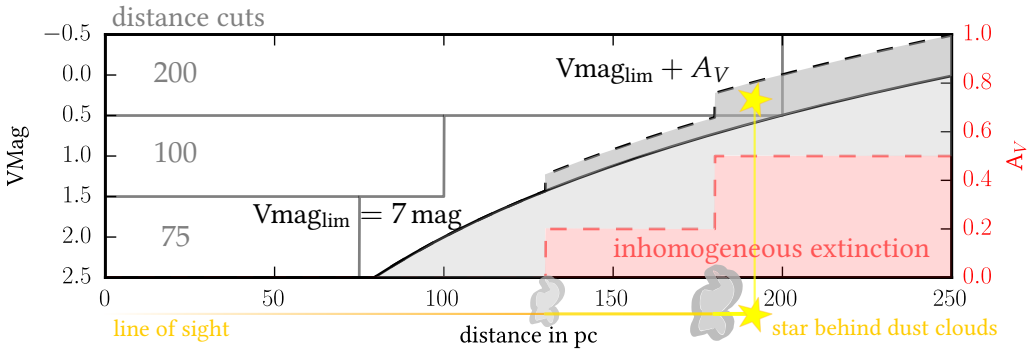

Figure 2.12: This is a zoom-in of figure 2.9 with an additional extinction scale on the right indicating the effect of two dust clouds at 130 pc and 180 pc in the line of sight between the observer and a hypothetical star of 0.3 VMag at 190 pc. The first, smaller, cloud has an extinction of $A_V = 0.2$ mag and the second an extinction of $A_V = 0.3$ mag. Their cumulative effect on the line of sight extinction is shown in dashed red and on the decreased volume covered by the magnitude limit in dashed black. The star would usually be bright enough to be seen by the survey and included into the 200 pc sample. Because of the strong extinction its apparent magnitude is above Vmag$_{lim}$ = 7 mag and therefore no longer in the 100 % completeness limit of the survey.

2.2.5 PROBABILISTIC BINARY CORRECTION

If we want to infer the stellar number density, with binaries resolved into individual stars, as opposed to the system number density, we need to correct for binaries. Once they are known and the magnitude difference is determined, we can split them up as mentioned in subsection 2.2.2. The problem, however, is that for O/B-stars the detection rate of binaries is very low (because of their fast rotation their spectra are broadened) though the binary rate itself is almost 100 %.
In this case again, we can use a probabilistic approach for stars where binaries are hard to detect. We can assign probabilities to a star of being an undetected binary (or even higher multiple stellar system) and sample the probability space of their mass ratios. When assuming that they have the same age and metallicity, isochrones can be used to assign new VMags and $B - V$ colours.
Of course these additional samples increase the data volume we are working with. For Hipparcos this might still be feasible, for Gaia it will probably not. Maybe a median effect of binaries on the stellar densities can be determined probabilistically and then corrected for with simpler methods. Forward modelling could also be more feasible (section 2.2.7), where binaries are modelled and the data is matched with synthesised observations.

2.2.6 RELAXING COMPLETENESS

When comparing Hipparcos and Tycho 2[10] star counts in bins of Vmag, the completeness according to Hipparcos for different apparent magnitudes can be determined. As displayed in figure 2.13 the Hipparcos catalogue is complete until Vmag = 7 mag (and not as the quoted Vmag = 7.3 − 9 mag from Perryman et al. [1997]), slowly declining to 80 % completeness

10 Which is complete up to 11 Vmag.

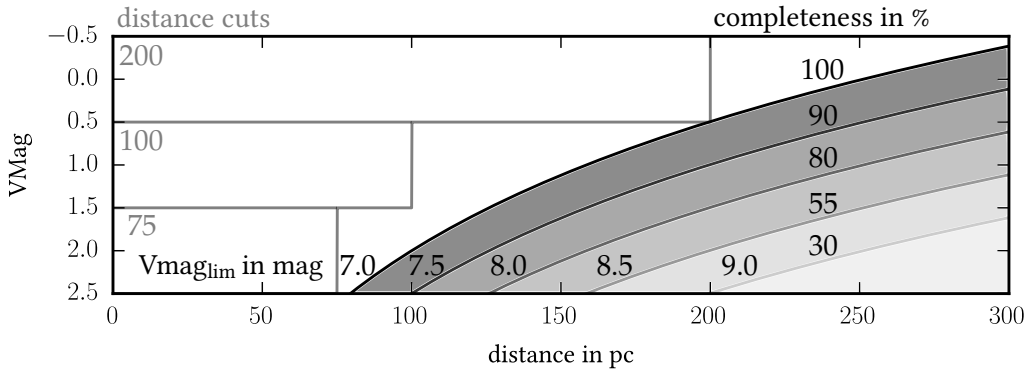

Figure 2.13: Zoom-in of figure 2.9 now with different Apparent V magnitude limits and the corresponding completeness in percent as calculated for Hipparcos compared to Tycho 2.

at 8 Vmag, and going down to 30 % at 9 Vmag[11]. When extrapolating star counts up from 55 %, corresponding to Vmag $= 8.5$ mag, the limiting distance is doubled compared to the 100 % completeness, which results in an eightfold volume coverage. Of course this gain will only be possible where there is no extinction. In reality the distance-completeness depends on the extinction, as was explained in section 2.2.4 and can be seen in figure 2.12. A hybrid method could be used to account for the distorted visibility volume, due to interstellar extinction, and also to increase the magnitude limit, by extrapolating star counts. Loss of completeness is stronger for stars that are redder and for stars closer to the Galactic plane, which indicates a preferential loss of stars with higher reddening. A possibility to account for this bias is to make the completeness comparison with Tycho 2 not only in bins of Vmag but also in colour and Galactic latitude.

2.2.7 MODELLING A MAGNITUDE LIMITED SAMPLE

With a Galaxy or disc model in the background, a magnitude limited sample can be modelled theoretically and compared directly to the observations. The latest Besançon Galaxy model (Besançon model) is also able to synthesise binaries. With a forward modelling approach, the local stellar density could be used as a free parameter and changed until a best fit between the mock observations and the data is found. The downside of this method is that there are many systematics and degeneracies due to model dependencies. We have the IMF, Star Formation History (SFH), Age Velocity-dispersion Relation (AVR), and stellar evolutionary tracks, which can all bias our determination. Moreover, our mock observations, as well as the real data, will be a random realisation of an underlying true PDF, which in the case of the model can be approximated via averaging, and in the case of the real data will always include Poisson noise.

This concludes the section on deriving stellar number densities and the chapter on statistical inference. In the next chapter volume-complete stellar samples will be used to infer properties of the stellar IMF, using a vertical local Galaxy model.

11 With a slight dependence on colour and Galactic latitude, but not as strong as claimed by Perryman et al. [1997].

Part II

MILKY WAY DISC MODEL INFERENCE

Using star counts and elemental abundances together with the JJ-model to redetermine the stellar IMF and chose the best set of stellar yields.

3

THE LOCAL INITIAL MASS FUNCTION, AS DERIVED FROM STAR COUNTS

In this chapter, building up on the methods described in the previous chapter, I will infer the stellar Initial Mass Function parameters using the vertical Milky Way disc model of Just and Jahreiss [2010], together with local Solar Neighbourhood stars with accurate parallaxes. Most of the content has been published in Rybizki and Just [2015], but a few post-publication findings are added (mainly into the discussion, section 3.6, with two new subsections), as well as further references.

3.1 INTRODUCTION

The stellar Initial Mass Function (IMF) has seen numerous re-determinations since the seminal work of Salpeter [1955]. The most popular IMF forms are broken power-laws [Scalo, 1986; Kroupa et al., 1993], lognormal with a Salpeter-like high-mass slope Chabrier [2003] (Chabrier 03), or, more recently, tapered power-laws [Parravano et al., 2011], which are similar to Chabrier 03 but result in more low-mass stars. Originally, the IMF was derived by the Luminosity Function (LF) of the Solar Neighbourhood via luminosity-mass relations and stellar lifetimes. More sophisticated derivations account for the Star Formation History (SFH) [Schmidt, 1959] and the scale height dilution [Miller and Scalo, 1979] of the observational sample.

Another, more direct approach is to look at young stellar clusters and derive an IMF from these spatially and temporally confined starburst populations. This yields a range of different IMFs [van den Bergh and Sher, 1960; Dib, 2014], which are not necessarily in conflict [Weidner and Kroupa, 2005], with a global IMF being able to describe the field stars in the Milky Way (MW) disc. Here we get hold on the theoretical concept of a time-independent local MW IMF by exploring its effect within our disc model in the realm of observables.

This chapter is based on a series of papers, which started with Just and Jahreiss [2010] (paper I), where a local, vertical MW disc model was constructed, using dynamical constraints of Main Sequence (MS) stars. The main advantage of this method is its weak dependence on the assumed IMF, as only the integrated mass-loss enters the dynamical model. Other determinations, as for example Haywood et al. [1997], have a degeneracy of their derived SFH and the high-mass slope of their IMF. As a result, the old Besançon model [Robin et al., 2003], using the constant SFH from Haywood et al. [1997], had to be revised recently [Czekaj et al., 2014] to a decreasing one, in line with different determinations from chemical evolution models [Chiappini et al., 1997], extragalactic trends [Ly et al., 2007; van Dokkum et al., 2013] and dynamical constraints [Aumer and Binney, 2009; Just and Jahreiss, 2010].

In Just et al. [2011] (paper II), the disc model was further constrained by comparing Sloan Digital Sky Survey [York et al., 2000] (SDSS) data with predicted star counts at the North

Galactic Pole (NGP). This yielded the MW disc model [Just and Jahreiss, 2010] (JJ-model) with a fixed SFH and a well-defined local thick disc model. The agreement between the model and the NGP data is very good, which was also confirmed in Czekaj et al. [2014].

After fixing the SFH, Age Velocity-dispersion Relation (AVR) and Age Metallicity Relation (AMR), we now want to further build up a consistent disc model by constraining the fiducial IMF, using local star counts, and taking into account turn-off stars and giants as well. In paper I, the Present-Day stellar Mass Function (PDMF) was already converted into an IMF, taking into account scale height correction and finite stellar lifetimes. Binaries and reddening were not accounted for, producing a very steep high-mass slope with $\alpha = 4.16$, which is also related to a relatively high break in the two-slope power-law, at $1.72\,M_{\odot}$.

In this chapter, we select volume-complete stellar samples from the revised Hipparcos [Perryman et al., 1997] (Hipparcos) [van Leeuwen, 2007], and an updated version of the Catalogue of Nearby Stars (CNS)4 [Jahreiss and Wielen, 1997] (which will soon be published as CNS5), also giving us a sound statistical sample to investigate the local stellar mass density (see discussion in sec 3.5.3). We use Galaxia [Sharma et al., 2011] (Galaxia) to create mock observations from the JJ-model with arbitrary IMFs. We find a new fiducial IMF, describing the data by sampling the two-slope broken power-law parameter space, using a Markov Chain Monte Carlo (MCMC) technique. Given the data, the model likelihood is approximated, assuming discrete Poisson probabilities for different magnitude bins, differentiating between dwarfs and giants.

A similar determination of the IMF was done in the Besançon update of Czekaj et al. [2014], with matching results. Instead of local LFs, they used the colour projections of Tycho 2 catalogue [Hoeg et al., 2000] (Tycho 2) data in different directions to determine their best fit. Their modelling machinery is very modular, being able to incorporate different stellar evolutionary and atmosphere models, as well as accounting for binarity or reddening from the model side. On the other hand, they do not calculate a likelihood, but use a χ^2 summary statistic. Since they have so many degenerate free parameters, they do not explore the full IMF parameter space, but test pre-determined ones from the literature together with other parameters of their Galaxy model.

Overall, the sophisticated approach with a concordance Galaxy model in the background able to produce mock observations to test theoretical concepts, like the IMF, is a very promising technique. Especially with the underlying physical models getting more and more refined with increasing observational evidence. One unsolved problem, which is also pointed out by Czekaj et al. [2014] is missing detailed 3D extinction data of the local InterStellar Medium (ISM).

In section 3.2, we explain how to create mock observations from our vertical disc model using Galaxia. Section 3.3 describes the reduction of Hipparcos and CNS data to obtain our observational sample, followed by section 3.4 on the likelihood determination in the IMF parameter space. The results are then presented in section 3.5 together with a comparison to widely used IMFs. In section 3.6, the results are put into context, followed by the conclusions in section 3.7.

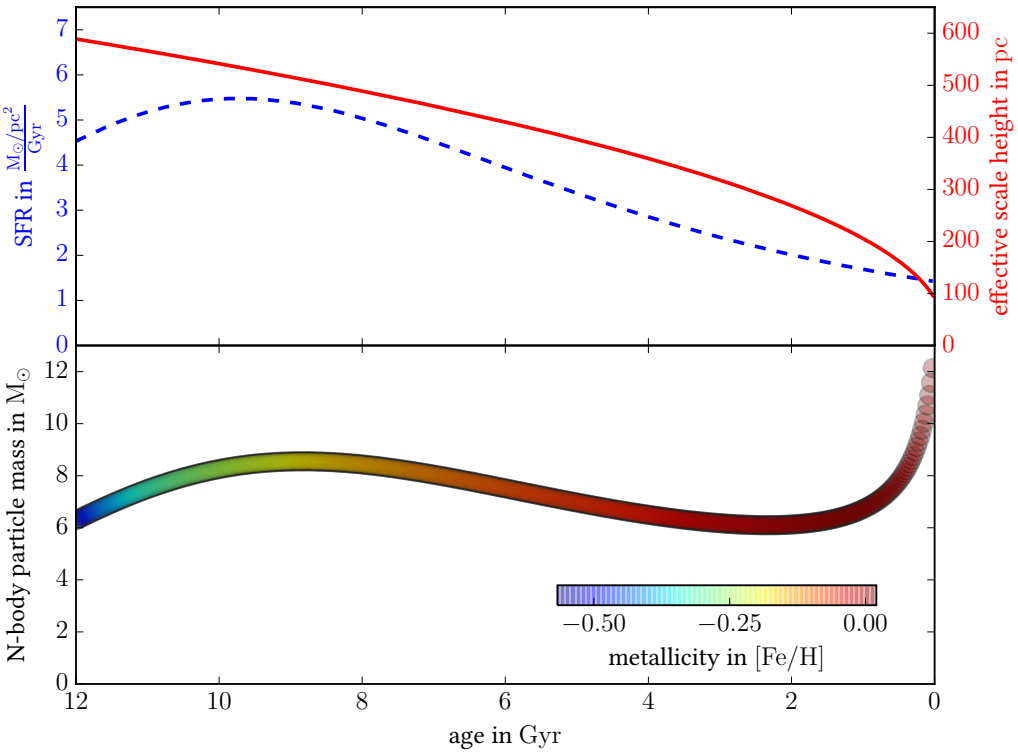

Figure 3.1: The upper panel shows in dashed blue the global SFH and in solid red the effective scale height of the JJ-model (at Solar Galactocentric distance).
In the lower panel the input N-body data, which is passed to Galaxia to create the 25 pc sphere, is displayed. The age, mass and metallicity of each SSP are visualised.

3.2 SYNTHESISING A LOCAL DISC MODEL

In paper I, a self-consistent dynamical, vertical MW disc model was developed. Combined with constraints from star counts of the NGP in paper II, a fiducial disc model (JJ-model) was chosen. The JJ-model fixes the SFH, the AVR, a simple Chemical Enrichment Model (CEM), and from that predicts the stellar vertical disc structure in terms of kinematics, star counts, ages and metallicities as functions of distance to the Galactic plane.
In order to obtain mock observations of the Solar Neighbourhood, we turn our vertical disc model into a local representation, used as an input for Galaxia to synthesise stellar samples.

3.2.1 THE DISC MODEL LOCALLY

As we want to compare our JJ-model to volume-complete stellar samples in the Solar Neighbourhood, we construct seven spheres that are disjunct in Absolute V magnitude (VMag), and have heliocentric distances from 20 to 200 pc (see table 1 & 2 for detailed limits). In the following, we explain how we prepare N-body particle representations of our model for each sphere such that Galaxia can turn them into mock observations.

As our model is evolved over 12 Gyr in 25 Myr steps, we construct 480 N-body particles (plus one for the thick disc) with specific ages, masses and metallicities for each sphere

separately. These are passed to Galaxia, where each particle is turned into a Simple Stellar Population (SSP) according to a prescribed IMF. The two youngest SSPs are split up age-wise, so that the youngest stars coming from Galaxia are 6.25 Myr old. We assign arbitrary phase-space information to the particles, since the final observable is a local Colour-Magnitude Diagram (CMD) based on volume-complete subsamples.

We will now illustrate the construction of a local N-body representation of our model for the 25 pc sphere following figure 3.1.
The upper panel depicts the global SFH in units of surface density per time and the effective scale height, h_{eff}, over age for the JJ-model, respectively. From that a local mass density, ρ_0, for each SSP can be calculated, which then is multiplied with the volume of the 25 pc sphere, V_{25}, to obtain

$$M_{25\,pc}(t_i) = V_{25\,pc}\,\rho_0(t_i) = \frac{4}{3}\pi r^3_{25\,pc}\,\frac{SFH(t_i)\cdot 0.025\,Gyr}{2\,h_{eff}(t_i)} \tag{30}$$

which is shown in the lower panel of figure 3.1 as resulting N-body particle masses. Colour-coded, the AMR is depicted, which is also coming from the JJ-model as an analytic function, but with an added Gaussian scatter of 0.13 dex standard deviation (tested with Geneva Copenhagen Survey [Nordström et al., 2004] (GCS) data, cf. fig. 15 of paper I).

For the thin disc, 3552 $M_\odot$ ($\mathcal{M}_{IMF,thin,25\,pc}$) in particle mass is passed to Galaxia for the 25 pc sphere

$$\mathcal{M}_{IMF,thin,25\,pc} = \int_{0\,Gyr}^{12\,Gyr} M_{25\,pc}(t)\,dt \simeq \sum_{i=1}^{480} M_{25\,pc}(t_i). \tag{31}$$

This is by construction of the JJ-model the gas mass that was used to create the thin disc stars (and in the meanwhile also remnants) still residing in the 25 pc sphere. Nowadays, only a fraction of that is left in stars, due to stellar evolution ($\mathcal{M}_{PDMF,25\,pc}$, cf. section 3.5.3). In the mass-age distribution of the N-body data, the peak from the global SFH (dashed blue line) around 10 Gyr can still be recognised. The increase for younger stellar populations stems from the decreasing effective scale height confining these stars closer to the Galactic plane (i.e. a bigger fraction of them is found in the local sphere, cf. fig. 14 of paper I).

The thick disc is implemented by inserting a single starburst (i.e. one SSP and equivalently one N-body particle) with 6.5 % of the thin disc mass

$$\mathcal{M}_{IMF,discs} = \mathcal{M}_{IMF,thin} + \mathcal{M}_{IMF,thick} = 1.065 \cdot \mathcal{M}_{IMF,thin} \tag{32}$$

12 Gyr ago and with a metallicity of [Fe/H] = -0.7, resulting in a present-day thick disc mass fraction of around 5 %. Since the local density of the stellar halo is negligible compared to the disc, we do not consider it as a separate component in this work.

A change in the IMF will affect the mass fraction remaining in the stellar component (cf. sec. 2.5 paper I), therefore we introduce a mass factor (mf), scaling our model's total mass ($\mathcal{M}_{IMF}$), which is distributed between $m_{low} = 0.08\,M_\odot$ and $m_{up} = 100\,M_\odot$, to fit the observed stellar mass density, $\mathcal{M}_{PDMF}$, such that

$$\mathcal{M}_{IMF} = mf \cdot \mathcal{M}_{IMF,discs}. \tag{33}$$

This is necessary because in paper I a Scalo-like IMF [Scalo, 1986] was used, with a different stellar evolutionary model [Fioc and Rocca-Volmerange, 1997] and also an independent local stellar mass density normalisation [Jahreiss and Wielen, 1997].

When going to larger heights above the Galactic plane, we also need to correct for decreasing vertical density profiles. For the 25 pc sphere, the deviation from a homogeneous density distribution is still negligible but this changes with larger spheres and especially with young stellar populations. For example when rescaling the star count in the highest magnitude bin in table 1 with a mean age of 0.1 Gyr, the number must be increased by 54 % to account for the low scale height of these stars (cf. figure 2 in paper II).

3.2.2 MOCK OBSERVATIONS WITH GALAXIA

Galaxia is a tool to generate mock catalogues from either analytic models or N-body data. It already has a default model, which is similar to the old Besançon model [Robin et al., 2003], but the updates [Robin et al., 2012; Czekaj et al., 2014; Robin et al., 2014] are not implemented yet.

In the previous subsection, we constructed particles representing our model locally, which we now pass for each sphere separately to Galaxia, together with the disjunct VMag limits building up a CMD successively.

So far Galaxia uses Padova isochrones [Marigo et al., 2008], which have problems in reproducing the lower end of the MS and the Red-Clump (RC). We include their revised templates [Bressan et al., 2012, PARSEC version 1.2 S[1]], where only minor differences at low-mass stars persist (cf. lower MS in figure 3.2). This remaining discrepancy is also pointed out in Chen et al. [2014, fig. A3], but should have only a negligible effect on the star counts in our used magnitude range.

Binaries, White Dwarf (WD)s or other remnants are not implemented in Galaxia yet but an update is being planned (private communication, Sharma 2015). When inspecting the CMD in figure 3.2 a second blue-shifted MS of subdwarfs in the synthesised catalogue is visible which comes from our distinct thick disc metallicity.

Beside being able to change the IMF from which Galaxia is distributing the particle masses into stars, we are using it as a black box. Specifying a photometric system will already yield a detailed stellar catalogue[2] in terms of a random realisation of our local model representation as for example depicted in figure 3.2 for our newly determined IMF.

3.3 OBSERVATIONS

The anchoring point for every Galaxy model in terms of observational constraints is the stellar distribution in the Solar Neighbourhood since detailed and volume-complete samples can only be obtained here. After using the vertical component of the velocity distribution of MS stars in paper I (dynamical constraint) and the SDSS NGP star counts in paper II (vertical density distribution constraint) we now use absolute local stellar densities for dwarf and giant stars.
This is achieved by constructing different samples combining absolute magnitude cuts and

1 http://stev.oapd.inaf.it/cgi-bin/cmd
2 See http://galaxia.sourceforge.net/Galaxia3pub.html for detailed instructions

Table 1: Observational sample and mock catalogues - dwarf stars

Catalogue	d (pc)	M_V-limits (Mag)	N_{fin} #	$\frac{\sigma_\pi}{\pi} > 15\,\%$ # lost	CNS5 25 pc	N_{25} rescaled†	JJ_{25} to 25 pc	log-likelihood $\ln(\mathcal{L}/P_{max})$	Mean mass $M_\odot$	Mean age Gyr
	200	],-1.5]	98	0	0	0.28	0.13	-21.9	6.4	0.1
	200	[-1.5,-0.5]	233	3	1	0.62	0.63	0.00	4.0	0.2
	200	[-0.5,0.5]	901	12	4	2.26	2.60	-9.20	2.9	0.3
Hipparcos	100	[0.5,1.5]	520	2	15	8.61	9.09	-0.76	2.2	0.5
	75	[1.5,2.5]	677	1	27	25.6	24.4	-0.81	1.7	1.0
	50	[2.5,3.5]	518	1	62	65.1	59.9	-1.79	1.4	2.3
	30	[3.5,4.5]	200	0	110	115.7	146.5	-5.90	1.1	5.3
	25	[4.5,5.5]	191	4	191	191	190.3	0.00	0.9	6.1
	25	[5.5,6.5]	198	11	198	198	207.9	-0.22	0.8	6.4
CNS5	25	[6.5,7.5]	193	16	193	193	196.0	-0.02	0.7	6.5
	25	[7.5,8.5]	207	13	207	207	205.3	-0.01	0.6	6.6
	20	[8.5,9.5]	139	15	245⋆	271.5	258.0	-0.20	0.5	6.7
total		],9.5]	4075	78	1253	1278.8	1300.8	-40.8	0.8	6.0

Catalogue gives the source catalogue, *d* gives the heliocentric distance of stars included, *M_V-limits* gives the magnitude range of each bin, *Nfin* is the final star count in each bin, *$\frac{\sigma_\pi}{\pi} > 15\,\%$* is the number of stars thrown out due to high distance errors, *CNS5* gives the number of stars within the volume-complete 25 pc sphere, the next two columns give the star counts of the observations and our JJ-model rescaled to 25 pc. The JJ-model with newly determined IMF is averaged over 400 random realisations, *log-likelihood* shows the probability of each bin after equation 35 normed with the maximal possible probability (cf. section 3.4.1) in natural logarithm which indicates each bin's impact on the likelihood function, the *mean mass* and *mean age* show the values for the corresponding JJ magnitude bins where the sum at the bottom is an average of all stars within 25 pc.

⋆for this magnitude bin volume-completeness is not given so the 139 stars from the 20 pc sphere have been rescaled to 25 pc yielding 271.5 stars which is 10 % more than the 245 stars observed in the 25 pc sphere

†rescaling the volume and accounting for the density profile of the magnitude bin's mean age population

Table 2: Observational sample and mock catalogues - giant stars

Catalogue	d (pc)	M_V-limits (Mag)	N_{fin} #	$\frac{\sigma_\pi}{\pi} > 15\,\%$ # lost	CNS5 25 pc	N_{25} rescaled†	JJ_{25} to 25 pc	log-likelihood $\ln(\mathcal{L}/P_{max})$	Mean mass $M_\odot$	Mean age Gyr
	200	],-1.5]	74	1	0	0.16	0.14	-0.87	3.4	1.6
	200	[-1.5,-0.5]	375	2	1	0.77	0.84	-1.47	1.8	4.4
	200	[-0.5,0.5]	1341	20	3	2.78	2.29	-23.4	1.7	3.9
Hipparcos	100	[0.5,1.5]	526	0	6	8.33	9.27	-3.03	1.5	4.8
	75	[1.5,2.5]	126	0	5	4.70	3.76	-2.99	1.2	6.3
	50	[2.5,3.5]	62	0	7	7.77	11.6	-5.55	1.2	6.6
	30	[3.5,4.5]	9	0	6	5.21	7.11	-0.34	1.0	8.8
total		],4.5]	2513	23	28	29.7	35.0	-37.7	1.3	6.3

Table 3: Effect of binarity and dereddening on the star counts

Radius of sphere [pc]	30	50	75	100	200
Magnitude bin [VMag]	4th	3rd	2nd	1st	<0.5
No correction	204	591	793	1052	2798
Binary correction	209	580	803	1046	2756
Extinction correction	204	591	793	1053	3060
Both corrections (N_{fin})	209	580	803	1046	3022

heliocentric distances such that the selected stars represent a volume-complete sphere. At the bright end we go up to 200 pc in order to obtain enough massive stars and giants to have reliable statistics. Our observational sample consists of stars from the extended Hipparcos catalogue [Anderson and Francis, 2012] and the CNS. A statistically more robust technique to construct volume-complete samples (taking into account the parallax error and without the necessity to exclude stars with poor parallaxes) was tested for Just et al. [2015] and is presented in section 2.2.
Fundamentally, we would like to implement all observational biases on the models side and compare the synthesised mock observations to unaltered observables. In this respect the updated Besançon model [Czekaj et al., 2014] has pushed the link between model and data in the right direction by implementing extinction models and a scheme for binary systems into their model. As Galaxia is not able to account for binaries yet and we are not providing positional information with the N-body particles we have to treat binaries and dereddening from the observational side.

3.3.1 HIPPARCOS

We use the extended Hipparcos compilation (117955 entries) which cross-matches the original stars from the revised Hipparcos catalogue [van Leeuwen, 2007] with other data sources. By using heliocentric distance and VMag cuts, similar to table 1 of paper I we obtain volume-complete observational spheres for different stellar magnitudes going down to 4.5 VMag. The only further selection criteria to eliminate misidentifications is a distance error below 15 % which reduces the sample insignificantly as visible in tables 1 & 2.
Before the VMag and distance cuts are applied, all stars (or better *stellar systems* represented by only a single entry in Hipparcos), which have both a binary flag and a Δmagnitude (Δmag) entry in the original Hipparcos catalogue [ESA, 1997], are split up into two components. The binary correction changes the number of stars in each distance bin slightly (see table 3).

With the binary correction we have 5394 stars in the Hipparcos sample of which 552 entries come from split up binary systems. On average the bins lose stars when correcting for binaries because the single components get fainter than the system bringing these stars below the magnitude limit. As the fainter magnitude bins have smaller limiting radii only a fraction of 'lost' stars fall into the fainter magnitude bins.
On scales of the investigated volume the ISM is in-homogeneously distributed with Ophiuchus and Taurus molecular cloud being the biggest absorbers in the 200 pc sphere [Schlafly et al., 2014]. 3D extinction maps with appropriate resolution are getting published [Lalle-

ment et al., 2014; Green et al., 2015] but the data are not available yet or do not cover the whole sky. In order to deredden our stars we adopt an analytic model from Vergely et al. [1998] describing a homogeneous extinction depending on the distance and Galactic latitude. Due to the local bubble we set the extinction to zero below 70 pc distance and above 52° Galactic latitude (cf. Vergely et al. [1998, fig. 4, 11]).

Aumer and Binney [2009] also adopted this model but only within 40 pc of the Galactic mid-plane resulting in 4 % less stars in the 200 pc sphere compared to our adaptation of the extinction model. We use the Vergely et al. [1998, p.548] cosecant law for the color excess,

$$E_{B-V}(d,b) = \begin{cases} 0, & d < \mathrm{d}_0 \vee b > 52^\circ \\ \mathrm{E}_0(d - \mathrm{d}_0), & \text{if} \quad d < \frac{\mathrm{h}_0}{|\sin(b)|} \\ \mathrm{E}_0\left(\frac{\mathrm{h}_0}{|\sin(b)|} - \mathrm{d}_0\right), & d > \frac{\mathrm{h}_0}{|\sin(b)|} \end{cases} \tag{34}$$

with $\mathrm{h}_0 = 55$ pc, $\mathrm{d}_0 = 70$ pc, $\mathrm{E}_0 = 0.47 \frac{\mathrm{mag}}{\mathrm{kpc}}$ and d, b being the heliocentric distance and the Galactic latitude. To transform from colour excess to extinction (A_V) we adopt the canonical $\frac{A_V}{E_{B-V}} = R_V = 3.1$ [Scheffler and Elsässer, 1992, p.190], which results in a maximum extinction $A_V \approx 0.19$ mag in a distance of 200 pc, close the Galactic plane.
In essence, the dereddening leaves the closer samples unaltered only increasing the 200 pc sample star count by ∼10 %. This is due to the photometry of stars, with a heliocentric distance between 100 and 200 pc, becoming brighter after extinction correction and thereby satisfying the magnitude limits.
As the ISM is highly inhomogeneous, adopting an analytic model is only a crude approximation but the best we can do at the moment. In the future we want to redo the analysis with upcoming 3D extinction maps, like for example Green et al. [2015].

3.3.2 CATALOGUE OF NEARBY STARS 5

The Hipparcos sample is supplemented with stars from CNS5 (7251 entries) for fainter magnitudes ($4.5 - 9.5$ VMag), which is a volume-complete catalogue for stars brighter than 8.5 (9.5) VMag up to a distance of 25 (20) pc.
The distances of the stars are calculated from parallaxes (when advisable the photometric parallaxes were preferred to the trigonometric) with a correction for the parallax bias [Francis, 2013] according to equation 1 in Anderson and Francis [2012], which was also used for stars in the Hipparcos catalogue.

The 20 pc sample includes 139 stars from 8.5 to 9.5 VMag, after excluding 2 WDs and 15 stars with relative distance errors above 15 %. For the 25 pc sphere the VMag ranges from 4.5 to 8.5. Here 44 stars have a too high error so that 789 stars remain in the final sample. All together 928 stars originate from the CNS5, of which 372 are in resolved multiple stellar systems (24 of the remaining 556 'single systems' are detected spectroscopic binaries). Of the 372 stars in multiple stellar systems 117 mostly primary and 87 mostly secondary components share a joint B-V value but have individual VMag entries so that they can be corrected by putting them on the MS. The MS was empirically assigned from MS stars with low parallax error.

In the end three stars reside in the CNS5 sample as well as in the Hipparcos sample because of slightly different VMag values directly at the VMag borders of 4.5 VMag. Those stars are

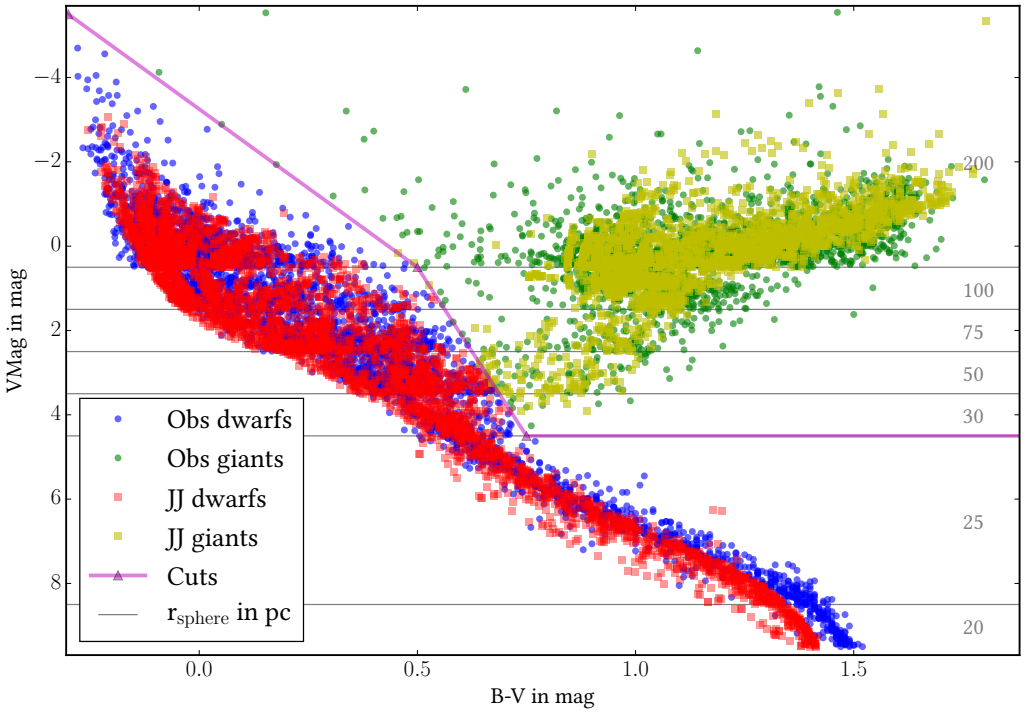

Figure 3.2: Colour-magnitude diagram of the observational sample (Hipparcos stellar systems are not split up) and one random realisation from the JJ-model with the newly determined IMF. The cuts with connected triangles at (B-V,M_V) = (-0.3,-5.5), (0.5,0.5), (0.75,4.5) and (3,4.5) for the division into dwarf and giant sample are indicated in magenta. On the right, the different sphere radii are written in units of pc.

excluded from the Hipparcos sample so that in our joint sample every star has a unique entry.
As a comparison to the Hipparcos sample we also list the 247 volume-complete (within 25 pc) CNS5 stars which are brighter than 4.5 VMag in table 1 and 2. The only peculiarity is the 2σ outlier with 15 against 8.65 expected stars in the 100 pc bin of the dwarf sample. Even the CNS5 sample can be seen as a valid random realisation of the enlarged Hipparcos sample.

3.4 STATISTICAL ANALYSIS

For our analysis we divide the derived CMDs into dwarf and giant stars with the cuts specified in figure 3.2. Since MS stars have a tight correlation between luminosity and stellar mass the dwarf sample contains information on the PDMF. The giant sample adds constraints for the integrated SFH and the IMF of higher mass stars (above 0.9 $M_\odot$).
To compare our observable (the LF) to a theoretical IMF we feed local representations of our model together with different IMFs to Galaxia leaving us with synthesised star counts from which we construct a likelihood assuming discrete Poisson processes (section 3.4.1). This is implemented into a MCMC scheme to obtain a representation of the Probability Density Function (PDF) in the two-slope IMF parameter space (section 3.4.2).

3.4.1 LIKELIHOOD CALCULATION

We approximate the likelihood of our model given the data by dividing each CMD into 12 magnitude bins for the dwarf sample and 7 for the giants (see table 1 & 2) and calculate the discrete Poisson probability distribution. The expected value is coming from our model (m_i) and the number of occurrences is the star count observed in each bin (d_i) leading to the likelihood

$$\mathcal{L}_{\text{total}} = \prod_{i=1}^{12+7} \mathcal{L}_i, \text{ where } \mathcal{L}_i = \frac{m_i^{d_i} e^{-m_i}}{d_i!}. \tag{35}$$

The log-likelihood then follows as:

$$\log \mathcal{L}_{\text{total}} = \sum_{i=1}^{12+7} \left(d_i \log(m_i) - \log(d_i!) - m_i \right). \tag{36}$$

For the calculation of the log factorial a very accurate approximation for $n > 0$ from Askey [1988, p. 339] is used:

$$\log n! \approx n \log n - n + \frac{\log\left(n(1 + 4n(1 + 2n))\right)}{6} + \frac{\log(\pi)}{2}. \tag{37}$$

We will normalise the log-likelihood with its maximal possible value, $\mathrm{P}_{\max} = -68.5$, occurring when the observed sample is tested with itself.
It should be kept in mind that a linear increase in star counts results in exponentially increasing penalties for our likelihood function, when the relative deviation remains constant. For example, if the expected value is 10 and the number of occurrences is 9, then we have a $\ln(\mathcal{L}/\mathrm{P}_{\max})$ of -0.04. For 100 expected stars and 90 occurrences $\ln(\mathcal{L}/\mathrm{P}_{\max})$ equals -0.46, for 1000 and 900 it is -5.1 and so forth. This on the one hand takes into account that bins with a lot of stars get a higher statistical weight but could also be dangerous when small systematic errors (which could come from a bad AVR or connectedly isochrones indicating wrong ages) result in large penalties for the likelihood potentially pointing our MCMC simulation to a biased equilibrium IMF parameter configuration.

3.4.2 SAMPLING THE LIKELIHOOD DISTRIBUTION

The variability of the outcome of Galaxia is twofold. First the IMF parameters can be varied changing the laws according to which the mock observations are produced. Second for fixed parameters the random seed of Galaxia can be changed yielding different random realisations. The latter can be minimised by averaging over many realisations. We over-sample each point in parameter space 400 times so that this noise is reduced by a factor of 20 (cf. tab 5) and should be a second order effect compared to the Poisson noise in the data (if we assume the observed stars have been randomly realised from an underlying probability distribution).

To sample the PDF of our parameter space we use a Python implementation [Foreman-Mackey et al., 2013] of an affine invariant ensemble sampler for MCMC [Goodman and Weare, 2010] where step proposals using the information of multiple walkers reduce the

autocorrelation time significantly.
Since the overall mass turned into stars ($\mathcal{M}_{\mathrm{IMF,discs}}$) could be slightly different to the JJ-model we add the mass factor (mf) as a fourth free parameter besides the three two-slope IMF parameters, low-mass index (α_1), high-mass index (α_2), and the power-law break (m_1). The functional form of the IMF is

$$\frac{\mathrm{d}n}{\mathrm{d}m} = k_\alpha m^{-\alpha} \begin{cases} \alpha = \alpha_1, & \text{if} \quad \mathrm{m_{low}} < m < \mathrm{m}_1 \\ \alpha = \alpha_2, & \quad\quad\; \mathrm{m}_1 < m < \mathrm{m_{up}} \end{cases} \tag{38}$$

with the lower and upper mass limit of the IMF $\mathrm{m_{low}} = 0.08\,\mathrm{M}_\odot$ and $\mathrm{m_{up}} = 100\,\mathrm{M}_\odot$ being fixed. The k_{α_i} ensure that the IMF is a continuous function at the power-law break (m_1) and normalises to unity in mass

$$\int_{\mathrm{m_{low}}}^{\mathrm{m_{up}}} m \frac{\mathrm{d}n}{\mathrm{d}m} \mathrm{d}m = 1, \tag{39}$$

such that it can be multiplied with the mass factor, mf, and the JJ-model mass, $\mathcal{M}_{\mathrm{IMF,discs}}$, to represent the gas mass turned into stars

$$\mathcal{M}_{\mathrm{IMF}} = \mathrm{mf} \cdot \mathcal{M}_{\mathrm{IMF,discs}} \cdot \int_{\mathrm{m_{low}}}^{\mathrm{m_{up}}} k_\alpha m^{-\alpha+1} \mathrm{d}m. \tag{40}$$

For each set of parameters we use the product of the likelihoods from the dwarf bins and the giant bins

$$\log \mathcal{L}_{\mathrm{total}} = \log \mathcal{L}_{\mathrm{dwarf}} + \log \mathcal{L}_{\mathrm{giant}} \tag{41}$$

to sample the parameter space. In this way the probability for each bin (12 from the dwarf sample and 7 from the giant sample), being an independent discrete Poisson process, is weighted equally into the final likelihood ($\mathcal{L}_{\mathrm{total}}$).

3.5 RESULTS

Here we present the newly determined fiducial IMF for the JJ-model. For comparison we also show the log-likelihood of the observational data with synthesised data generated from our model but using common IMFs from the literature.

3.5.1 NEW IMF PARAMETERS

Multiple burn-ins from different starting points all settling in the same equilibrium configuration suggest a well-behaved parameter space with respect to our likelihood calculation. We use 20 walkers each sampling 500 steps to generate the point cloud representing the PDF of the parameter space. For each step we average over 400 realisations. Figure 3.3 shows the marginalised likelihood distribution of each parameter as histograms on the diagonal and as point clouds for each parameter pair in the lower left. Just for illustrative reasons each dot is coloured to indicate high ($\mathrm{red_{max}}$ = -77.2) and low ($\mathrm{blue_{min}}$ = -86.7) log-likelihood values with grey dots being below this 3σ range. In the histograms the mean and the standard

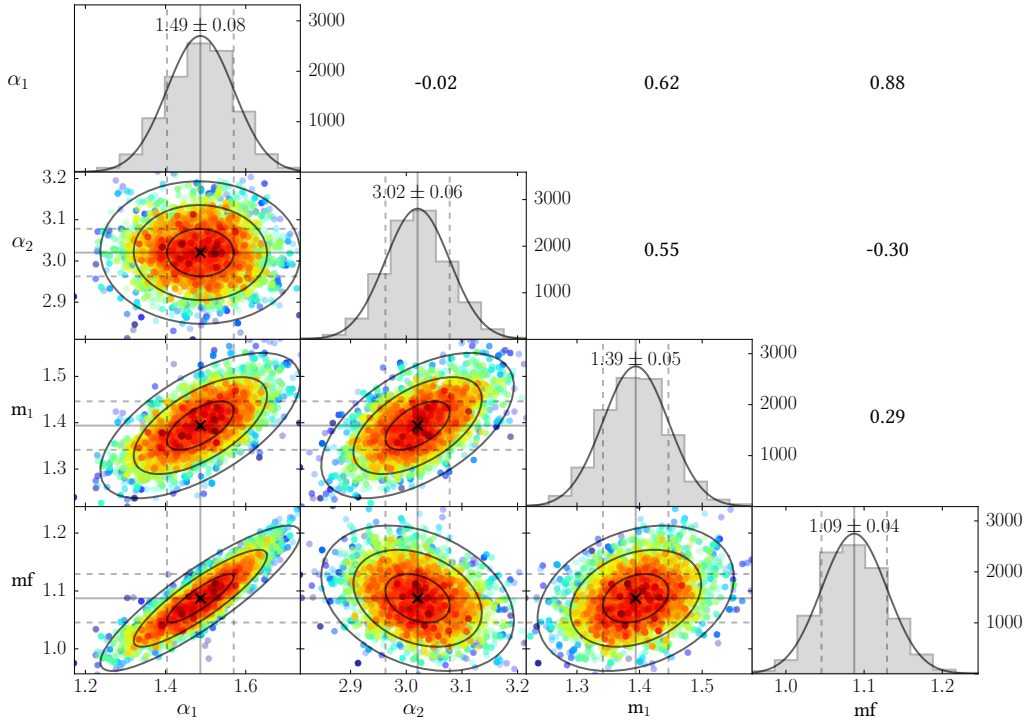

Figure 3.3: Marginalised parameter distribution of the MCMC run exploring the equilibrium distribution of the parameter space with respect to our log-likelihood using 10^5 evaluations. Each scatter plot shows the projected 2D parameter distribution with points coloured by likelihood increasing from blue to red. Crosses indicate the mean values and ellipses encompass the 1σ-3σ regions. The respective correlation coefficients are given at the position mirrored along the diagonal. Gaussian fits and histograms of the marginalised parameter distribution are given on the diagonal. The mean and standard deviation of each parameter is written and also indicated by solid and dashed grey lines.

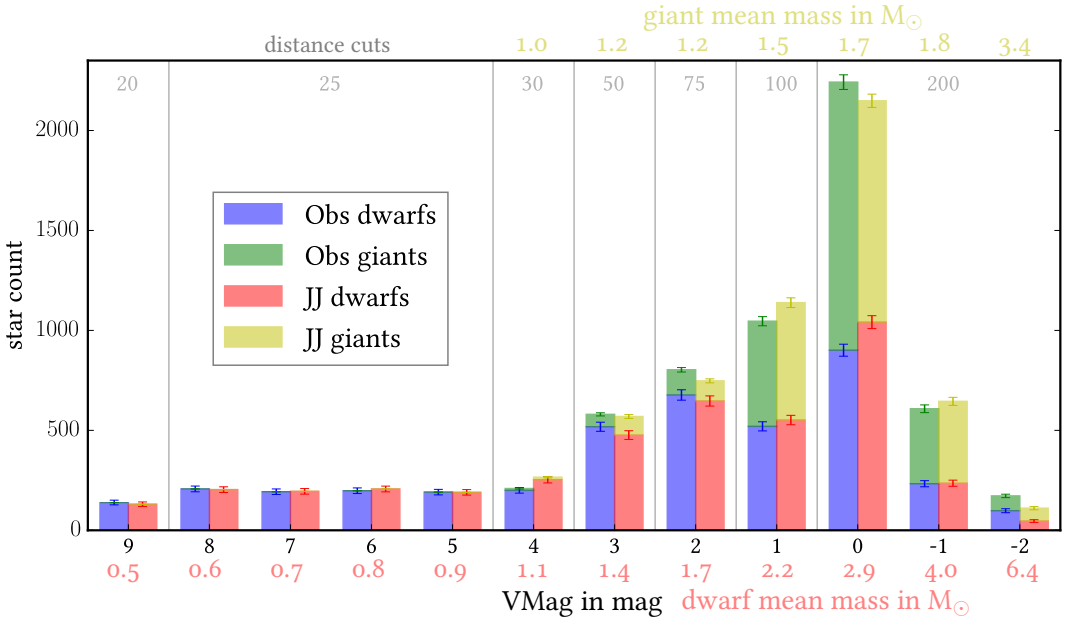

Figure 3.4: Luminosity function of the observations and the new IMF of the JJ-model (cf. table 1 and 2). Error bars indicate Poisson noise in the observational sample and the standard deviation for the 400 times over-sampled synthesised catalogue. Star counts are not normalised for the different distance limits. The limiting radii of the corresponding magnitude bins are written in the top.

deviation of the number density of each marginalised parameter is given which represents our central result and defines our new fiducial IMF:

$$\begin{aligned} \alpha_1 &= 1.49 \pm 0.08, \\ \alpha_2 &= 3.02 \pm 0.06, \\ m_1 &= 1.39 \pm 0.05, \\ mf &= 1.09 \pm 0.04. \end{aligned} \tag{42}$$

Furthermore Pearson's correlation coefficient for each parameter pair is given in the upper right of figure 3.3 which is also represented in the 1σ-3σ ellipses of the projected point clouds. The only two parameter which are uncorrelated are the power-law indices. Almost positive linear is the correlation of the mass factor with the low-mass slope. This is due to more mass being put into stars which are not represented in our data ($m < 0.5\,M_\odot$) for high α_1 which can be counterbalanced with a high-mass factor. Similarly but less strong the anti-correlation of the mass factor with the high-mass slope is due to mass being shifted out of our represented data domain when α_2 is getting lower. The reason for both power-law indices being positively correlated with the power-law break is due to the shape of the IMF which is sharply decreasing at the position of the break and the number densities of the faintest and brightest magnitude bin which need to be matched when shifting m_1. This reasoning can be best visualised when looking at the green dotted line (our IMF) and the blue error bars (our observational sample) in figure 3.5. Additionally when increasing both α_1 and α_2 the mass that is gained by the steeper low-mass slope will be counterbalanced by the mass-loss of the steeper high-mass slope.

Figure 3.4 shows the binned LF of our fiducial IMF (averaged over 400 realisations) compared to the observations in absolute numbers. The CMD representation of the LFs can be seen in figure 3.2 where the same colours have been used for the different samples. The deviations in each bin look small and systematics are not apparent neither in the dwarf nor the giant sample which shows that the whole machinery, consisting of the disc model and Galaxia producing the mock observations, works well and the MCMC simulation has likely converged towards the equilibrium configuration.
When inspecting the detailed likelihood contribution of each bin in table 1 & 2 we see that the largest penalty comes from the zeroth VMag bin. Especially the giants with $\ln(\mathcal{L}/P_{max})$ = -23.4 have a huge impact. The reason for that is likely a RC that is too faint in our mock catalogue. In the dwarf sample too many stars are in the synthesised zeroth VMag bin with $JJ_{25} \cdot (N_{fin}/N_{25})$ = 1036 compared to 901 stars in the Hipparcos catalogue.
A weakness of our modelling machinery is apparent in the high $\ln(\mathcal{L}/P_{max})$ value of the brightest dwarf bin indicating that too few bright stars are produced. The reason is most likely that we are not accounting for binaries and that we use a two-slope power-law. Minor effects could be missing high-metallicity stars and that our synthesised stars are not younger than 6.25 Myr. It could also indicate a change of the high-mass power-law index for stars more massive than contained in our data.

3.5.2 TESTED IMFS

Because for other shapes of the IMF part of the mass could also be hidden in the mass range not represented by our observational sample (0.5 to 8 $M_\odot$) we determine the factor with which the total mass needs to be rescaled in order to maximise the likelihood for a particular IMF when it is used with our JJ-model against the observational sample. We again average over 400 realisations and get the standard deviation as the enclosing 68 % of the likelihood. In table 4 the log-likelihoods of the different IMFs (using our disc model but adjusting for each IMF's best fit mass factor) are listed with $JJ_{3\sigma}$ being the log-likelihood value which is lower than 99.7 % of the points representing the PDF in figure 3.3.
Table 5 illustrates a few properties of our log-likelihood. JJ_{400} and JJ_1 show the mean and the standard deviation of 100 log-likelihood determinations with different seeds which are averaged over 400 in the former and 1 realisation in the latter case. This shows that the averaging is important for the MCMC simulation in order to smoothen the likelihood distribution. The deteriorated mean for single realisations is due to a skewed distribution since P_{max} is a lower limit and the penalty increases for extreme values which are not smoothed out as in JJ_{400}.

The last column of table 5 (JJ_{ideal}) gives an ideal log-likelihood which is obtained when the data is indeed represented by the model. For that we draw 100 single random samples (JJ_1) from JJ_{400} with replacement and evaluate their log-likelihood with the parent distribution (JJ_{400}). Each sample fulfilling the observational constraint of having dwarf and giant star counts fixed to $N_{Obs,dwarf}$ = 4075 and $N_{Obs,giant}$ = 2513. This means that a $\ln(\mathcal{L}/P_{max})$ of around -13.8 would indicate a perfect model. An even lower log-likelihood value close to P_{max} ($\ln(\mathcal{L}/P_{max}) = 0$) would be unrealistic since there is a natural scatter to Poisson processes.
Related to that we also inspected the distribution of star counts in individual magnitude

Table 4: Likelihoods of the different IMFs

IMF	JJ	$JJ_{3\sigma}$	Besançon B	KTG 93	Chabrier 03
$\ln\left(\frac{\mathcal{L}}{P_{max}}\right)$	-79.3	-86.7	-96.7	-195.6	-216.1

Table 5: Variability of the log-likelihood

Sample	JJ_{400}	JJ_1	$JJ_{ideal^\star}$
$\ln\left(\frac{\mathcal{L}}{P_{max}}\right)$	-79.3 ± 0.6	-89.5 ± 14	-13.8 ± 2.8

*if data was coming from our model (see text)

bins for random realisations (with the same parameters but different seeds) which indeed is Poissonian.

KTG 93

The widely used Kroupa et al. [1993] (KTG 93) IMF is a three-slope broken power-law with $\alpha_1 = 1.3$, $\alpha_2 = 2.2$, $\alpha_3 = 2.7$, $m_1 = 0.5$ and $m_2 = 1$.

$$\frac{dn}{dm} = k_\alpha m^{-\alpha} \begin{cases} \alpha = \alpha_1, & m_{low} < m < m_1 \\ \alpha = \alpha_2, & \text{if } m_1 < m < m_2 \\ \alpha = \alpha_3, & m_2 < m < m_{up} \end{cases} \tag{43}$$

Again the k_{α_i} ensure continuity and normalisation of the IMF to unity in mass between $m_{low} = 0.08\,M_\odot$ and $m_{up} = 100\,M_\odot$.
The likelihood peak is obtained with a mass factor of 1.392 ± 0.019 which is quite high. The reason for that is too much mass being put into low-mass stars which are not represented in our observational sample (see table 8).
With $\ln(\mathcal{L}/P_{max}) = -195.6$ it scores poorly compared to our or the default model B of Czekaj et al. [2014] (Besançon B) IMF showing that its shape is not able to reproduce local star counts. This is visible in figure 3.5 where it produces too few stars within 0.9 - 2 $M_\odot$ and too many outside of this range compared to our IMF.

Besançon B

This is one of the new fiducial Besançon model IMFs from Czekaj et al. [2014] tested with Tycho 2 all-sky colour distribution. It is also a three-slope broken power-law with $\alpha_1 = 1.3$, $\alpha_2 = 1.8$, $\alpha_3 = 3.2$, $m_1 = 0.5$ and $m_2 = 1.53$. The mass factor for this IMF is 1.107 ± 0.015 which is compatible with our own mf. Also the shape of the IMF (cf. figure 3.5), the likelihood (see table 4) and the mass fractions (cf. table 8) are similar. This is remarkable since they have different scale heights, SFH and also an additional data set (Tycho 2 colour vs. Hipparcos/CNS VMag).
Compared to our IMF the Besançon B IMF is producing slightly less high-mass stars and more low-mass stars which could be partly due to their rigorous treatment of binaries (see figure 3.5 and cf. section 3.6.3).

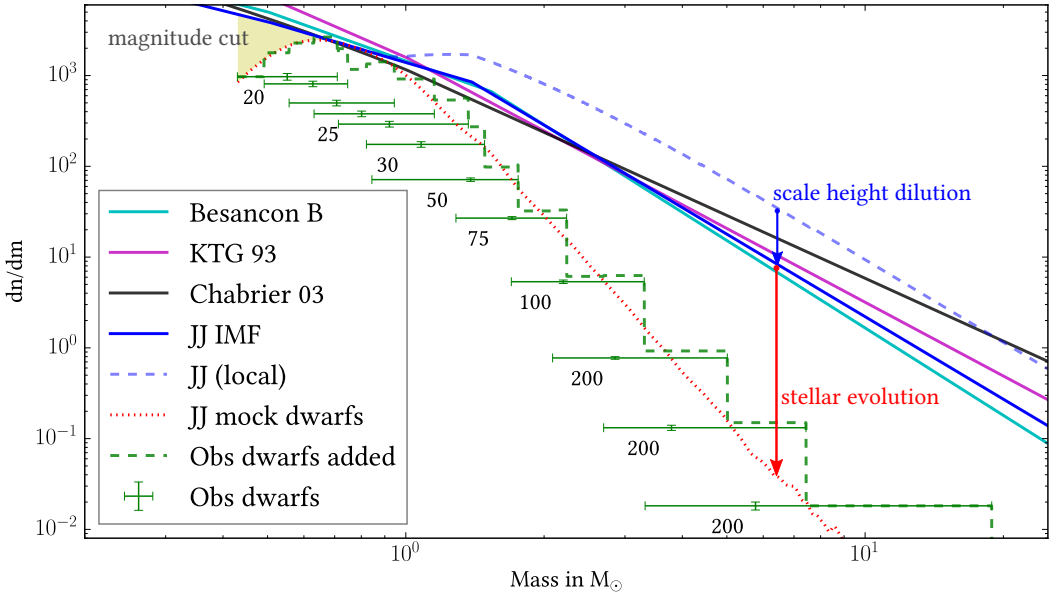

Figure 3.5: 25 pc LF of dwarf stars translated into mass space. Our fiducial IMF is plotted in thick blue and the Besançon B, KTG 93, and Chabrier 03 IMFs are plotted in cyan, magenta, and black, respectively. The green error bars represent the 12 magnitude bins from the observational dwarf sample with their limiting radius given in parsec. The x-value and the x-error are associated with the median and the range of stellar masses in the corresponding mock magnitude bin synthesised with our fiducial IMF. The y-value represents the number of stars normalised to the mass range and the y-error is the Poisson noise. As the masses from different magnitude bins overlap the values are added up in the dashed green line representing a kind of 'observational' PDMF. Below 0.7 $M_\odot$ the yellow shaded area indicates the mass that is missing due to incompleteness by the magnitude cut. In dotted red the same effect is visible, as this line represents the synthesised dwarf mass function of our IMF averaged over 100 realisations. From 0.9 $M_\odot$ upwards the IMF and the local IMF in dashed blue deviate since locally (i.e. close to the Galactic plane) young and therefore massive stars are over-represented, which is indicated by the blue arrow. The change from the IMF to the PDMF due to stellar evolution is indicated by the red arrow.

Chabrier 03

Another widely used IMF comes from Chabrier [2003]. It is a mixture of a lognormal form in the low-mass and a Salpeter power-law in the high-mass regime

$$\frac{\mathrm{d}n}{\mathrm{d}m} = \begin{cases} \frac{0.852464}{m} \exp\left(\frac{-\log^2\left(\frac{m}{0.079}\right)}{2 \cdot 0.69^2}\right), & \text{if} \quad m < \mathrm{M}_\odot \\ 0.237912 \cdot m^{-2.3}, & \qquad\quad m > \mathrm{M}_\odot. \end{cases} \tag{44}$$

The mass factor for the best likelihood is: 1.317 ± 0.017. It is so high because a huge mass fraction is going into stars more massive than 8 $M_\odot$ (cf. table 8, highest supernova rate compared to any other standard IMF). The shape of the Chabrier 03 IMF fits our model worst with respect to the data scoring a log-likelihood of $\ln\left(\mathcal{L}/\mathrm{P}_{\max}\right)$ = -216.1.

3.5.3 From Luminosity Function to local stellar mass density

In figure 3.5 the IMFs are normalised such that their integrated mass is representing the mass of gas that was turned into stars (of which a few already turned into remnants) still

residing in the 25 pc sphere (i.e. $\mathcal{M}_{\mathrm{IMF,25\,pc}}$ including the thick disc and each IMF's mass factor cf. equation 33). Beware that in figure 3.5 actually the number of stars per mass interval is displayed though normalisation happens in mass space (see discussion in section 3.6.2).

The yellow shaded area shows the incompleteness of our observations in low-mass stars due to the magnitude cut. This comes from high-metallicity stars being redder and fainter than their equal-mass low-metallicity counterparts so they are excluded and do not contribute to the smallest mass bin leading to a decrease of the observed mass compared to the theoretical IMF. The same is true for the JJ-model mock dwarfs in dotted red (as we apply the same magnitude cuts) which were spawned using the blue IMF. We could drop the magnitude cut for faint stars in Galaxia and the red dotted line would be perfectly aligned with the JJ-model IMF in the low-mass regime, which corresponds to the local PDMF. In the 'observational' PDMF represented by the dashed green line the little bump compared to the JJ-model mock dwarfs at around 0.8 $\mathrm{M}_{\odot}$ coincides with the *Wielen dip* [Wielen, 1974], observed in the local luminosity function at VMag ~ 7.
In the high-mass regime, the blue arrow indicates the over-representation of massive stars in the local IMF of the 25 pc sphere, as their vertical distribution is more confined to the Galactic plane (if one would not account for the scale height dilution the deduced IMF would look like this). The red arrow indicates the conversion from the IMF to the PDMF due to stellar evolution.
We can quantify the difference of IMF and PDMF by looking at the integrated mass (between $\mathrm{m_{low}}$ and $\mathrm{m_{up}}$) of the two functions represented by 'JJ IMF' and 'JJ mock dwarfs' from figure 3.5 (the latter being made equal to 'JJ IMF' for the low-mass part not affected by stellar evolution). The outcome is that 55.8 % of the mass originally turned into stars is still present in dwarf stars today ($\mathcal{M}_{\mathrm{PDMF,25\,pc}}$ / $\mathcal{M}_{\mathrm{IMF,25\,pc}}$). Including giants this value only changes slightly to 56.9 % which is consistent with the integrated stellar mass of our disc model (figure 1 of paper I adapted for 25 pc age distribution yields 56.5 % of stars increasing to 70.8 % when remnants are included which is their $\mathrm{g_{eff}}$) confirming that the new IMF still fits within our model's framework as SFH and AVR are only dependent on the integrated mass-loss.

In order to clarify our remnants which Galaxia is not synthesising we derive from our PDMF and IMF that we should have 707 stellar remnants for stars between 1 and 8 $\mathrm{M}_{\odot}$ (potentially WDs) and 17 heavier ones (potentially black holes or neutron stars) in the 25 pc sphere. Compared to Sion et al. [2014] (or similarly Just et al. [2015]), we have over a factor of 2 more since they expect 344 WDs within the same limits. But their assumed volume-completeness for the 13 pc sample is probably more like a lower limit, at least when speaking of the cool end of the WD cooling sequence. Holberg et al. [2008] propose a WD mean mass of 0.665 $\mathrm{M}_{\odot}$ which for us results in a WD mass density of 0.0072 $\mathrm{M}_{\odot}/\mathrm{pc}^3$ quite close to the Besançon value based on Wielen [1974] which was already corrected downwards in Jahreiss and Wielen [1997] because one out of 5 WDs left the 5 pc sphere. Our high number of WDs is partly due to the functional form of the two-slope IMF because it has an overabundance where the power-law break lies (when expecting a concave function describing the underlying distribution in log-space, see our IMF in figure 3.5) which slightly exaggerates the mass fraction of the IMF going into Planetary Nebula (PN) (cf. table 8).

Table 6: Local stellar mass density of different thin disc components in $10^{-4} M_\odot / pc^3$

Mass component	Flynn et al. [2006]	JJ-model	JJ-model*
giants	6	7	7
$M_V < 2.5$	31	11	11
$2.5 < M_V < 3$	15	5	5
$3 < M_V < 4$	20	19	19
$4 < M_V < 5$	22	26	25
$5 < M_V < 8$	70	66	65
$8 < M_V$	135	205	176*
$\rho_{\text{thin disc}}(z = 0\,pc, t = 12\,Gyr)$	299	338	309
$\rho_{\text{thick disc}}(z = 0\,pc, t = 12\,Gyr)$	35	17	15
brown dwarfs	20	20⋆	20⋆
white dwarfs	60	72†	30*
$\rho_{\text{PDMF, total}}$	414	447	374

*using Just et al. [2015] (empirical extension from section 3.6.8)
⋆taking the same value as Flynn et al. [2006] (FH 06)
†derived implicitly from our PDMF (see text)

With these values (summarised in table 6) the overall present-day mass fraction of stars and stellar remnants ($\mathcal{M}_{\text{PDMF,total, 25 pc}}$) is

$$g_{\text{eff}} = \frac{\mathcal{M}_{\text{PDMF, 25 pc}} + \mathcal{M}_{\text{BD \&WD 25 pc}}}{\mathcal{M}_{\text{IMF,25 pc}}} = 71.7\,\% \tag{45}$$

which is close to 70.8 % for the 25 pc sample of paper I. This also implies a combined Brown Dwarf (BD) and WD mass fraction of about 20 % of the local mass budget ($\mathcal{M}_{\text{PDMF,total, 25 pc}}$) consistent with the Jahreiss and Wielen [1997, tab. 3] value and the stellar evolution of paper I. Then again we also could have chosen the proposed WD local mass density of Holberg et al. [2008] $M_\odot / pc^3 = 0.0032$ which would decrease the local disc mass density and change g_{eff} and the remnant fraction. Here we chose to stay self-consistent with our IMF's remnant fraction though we could have used those independent observations as a prior yielding tighter constraints for our IMF.

For the following local mass density test we use our disc model and the fiducial IMF to produce all stars within 25 pc down to 0.08 $M_\odot$ without any magnitude cuts and analyse the sample's properties. In this sample we find a local stellar mass density of 0.034 $M_\odot / pc^3$ compared to 0.030 $M_\odot / pc^3$ for the same selection of stars in Flynn et al. [2006, tab. 2] (including giants, excluding BDs, WDs, other remnants and the thick disc component) who use a similar method. In table 6 the detailed comparison reveals that especially the two brightest bins of the FH 06 sample are 3 times denser than the corresponding bins in the JJ-model sample. For VMag$>$ 3 the densities match quite well except for the faintest mag bin. The over-abundance of bright stars could be caused by their large value of n in Holmberg et al. [1997, eq. 3], which is resulting in nearly exponential vertical density distribution with high local mass densities though this then should apply to the other mag bins as well.

Table 7: Local mass density over stellar age in $10^{-4} M_\odot / pc^3$

Age [Gyr]	Besançon A	Besançon B	JJ-model	JJ-model*
0 - 0.15	20	19	9	8
0.15 - 1	55	50	36	34
1 - 2	46	41	30	29
2 - 3	33	28	27	25
3 - 5	58	49	52	48
5 - 7	61	50	54	49
7 - 10	117	93	84	76
10 - 12	-	-	46	41
Thin disc	390	330	338	309
Thick disc	29	29	17	15
WD	71	71	92†	50†*
$\sum$	490	430	447	416

*using Just et al. [2015] (empirical extension from section 3.6.8)
† including BDs

Another indication for an over-estimation of their model's local star counts becomes evident when comparing the number densities from Holmberg and Flynn [2000] (upon which FH 06 is based) with those from CNS5. For $M_V < 2.5$ they have 0.0013 star pc^{-3} whereas our volume-complete sample has half of this with 0.0007 star pc^{-3} and this despite the fact that the 25 pc from the CNS5 seem to have an over-representation of the upper MS compared to the larger sample (cf. table 1). The next mag bin $2.5 < M_V < 3$ is three times denser according to Holmberg and Flynn [2000] with 0.0010 star pc^{-3} compared to the 0.0003 star pc^{-3} we measure for our 25 pc sample, which strongly indicates a necessary revision. Fainter mag bins are much better fit in star counts as well as in stellar mass density.
Comparing our thin disc stellar mass density (excluding thick disc stars and WDs) of 0.0338 $M_\odot / pc^3$ to the default Besançon B model that has 0.0330 $M_\odot / pc^3$, reveals a similar discrepancy. Our disc model has 12 Gyr of evolution compared to 10 Gyr, and in table 7 we make a detailed comparison, keeping in mind the different SFH and vertical profiles of each disc model [Czekaj et al., 2014, tab. 7 and fig. 4]. The Besançon B model uses the same local mass density as we do from Jahreiss and Wielen [1997] based on 25 pc, though they add the thick disc on top of this value, which is an inconsistency, as Jahreiss and Wielen [1997, table 3] accounts for all local stars, not only those of the thin disc.

Overall, for the other disc mass models more mass seems to be sitting in stellar mass bins of bright stars, which might be partly due to the local dwarf sample being almost 2 times denser than the 200 and 100 pc sample at the upper MS (cf. table 1 'Observations' & 'CNS5'). Since we use volume-complete samples to fit the luminosity function and take into account the scale height dilution according to the stellar ages, we trust our mass distribution in the mass range that our observational evidence samples (0.5 - 8 $M_\odot$).
From the local LF the high-mass end of the IMF for stars more massive than 8 $M_\odot$ can not be

constraint, due to too few massive stars. The impact on the stellar mass density is negligible. In chapter 4 we will constrain the high-mass slope, using abundance data and a chemical extension of the JJ-model.
Ideally we should have included a constraint for the low-mass stellar mass density from other observations (which we do empirically in section 3.6.8) because now the mass factor and the low-mass power-law index are strongly correlated and certainly a bit too high. Better values for a more realistic two-slope IMF would probably be in the lower left of the 1σ ellipse in figure 3.3 (e.g. $\mathrm{mf} \simeq 1.05$ and $\alpha_1 \simeq 1.4$).

3.6 DISCUSSION

We discuss our findings with respect to their model dependencies as well as our analysis method. Then we provide a comparison of the mass distribution from various IMFs and end this section with an empirically driven adaptation of our IMF to account for missing low-mass star representation in our data.

3.6.1 ISOCHRONES

A crucial ingredient for our investigation is the used set of isochrones since it translates our analytical disc model into the realm of observables. When we were using the default option [Marigo et al., 2008] provided by Galaxia, the highest likelihood we could score was $\ln(\mathcal{L}/\mathrm{P}_{\max})$ = -109 with slightly different IMF parameters. With the latest PARSEC [Bressan et al., 2012] isochrones the observations are much better fit by the model increasing the normed log-likelihood by 30. Still a few discrepancies are visible when inspecting figure 3.2.
The M dwarf V-Band problem was already mentioned in section 3.2.2 and is discussed in Chen et al. [2014].
Section 3.5.1 discusses the huge likelihood penalty from the brightest magnitude bin in table 1 which could be due to unaccounted binaries in our sample or due to missing turn-off stars (which could be related to our discrete time steps) or due to missing super Solar metallicity stars or a high-mass power-law index which is too large which is due to the functional form of our two-slope IMF.
Table 2 shows missing stars in the zeroth mag bin and an over-abundance in the first for the giants. This is an indication for the RC being too faint compared to the observations.
Another striking feature is the complete absence of synthesised stars bluewards from the RC whereas Hipparcos shows several dozens. One reason is probably that population II stars are not synthesised, such that the horizontal branch is not reproduced by our model. Also the extrapolated high-mass slope produces too few massive stars, which would populate this region of the CMD.
Of course not all differences are linked to the isochrones as the JJ-model SFH, AMR or IMF also affect the distribution of stars in the CMD. Another reason for mismatch is our used reddening law not accounting for inhomogeneous ISM which explains the unmatched faint giants on the red end of the giant sequence in figure 3.2.

3.6.2 MASS FACTOR

The overall mass with our newly determined IMF compared to the JJ-model SFH increased by the thick disc fraction (6.5 %) and the mass factor (mf = 1.09). The normalisation in paper I was done using $\rho_{\mathrm{PDMF,total}} = 0.039\,\mathrm{M_\odot pc^{-3}}$ from Jahreiss and Wielen [1997]. Since we utilise new isochrones together with number densities derived from volume-complete star counts, a change of about 10 % is not unexpected but our value of $0.045\,\mathrm{M_\odot pc^{-3}}$ is probably exaggerated. The present-day mass fraction (g_{eff}) stays similar and also the remnant fraction is compatible with paper I values as shown in section 3.5.3, though WD and faint stellar local mass density are arguably too high. The problem is that we do not have observational constraints for the whole mass range resulting in a degeneracy of the mass factor and the low-mass slope (see figure 3.3, also valid for the high-mass slope). We propose a solution to this in section 3.6.8.

3.6.3 BINARITY

In our observational sample we tried to account for all binaries that have Δmag entries, so that we could split them up. Apart from these another 365 stellar entries in our observational sample are listed in the *Washington Double Star Catalogue* [Mason et al., 2001] or the *Catalogue of Components of Double and Multiple Stars* [Dommanget and Nys, 2002], as multiple systems but are not resolved, i.e. they are not split up for this analysis but just kept as one 'star'.
As mentioned in section 3.5.1, we have a problem with binaries in massive stars, which are hard to detect, as lines are blurred, and increased luminosity could also be due to ageing of a single star. Since binary fraction in massive stars is expected to be up to 80 % and our likelihood gets a large penalty from the brightest dwarf mag bin not being matched well (other important reasons for too few synthesised stars in that bin are our two-slope functional form and our rough analytic extinction model), we believe that we miss quite a few high-mass binaries. Other than that, listings of binary stars in the Hipparcos catalogue are said to be 'fairly complete' [Lindegren et al., 1997] for $\Delta Hp < 3.5$ mag and an angular separation bigger than 0.12 to 0.3 arcsec (increasing with ΔHp). In CNS5 all stellar systems from the literature with resolved magnitude differences are split into their respective components.

The Besançon group is doing the favourable approach of accounting for binaries from the model's side [Czekaj et al., 2014; Robin et al., 2012; Arenou, 2011]. They use an angular resolution limit of 0.8 arcsec for resolved binaries in their Tycho 2 data. In Czekaj et al. [2014, fig. A.3] the relative difference in stellar mass frequency produced with binarity treatment in single, primary and secondary stars compared to the same sample excluding secondary stars is shown. With B-components included the IMF produces around 6 % more stars below 1.1 $\mathrm{M_\odot}$ and around 6 % less above with a short transition in between. Overall the effect of binarity seems to play a secondary but not negligible role especially in massive dwarf stars.

3.6.4 DIFFERENT FUNCTIONAL FORMS OF THE IMF

A crude investigation of the three-slope IMF after the publication of Rybizki and Just [2015] yielded an improved $\ln\left(\frac{\mathcal{L}}{P_{max}}\right)$ = -46.2 compared to -79.3 for the best two-slope IMF, but with two more free parameters: α_1 = 1.51, α_2 = 3.47, α_3 = 1.47, m_1 = 1.55, m_2 = 3.60 and mf = 2.1.
This IMF would need further observational constraints from stars lighter than 0.5 $M_\odot$ (and heavier than 8 $M_\odot$) which are not (well) represented in our data. For the two-slope IMF this is done in section 3.6.8 by introducing another low-mass break in the power-law. Obtaining a constraint for the high-mass stars is challenging (see section **??**) but would certainly yield a steeper high-mass slope compared to α_3 = 1.47.
The assessment whether we are over-fitting or adding significant parameters would need the comparison of Bayes Factor (BF)s (see section 2.1.5) for each functional form (and replaces the *reduced* χ^2 methodology). In that case we should not only test the parameter space of multicomponent power-law functions, but also of other functional forms (e.g. Chabrier [2003], Parravano et al. [2011]). In our analysis we only used the fixed literature values and adjusted for the mass factor which just shows that these IMFs yield lower likelihoods (within our model and likelihood determination) than our optimised two-slope power-law.

3.6.5 SPLITTING THE CMD

Before exploiting the full 2D information of the CMD and adapting the statistical machinery as well as dealing with colour issues of the isochrones (not speaking of enhanced sensitivity to reddening), the easiest way to increase the data constraints is to split up the CMD into dwarf and giant samples as we do here. Weighting both into the final likelihood is a valuable gain since they represent stellar populations with different ages and masses (check the last columns of table 1 & 2), and are still build from the same IMF (as well as SFH, AVR and AMR). Interestingly the likelihood penalties from both samples are similar though the dwarfs contribute 12 and the giants only 7 bins. In fact, the faint mag bins from the CNS are well matched with a one-slope IMF in the low-mass range (0.4 < $M_\odot$ < 1.0). This mass range is only represented in the dwarf stars, so no trade-off with the giants is necessary leading to a small cumulative penalty of $\ln(\mathcal{L}/P_{max})$ = -0.45 from these 5 bins.

Exemplary for the insight gained from splitting up the CMD, the zeroth mag bin can be inspected where a common sample would have balanced our model predicting too few giants and too many dwarfs. As these two bins have well distinct age and mass, constraints are put on different parts of the IMF. On the other hand the over-abundance of stars in the third mag bin in giants and the 4th mag bin in both giants and dwarfs is indicating too many stars for the IMF around 1.1 $M_\odot$. This is in balance with the depletion of stars from around 1.3 $M_\odot$ (second mag in giants and third in dwarfs) in order to fit the two-slope power-law with respect to our constructed likelihood.

3.6.6 BINNING

As pointed out in section 3.4.1 (and also in a blog entry[3] written on our statistical method) the importance of likelihood is unevenly assigned between different bins. On the one hand, this is wanted, because higher star counts in a bin give a stronger constraint for the assumed Poisson process, on the other hand this is problematic when small systematic errors, translate into larger penalties for densely populated mag bins. Similarly for the MCMC when it is trading-off log-likelihood penalties to *find* its equilibrium position. With this in mind the relatively high $\ln(\mathcal{L}/P_{max})$ values of the third mag giant bin, the 4th mag and the brightest dwarf bin, (though having comparatively low star counts) indicate an even stronger deviation from the data than represented in the log-likelihood penalty. The deviations are not compatible with expected Poisson noise, as the third mag giant bin and the 4th mag dwarf bin are close to $4\,\sigma$ off their expected value and the brightest dwarf bin is off by more than $5\,\sigma$.

This means that our IMF produces too many stars around $1.1\,M_{\odot}$ and too few high-mass stars, which shows that our adopted functional form of a two-slope IMF is probably too inflexible to match the underlying IMF represented by the data. A test for the BF of different functional forms together with additional low- and high-mass constraints (priors) could clarify this hypothesis (cf. discussion in sec 3.6.4).

The best solution would be, to avoid binning in the first place what we did not do because we wanted a high quality observational sample with little model-dependency leading to the choice of volume-complete samples and their conservative magnitude cuts (a more robust way of constructing volume-complete samples is discussed in section 2.2). On the other hand modelling the complete magnitude-limited Hipparcos catalogue would have made more use of available data. The complication would have been, to simulate the smooth density distribution of our JJ-model in Galaxia and account for increasing contribution of thick disc stars with increasing height above Galactic plane. The integration of a semi-analytic form of our JJ-model in a future version of Galaxia could make this endeavour feasible and also simplify the integration of a 3D extinction model.

3.6.7 HIGH-MASS SLOPE

Our high-mass power-law index of $\alpha_2 = 3.02$ is at the higher end of the literature values which can mostly be attributed to the functional form and should also not be extrapolated to O and early B type stars, because these are not very well sampled in our 200 pc volume. For studies using star counts, it will always be challenging to account for high-mass stars, because of them being rare and confined to the Galactic plane, where extinction complicates things. This (and a similar functional form) is the reason why we and also the new default Besançon model [Czekaj et al., 2014] propose steep high-mass slopes for A and late B type stars. Only with Gaia [Lindegren et al., 2008] (Gaia) the surface density of O,B stars will be available for a large area, yielding viable constraints on the high-mass slope of the IMF from the LF.

3 https://astrostatistics.wordpress.com/2015/01/15/some-unwitting-pdbil-mcmc/

Table 8: Mass distribution, PN- and SN II-occurrences for different IMFs

IMF:	JJ-model	JJ-model*	Besançon B	KTG 93	Chabrier 03	Salpeter 55
Mass range in $M_\odot$	mass fraction in %					
8 - 100	6	7	4	8	22	15
1.4 - 8	32	34	30	24	29	20
1 - 1.4	13	13	12	9	7	5
0.5 - 1	20	21	23	22	16	12
0.08 - 0.5	29	25	31	36	26	48
PN* (1 - 8)	994	1044	951	707	687	467
SN II* (> 8)	17	18	12	21	47	32

*number of occurrences for an SSP with mass $M_{IMF,25\,pc} \approx 4100\,M_\odot$ at $t = \infty$
*using Just et al. [2015] (empirical extension from section 3.6.8)

An important measure for an IMF in terms of Galaxy simulation is the fractional mass going into stars heavier than $8\,M_\odot$ as they supposedly explode as SuperNova of type II (SN II) and have the highest and fastest stellar feedback to the Galactic evolution in terms of gross elemental synthesis and heating of the gas phase. In table 8 we list the fraction of total mass and total star count going into the SN II mass bin for all investigated IMFs adding Salpeter (with $\alpha = 2.3$) for comparison.
The fraction of mass going into stars ending their lives as SN II ranges from 4 % for Besançon B to 22 % for Chabrier 03. In order to obtain sensible results, modellers usually tune their feedback physics according to their used IMF. In general CEMs and their predicted element ratios are especially sensitive to the number of SN II events. So using a Chabrier 03 IMF will need substantially different stellar yields to obtain similar results (i.e. reproduce observations) compared to a CEM using the new Besançon B IMF (see chapter 4).
Same is true for cosmological hydrodynamical simulations reproducing the number of dwarf galaxies around spirals and also galaxy morphologies. Usually the necessary feedback is high, so that top-heavy mass functions are used like the Chabrier 03 IMF. To get even higher feedback the limiting mass for SN II-explosion can be reduced below the fiducial value of $8\,M_\odot$ as for example in Vogelsberger et al. [2013, with a limiting mass of $6\,M_\odot$]. Depending on the sub-grid physics of wind mass loading and wind metal loading which they treat separately the observed stellar masses of galaxies and especially low-mass systems are reproduced (this is achieved with large wind mass loading and generally a huge amount of SN II). But at the same time this over-predicts the metallicity of massive galaxies and underestimates the metallicity of dwarf galaxies [Vogelsberger et al., 2013, fig. 11 & sec. 4.2.7], which can not be counterbalanced by the wind metal loading factor. This tension not only suggests that too much stellar mass is going supernova but might as well point to a metallicity - or more general: an environment-dependent IMF [van Dokkum and Conroy, 2012].

3.6.8 EMPIRICALLY MOTIVATED THREE-SLOPE IMF EXTENSION

Our observational sample not constraining the high (volume too small) and low-mass stars (sparse V Band data and no reliable isochrones) is deteriorating our inferred IMF parameters. A good solution would be to include observationally based priors into the likelihood determination directing the MCMC simulation to a more physically motivated solution. Possible constraints directly connected to the shape of the IMF and the mass normalisation could be the SN II rate and H II regions the PN rate the WD number density and low-mass stellar density. But it is not trivial to account for the uncertainty of those observations in the prior function.
As an empirical fix we introduce a second power-law break at $0.5\,M_\odot$ leaving the shape of the IMF above the same, but changing it for lower masses. With a look at table 6 all bins should stay the same except for the $8 < M_V$ bin which should decrease to $0.017\,M_\odot pc^{-3}$ being a new value derived from volume-complete near-infrared (IR) data of the CNS5 [Just et al., 2015]. This shrinks our mass factor and still uses our high quality data for the higher mass bins. The proposed IMF parameters fulfilling this additional constraint are: $\alpha_0 = 1.26$, $m_0 = 0.5$, and $mf = 1.03$. Compared to our low-mass slope of $\alpha_1 = 1.49$ the extension to lower masses is a bit shallower and quite similar to KTG 93 also having its low-mass power-law break at $0.5\,M_\odot$.

3.7 CONCLUSION

We use Solar Neighbourhood stars to determine a new fiducial IMF, in the mass range $0.5 - 8\,M_\odot$, within the framework of our local vertical MW disc model (JJ-model). For that we carefully select volume-complete samples based on dereddened and binary corrected Hipparcos and CNS5 data. Then we use Galaxia to create the corresponding mock observations from our JJ-model. We construct a likelihood by assuming a discrete Poisson process for the star count in magnitude bins differentiating between dwarfs and giants. With MCMC simulations we sample the PDF of the two-slope IMF parameters. The derived IMF has a low-mass power-law index of $\alpha_1 = 1.49 \pm 0.08$, a power-law break at $m_1 = 1.39 \pm 0.05\,M_\odot$, a high-mass index of $\alpha_2 = 3.02 \pm 0.06$, a mass factor of $mf = 1.09 \pm 0.04$ with respect to our paper I mass normalisation. Except for physics not accurately represented in our model (binaries, inhomogeneous ISM, variable stars, low-mass stellar atmospheres, metal enrichment law and thick disc) these findings are robust in our observationally backed mass range from 0.5 to $8\,M_\odot$. An empirically driven low-mass extension adds $\alpha_0 = 1.26$ and $m_0 = 0.5$ and decreases the mass factor to 1.03.
Independently from us, the Besançon model using Tycho 2 colour projections as observational constraints favours similar IMFs. The steep high-mass slopes decrease the number of SN II ejected by an SSP compared to classical IMFs like Salpeter or Chabrier 03 by a factor of about 3.
The future of analytic Galaxy modelling will see increasing modularity to incorporate up-to-date theoretical progress in stellar atmospheres and evolutionary tracks. Observational biases like binarity, selection effects or reddening will be accounted for from the models side and the observational samples will get diversified to overcome degeneracies in the various model ingredients like SFH, AVR and CEM. With ever more realistic MW models traces of theoretical concepts like the Cold Dark Matter (CDM) halo or chemical yields can be

mapped into the space of observables putting tighter constraints on the model ingredients. To achieve that, tools to measure the probability of model predictions given the data and schemes to optimise for the various data sets in an automated hierarchical fashion need to be implemented. On the other hand high-quality data, able to discriminate between different model parameters, is needed. With the second data-release of Gaia, precise parallaxes of up to a billion stars will be published so that an exciting era for Galaxy modelling is lying ahead.

4

CHEMICAL ENRICHMENT MODEL PARAMETER ESTIMATION WITH APOGEE DATA

In section 4.2 Chempy, a new numerical chemical evolution model, will be presented. In a proof-of-concept, important parameters of the chemical model will be determined, as inferred from Solar Neighbourhood abundances of Red-Clump (RC) stars. The statistical techniques to map the model into the space of observables and to construct a suitable statistical measure, for comparing the mock data to the real data, are discussed in sections 4.3 & 4.4. With an Markov Chain Monte Carlo (MCMC) the posterior of the parameter space will be explored and the resulting new fiducial values are presented in section 4.5. Different yield sets are tested in section 4.5.1 and the results indicate that the chemical model can put constraints on the high-mass index of the Initial Mass Function (IMF).
The chapter is beginning by a short introduction to the concept of analytical chemical enrichment models following the derivation of [Matteucci, 2012, chapter 3].

4.1 THE SIMPLE ONE ZONE CLOSED BOX MODEL

For the simple model, the following assumptions are made:

- the system consists of one zone and is closed
- the initial gas is primordial
- the IMF $\phi(m)$ is constant in time
- the gas is well mixed at any time

First, the fractional gas mass is defined,

$$\mu = \frac{M_{gas}}{M_{tot}}, \tag{46}$$

which relates the gas mass to the total mass, containing stellar and gas mass,

$$M_{tot} = M_{\star} + M_{gas}. \tag{47}$$

The system begins with $\mu = 1$ and a metallicity $Z = 0$, which is defined as the metal mass fraction of the gas,

$$Z = \frac{M_Z}{M_{gas}}. \tag{48}$$

The equation governing the evolution of the gas in the system is

$$\frac{dM_{gas}}{dt} = -\psi(t) + E(t), \tag{49}$$

where $\psi(t)$ is the Star Formation Rate (SFR) and $E(t)$ is the rate at which dying stars restore both enriched and unenriched material into the ISM at time t,

$$E(t) = \int_{m(t)}^{\infty} (m - M_R)\psi(t - \tau_m)\phi(m)\mathrm{d}m. \tag{50}$$

Here M_R is the remnant mass and τ_m is the lifetime for a star of mass m. Equation 49 can only be solved analytically, when simplifying equation 50, by assuming that all stars above a specific mass (m_{IRA}) die instantaneously and all stars below that limit live forever. This approximation is referred to as Instantaneous Recycling Approximation (IRA) and yields

$$R(m_{IRA}) = \int_{m_{IRA}}^{\infty} (m - M_R)\phi(m)dm, \tag{51}$$

the total mass fraction restored into InterStellar Medium (ISM) by a stellar generation. R depends on the IMF and on metallicity and varies between 0.2 and 0.5 for the usually adopted $m_{IRA} = 1\,M_\odot$.
Another important quantity is the *net yield per stellar generation*:

$$y_Z = \frac{1}{1-R}\int_1^{\infty} m p_{Zm}\phi(m)dm \tag{52}$$

where p_{Zm} is the fraction of newly produced and ejected metals by a star of mass m, which is referred to as *net stellar yields*.
With IRA equation 50 can be rewritten,

$$E(t) = \psi(t)R, \tag{53}$$

which also simplifies equation 49

$$\frac{dM_{gas}}{dt} = -\psi(t)(1-R). \tag{54}$$

Focusing on metals only the equation governing the evolution writes

$$\frac{d(ZM_{gas})}{dt} = -Z\psi(t) + E_Z(t), \tag{55}$$

and again, under the assumption of IRA, the convolution in the metal feedback,

$$E_Z(t) = \int_{m(t)}^{\infty} [(m - M_R)Z(t-\tau_m) + m p_{Zm}]\psi(t-\tau_m)\phi(m)dm, \tag{56}$$

can be avoided by replacing with R,

$$E_Z(t) = \psi(t)RZ(t) + y_Z(1-R)\psi(t). \tag{57}$$

This can be substituted in equation 55 and, after some algebraical manipulation, yields

$$\frac{dZ}{dt} = y_Z(1-R)\psi(t). \tag{58}$$

Dividing by equation 54 it follows

$$\frac{dZ}{dM_{gas}}M_{gas} = -y_Z, \tag{59}$$

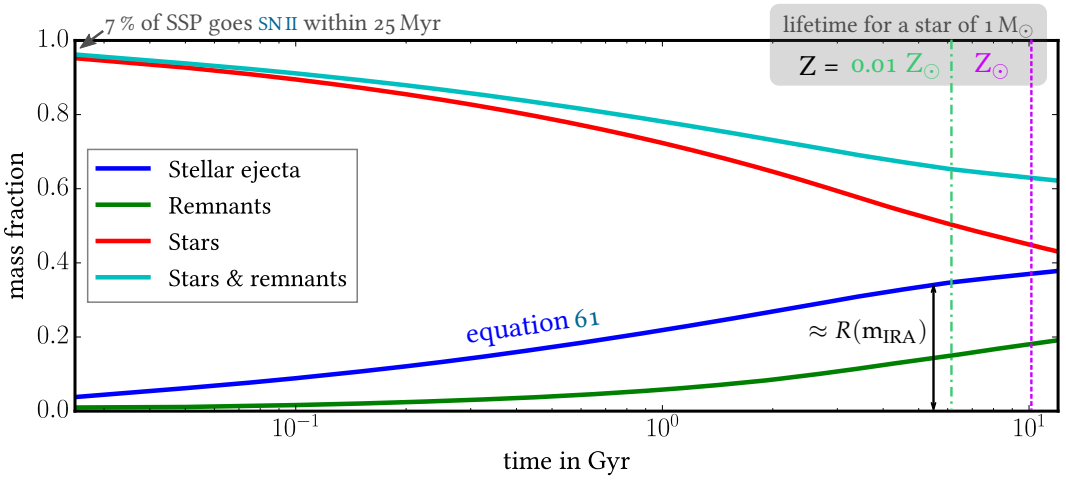

Figure 4.1: The time evolution of the mass fractions of an SSP with $Z = Z_\odot$ and JJ-model IMF from 0.025 to 12 Gyr on a logarithmic time scale. The lifetime of a Solar mass star with metallicity $Z_\odot$ and $0.01\,Z_\odot$ are indicated with the dashed magenta line and the dash-dotted green line respectively.

which, after integrating over $M_{gas}(0) = M_{tot}$ and $M_{gas}(t)$ and $Z(0) = 0$ and $Z(t)$., has the following analytic solution

$$Z = y_Z \ln\left(\frac{1}{\mu}\right). \tag{60}$$

Remarkably, the resulting metal enrichment is independent from the SFR.

Due to the crude approximation, which is dominated by the IRA, the simple model is not a good representation of the metal evolution of our Milky Way (MW). One major shortcoming is the *G-dwarf problem* which was discovered by van den Bergh [1962] and Schmidt [1963] and refers to the overprediction of metal-poor stars by the model, which is not observed in Solar Neighbourhood stars. One obvious solution to this problem is to start from pre-enriched gas. The simple model can be extended to account for *secondary elements*, gas infall, or outflow. But it is not able to reproduce the α-enhancement of old stars, see discussion in section 1.4.7, unless the IRA is relaxed.

the production of secondary *elements is depending on the initial abundance of a star, contrary to* primary *elements*

To illustrate the impact of the IRA, the mass budget over time for a SSP with $Z = Z_\odot$ and JJ-model IMF is displayed in figure 4.1. The stellar lifetimes ($\tau(m, Z)$) are taken from Argast et al. [2000] and for simplicity it is assumed that they eject all their feedback at the end of their life, meaning that stellar wind feedback is delayed. For the remnant mass (M_R from equation 50) left from AGB stars and SuperNova of type II (SN II) the values of Karakas [2010] and Nomoto et al. [2013] are adopted respectively.
If the metal-dependency of $\tau(m)$ is neglected, so that it can be inverted $\tau^{-1}(t)$, the cumulative stellar feedback, which is depicted as the blue curve in figure 4.1, can be stated in terms of R (c.f. equations 50 & 51),

$$\int_0^t E(t)\mathrm{d}t = R(\tau^{-1}(t)). \tag{61}$$

For $Z = Z_\odot$ and $m_{IRA} = 1\,M_\odot$ this means that the instantaneously returned material is about 38 % of the SSP mass. Without IRA the feedback would be distributed over a time span of 10,3 Gyr and feedback from low-mass and high-mass stars would be well separated.
For SN II feedback IRA is a well justified approximation, because the lifetime of massive stars is too short to be resolved with 25 Myr, which is the time resolution of the JJ-model. But SN II only constitutes about 7 % of the SSP and their overall feedback sums to 4 %, with the missing mass being confined in compact remnants.
It should be mentioned that R is highly dependant on the assumed IMF. For Kroupa et al. [1993] (KTG 93) IMF the SN II feedback is 5 % and $R(m_{IRA}) = 0.3$. The respective quantities for Chabrier [2003] (Chabrier 03) IMF are 0.14 and 0.43.
Another issue that can hardly be implemented into an analytical model is metal-dependency. As shown in the grey box of figure 4.1 stellar lifetimes change considerably with metallicity. Therefore the yield of stars depends on the initial abundance of the star. With numerical integration the metal-dependence can be taken into account and the assumption of IRA can be relaxed.

4.2 CHEMPY – A NUMERICAL CHEMICAL ENRICHMENT CODE

Chempy is a Python implementation of a simple chemical enrichment model, written by the author and intended for open-source publication. It was designed to be modular and fast with the aim to explore a huge parameter space with MCMC simulations. After minor cleaning of the source code, Chempy will be staged publicly[1] for everybody to use and contribute. This is intended to help comparing and reproducing results of chemical evolution modelling.
So far a one zone model with gas infall is implemented so that it follows the chemical evolution of the thin disc. It can be easily extended for other purposes, e.g. mixing of different zones or Galactic outflows.
In the following the various routines of the code will be explained and put into their astrophysical context. The possible choices will be indicated together with the default model parameters.

4.2.1 SOLAR ABUNDANCES

Solar abundances are very important because most observations are normalised with respect to the Sun. As the model calculates mass fractions, Solar abundances are necessary in order to compare the outcome with observations. So far the user can chose between two different sets of Solar abundances, namely Asplund et al. [2009] and Lodders et al. [2009, tab.6], with minor differences in the metallicity ($Z_\odot = 0.0134$ and $Z_\odot = 0.0141$, respectively) and also in element ratios for example in [O/Mg].

1 The code will be available at github: https://github.com/SIKz17/Chempy.

4.2.2 STAR FORMATION HISTORY

Chemical evolution models usually facilitate a Schmidt law, which connects the gas surface density with the rate of star formation [Chiappini et al., 1997]. In Chempy, the Star Formation History (SFH) and the infall rate can be fixed separately, because the JJ-model already provides constraints for the thin disc star formation. The default is the global SFH as depicted in the upper panel of figure 3.1, which begins 12 Gyr ago, peaks around 10 Gyr look-back time and slowly declines until the present day. The time resolution is 25 Myr, resulting in an array of 481 mass values, which are provided in units of $\frac{M_\odot/pc^2}{Gyr}$. The total mass formed into stars is

$$M_{SFR} = \int_{0\,Gyr}^{12\,Gyr} SFR(t)dt \simeq \sum_{i=0}^{480} SFR(t_i). \tag{62}$$

The functional form of the JJ-model SFH can be directly manipulated and other forms can be easily included.

4.2.3 GAS INFALL

For the gas infall, the user has the choice between different functional forms. The default is an exponential function,

$$\dot{G}(t) \propto e^{\lambda_{infall} t} \tag{63}$$

with λ_{infall} being the *infall decay rate*. The overall infalling mass is normalised with respect to M_{SFR} multiplied by the *infall scaling factor* γ_{infall},

$$M_{infall} = \gamma_{infall} M_{SFR}. \tag{64}$$

Also the elemental composition of the gas infall can be chosen from primordial over α-enhanced to Solar. The default being [Fe/H]=-3 dex and an [α/Fe]=0.4 dex.

4.2.4 YIELD TABLES

In order to calculate the feedback, yield tables are needed in machine readable form. The user can chose between different authors for the various feedback processes. The yield should be given as the feedback of both enriched and unenriched material, as in equation 50, and will be normalised to the stellar mass.

4.2.4.1 SUPERNOVA OF TYPE II

The default is from the review yield set of Nomoto et al. [2013]. It provides feedback for metallicity $Z \in [0, 0.001, 0.004, 0.008, 0.02, 0.05]$, the masses $M/M_\odot \in [13, 15, 18, 20, 25, 30, 40]$, and all the elements up to germanium-32. They also provide feedback for HyperNova (HN), assumed to occur at 50 % rate for stars more massive than 20 $M_\odot$, which slightly changes the chemical composition of the overall ejecta.
Other yield sets for massive stars are from Chieffi and Limongi [2004], Francois et al. [2004] and Pignatari et al. [2013].

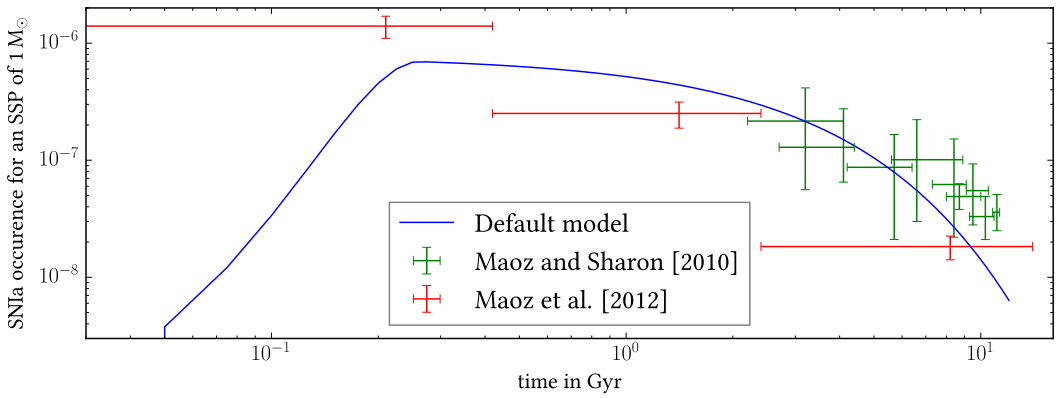

Figure 4.2: The occurrences of **snIa!** for an SSP of one $M_\odot$ over time in with logarithmic axes. The default Chempy model prescription with the fiducial parameters from equation 74 are used. For comparison the data of Maoz and Sharon [2010] and Maoz et al. [2012] are plotted.

4.2.4.2 AGB STARS

For Asymptotic Giant Branch (AGB) stars the default yields were taken from Pignatari et al. [2013]. They provide feedback for metallicity $Z \in [0.01, 0.02]$,the masses $M/M_\odot \in [1.65, 2, 3, 5]$, and all the elements up to bismuth-83. The alternative yield set is coming from Karakas [2010]

4.2.4.3 SUPERNOVA OF TYPE IA

For SuperNova of type Ia (SN Ia) only one yield set is available coming from Iwamoto et al. [1999]. They provide the feedback for metallicities $Z \in [0.0001, 0.02]$ including all elements from carbon-6 to zinc-30.

4.2.5 IMF

The IMF ($\phi(m)$) is one of the central parameters as it determines the mass fractions of stars going into the individual feedback processes. The choice includes the IMFs from chapter 3 and all parameters can be freely varied. The default is the new JJ-model IMF determined in Rybizki and Just [2015], but with an additional break at $m_2 = 6\,M_\odot$ and a *high-mass index*, α_3.
Not only the mass but also the number fraction of stars can be queried. The IMF is calculated in linear steps between $m_{low} = 0.08\,M_\odot$ and $m_{up} = 100\,M_\odot$ and is normalised to unity,

$$\int_{m_{low}}^{m_{up}} m\phi(m)\mathrm{d}m = 1. \tag{65}$$

The mass limits and the number of steps can be set at will. A good compromise between accuracy and speed is reached at 10^5 mass steps.

4.2.6 YIELD TABLE OF AN SSP

In order to calculate the yield of an SSP it is necessary to declare the mass range in which a specific feedback process acts. In the default model of Chempy, mass ranges similar

to the Nomoto et al. [2013] chemical enrichment model are used, but can also be varied freely. From $m_{low} = 0.08\,M_\odot$ to $m_{AGB,low} = 0.8\,M_\odot$, no feedback is necessary because stars live longer than 12 Gyr. AGB feedback will be calculated for stars between $m_{AGB,low}$ and $m_{AGB,up} = 8\,M_\odot$. The feedback of SN II is calculated for masses of $m_{SNII,low} = 10\,M_\odot$ and $m_{SNII,up} = 50\,M_\odot$ and SN Ia are assumed to come from stars with $m_{SNIa,low} = m_{AGB,low}$ and $m_{SNIa,up} = m_{SNII,low}$. The time delay function of SN Ia,

$$DTD(t) = \begin{cases} \exp\left(\frac{1}{2}\left(\frac{t-t_{peak}}{\sigma_{SNIa}}\right)^2\right), & \text{if} \quad t < t_{peak} \\ \exp\left(-\frac{(t-t_{peak})}{\tau_{SNIa}}\right), & \quad\quad\; t \geq t_{peak} \end{cases} \tag{66}$$

is parametrised using a Gaussian before the *time of peaking SN Ia occurrence* (t_{peak}) and an exponential with decay time $\tau_{SNIa} = 2.5$ Gyr thereafter, which can be inspected in figure 4.2 for the parameters derived in equation 74, together with data from Maoz and Sharon [2010] and Maoz et al. [2012]. Noteworthy, the data has not been used in the MCMC simulation to obtain the SN Ia parameters, though they guided the prescription of the Delay Time Distribution (DTD) functional form.
In the default model σ_{SNIa} is related to the peak time as $\sigma_{SNIa} = \frac{1}{4}t_{peak}$. The number of SN Ia events (n_{SNIa}), distributed with the DTD over a time span of 12 Gyr, is determined by the *SN Ia number fraction* β_{SNIa}, of stars in the SN Ia mass range that explode,

$$n_{SNIa} = \beta_{SNIa} \int_{m_{SNIa,low}}^{m_{SNIa,up}} \phi(m)\mathrm{d}m. \tag{67}$$

For mass conservation, the mean remnant mass ($\overline{M_R}$) per SN Ia is subtracted from the remnants of the SSP. Then the missing mass, for reaching the Chandrasekhar limit, is subtracted from the hydrogen in the ISM and turned, together with the remnant, into the SN Ia feedback, which goes back into the ISM. In this way the single-degenerate progenitor model is reproduced, though the tail of the DTD also accounts for the longer time needed for the in-spiral of the double-degenerate model.
The feedback from stars of the mass range between $m_{AGB,up}$ and $m_{SNII,low}$, referred to as super-AGB, is taken into account by feeding back the initial stellar composition into the ISM and leaving behind a compact remnant, made up from 13 % of the initial stellar mass, as in Kobayashi et al. [2011, sec.2.1]. Similarly for stars more massive than $m_{SNII,up}$ the initial composition is given back via stellar winds and a Black Hole (BH) with 25 % of the initial mass of the star is created.

After fixing the feedback processes, the mass return per time needs to be determined from IMF, using stellar lifetimes. In Chempy the metal and mass-dependent lifetimes of Raiteri et al. [1996, eq.3] and Argast et al. [2000] are included, with the latter as default and only small differences between the two. Because the metallicity of an SSP is fixed, the mass of dying stars (Δm) can be calculated for each time step (t_i),

$$\Delta m(t_i) = \int_{\tau^{-1}(t_i)}^{\tau^{-1}(t_{i-1})} m\phi(m)\mathrm{d}m. \tag{68}$$

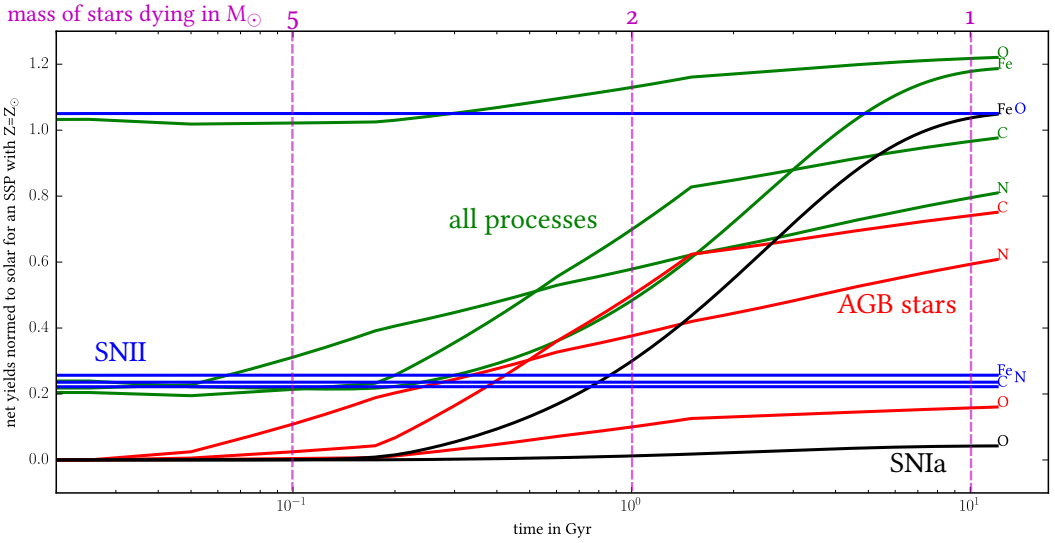

Figure 4.3: Net yields of an SSP with $Z=Z_{\odot}$ normed to Solar for the different feedback processes. The default model of Chempy, with the parameter values of equation 74, is used and the feedback is plotted over time. Masses of stars dying are indicated in magenta dashed lines.

In order to distribute $\Delta m(t_i)$ across the elemental and remnant mass fractions of the total SSP feedback, the yield tables are interpolated linearly in mass and metallicity for the corresponding processes at work for stars with initial mass between $\tau^{-1}(t_{i-1})$ and $\tau^{-1}(t_i)$. The resulting table is also keeping track of the supernova events taking place and the White Dwarfs (WDs) being produced over time.
In order to investigate the feedback from specific processes only, they can be switched on and off at will and plotted in different representations, like total mass fractions or net yields normed to Solar as depicted in figure 4.3. The yields of oxygen, carbon, nitrogen and iron are shown for a Solar metallicity SSP over time, using the default Chempy model with the fiducial values from equation 74. The SN II yield in blue contribute the bulk of oxygen and does not change with time, as all SN II explode after the first time step. SN Ia contribute most of the iron and the long decay time (τ_{SNIa}) is dominating the time-dependence of the iron feedback.
An interesting feature of the AGB yields is that carbon is mostly produced in low-mass AGB stars (it takes more time) and nitrogen in high-mass AGB stars. This means that the carbon over nitrogen ratio is potentially sensitive to the IMF, which can be investigated in a future study.
In the chemical evolution of the thin disc all of these feedback processes work at the same time, which is indicated in green in figure 4.3 for a single SSP. Remarkably, the major contribution of the α elements, represented by oxygen here, can be attributed to SN II, for iron it is SN Ia, and AGB stars produce the bulk of carbon and nitrogen. This means that these elements are sensitive to the feedback of the respective processes, which is why they are used in section 4.5 to guide the MCMC simulation.

4.2.7 INITIAL CONDITIONS

As a last step, before the chemical evolution model can be started, the initial gas mass and its elemental abundances need to be set. The default is an amount of $G_0 = 3 \frac{M_\odot}{pc^2}$ with [Fe/H]=-0.7 dex and an α-enhancement of 0.4 dex. This should simulate conditions of an ISM that has experienced fast enrichment by a pronounced initial burst of star formation.

The arising question is, what part and evolution of the MW is the model actually reproducing. The JJ-model SFR is only valid for the thin disc at Solar Galactocentric distance. When speaking of chemical enrichment, gas flows and radial migration of stars, which are not well constrained, should be taken into account. Otherwise the elemental abundances of Solar Neighbourhood stars are impossible to reconcile with the present-day cosmic abundance standard as inferred from young O and B-stars [Nieva and Przybilla, 2012]. Excellent approaches to model the chemical enrichment of the whole disc can be found in Schönrich and Binney [2009a]; Minchev et al. [2013]; Kubryk et al. [2015].

So far the Chempy model is too simplistic incorporate radial migration but it should be extended in the future. The approach here is to look how far this simple model can approximate the reality as inferred from observations.

4.2.8 TIME INTEGRATION

The main program evolves the chemical model in the following way, which is also represented in the triangular matrix of equation 69 where the diagonal represents the chemical abundance state of the model and the upper right holds the yield tables of the different SSPs.
The simulation starts at $t = 0$ Gyr, column s_0 and row t_0, with the initial gas mass and adds the gas from the infall. Then the mass $\mathrm{SFR}(t_0)$ of the first SSP is subtracted and turned into stars, inheriting the elemental abundance of the gas. Lastly, the feedback table for the first SSP, Δm_0, is calculated for all times ($s_i, i \in 0, 1, ..., 480$), which fills up the first row.
Now the next time step (t_1, s_1) can be iterated. First the feedback $\Delta m_0(s_1 - t_0)$ is calculated, with remnants being kept separately. Then the gas infall of that time step is added, after which the second SSP is formed. Lastly, the feedback for that SSP until $s_{480} - t_1$ is calculated and the next iteration takes place.
For each of those the feedback just needs to be added up from the values in the same column above. This is done until $t_{480} = s_{480} = 12$ Gyr, except the gas turns negative, due to wrongly prescribed infall, which causes the simulation to prompt an error.

$$
\begin{array}{c}
 \\
t_0 \\
t_1 \\
t_2 \\
\vdots \\
t_{480}
\end{array}
\begin{array}{c}
\begin{array}{ccccc} s_0 & s_1 & s_2 & ... & s_{480} \end{array} \\
\begin{pmatrix}
G_0 + \dot{G}(t_0) - \mathrm{SFR}(t_0) & +\Delta m_0(s_1 - t_0) & +\Delta m_0(s_2 - t_0) & ... & +\Delta m_0(s_{480} - t_0) \\
0 & \dot{G}(t_1) - \mathrm{SFR}(t_1) & +\Delta m_1(s_2 - t_1) & ... & +\Delta m_1(s_{480} - t_1) \\
\vdots & \ddots & \dot{G}(t_2) - \mathrm{SFR}(t_2) & ... & +\Delta m_2(s_{480} - t_2) \\
\vdots & 0 & \ddots & \ddots & \vdots \\
0 & \dots & \dots & 0 & \dot{G}(t_{480}) - \mathrm{SFR}(t_{480})
\end{pmatrix}
\end{array}
\tag{69}
$$

Thanks to the Python library numpy [van der Walt et al., 2011], these array manipulations are reasonably fast. On a modern processor a single simulation, including all elements, takes about 20 s.

4.2.9 OUTPUT

The outcome of a simulation can be analysed with different plotting routines that are implemented. Also the different yield sets can be investigated. The program is written in such a way that it can be called by an MCMC in order to explore the parameter space of input functions. For that also a probability measure is needed, the construction of which is explained in section 4.4.
Since a large simulation should not be interrupted, the program, by default, gives a prompt upon failure, which usually happens because of negative gas, and returns a probability of $-\infty$.

4.3 MAPPING MODEL OUTCOME INTO THE SPACE OF OBSERVABLES

Before a likelihood can be constructed a data set with discriminative power for the problem under investigation needs to be found and the model needs to be prepared in such a way that it represents the observations as good as possible. First the data is presented and then the way, in which the model is mapped into the space of observables.
The method has also been described in a submitted conference proceedings paper [Just and Rybizki, 2015].

4.3.1 DATA

A homogeneous set of high quality abundances of around 10^5 stars have been published in the APO Galactic Evolution Experiment [Alam et al., 2015] (APOGEE) survey. A catalogue for a sub-sample of 20,000 RC stars with added distances by Bovy et al. [2014] is used here, because spatial cuts can be applied to the stars. All stars with 7.5 kpc < R_{Gal} < 8.5 kpc and -150 pc < Z_{Gal} < 150 pc are selected in order to stay within the locus of the JJ-model. This yields a sample of 412 RC stars, for which up to 15 elemental abundances are available.

4.3.2 MODEL

With Chempy it is possible to reproduce the selections, as applied to the data in the previous section. This is realised by taking the relative chemical abundances of the gas at each time-step and weight them with the age-distribution of the stellar sample. In order to reproduce Solar Neighbourhood stars with a lifetime > 12 Gyr the global SFR of the JJ-model needs to be corrected for the scale height dilution (see discussion in section 3.2.1). These relative weighting factors are represented in the N-body masses of the lower panel of figure 3.1 and also by the blue dashed curve in the upper panel of figure 4.5.
Additionally, the age distribution of a specific stellar type, e.g. RC stars, can be reproduced with Galaxia, using PARSEC [Bressan et al., 2012] isochrones. It is realised by feeding the JJ-model parameters and a flat SFR into Galaxia and apply the (e.g. photometric) cuts, as visualised in figure 4.4, to the resulting stellar sample. For RC and old MS stars the relative age distributions are shown in the upper panel of figure 4.5.
Multiplying these stellar type age distributions (e.g. the magenta line from figure 4.5, for RC

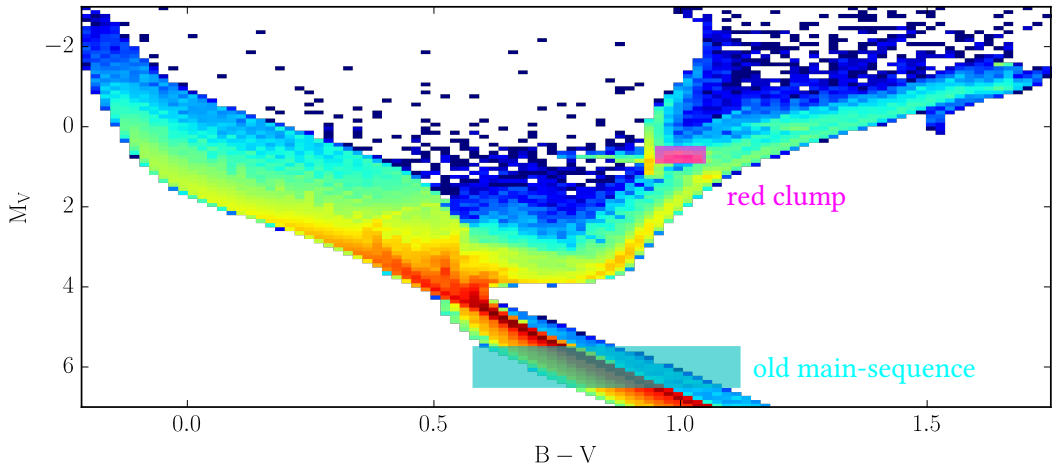

Figure 4.4: Selection of specific stars in the CMD. The stars have been synthesised with a flat SFR and the JJ-model parameters using Galaxia and their binned density is shown in logarithmic colour code. The RC selection is shown in magenta and the old MS in cyan. The corresponding age distribution of these selected stellar samples can be inspected in figure 4.5

stars) with the age distribution of the JJ-model, which represents a spatial selection (e.g. the blue dashed curve of figure 4.5, for the Solar Neighbourhood), and using the resulting relative age distributions to weight the abundances from the chemical evolution model, gives a very good approximation of the abundance distribution derived from stars with similar (spatial and stellar type) cuts.

To illustrate this effect, the model is compared to RC stars for different heights above the Galactic plane in figure 4.6. It is worth noting that, even though the model stays the same for all three heights and the APOGEE RC stars become metal-poorer with height, the age-weighted model tracks the difference quite well. One caveat is that the thick disc is not modelled, which is contributing with an increasing stellar fraction with increasing height above the Galactic plane. On the other hand, since the RC stars are quite young (see figure 4.5), only few of those should come from the thick disc.

The difference for different stellar populations in iron abundance can be inspected for the Solar Neighbourhood in the lower panel of figure 4.5. For comparison the local APOGEE RC sample is also plotted. Without the stellar type selection, the local model abundance distribution would be incompatible with the data. The RC model distribution is still off but resembles the data much better. Beware that the model used to plot figures 4.5 & 4.6, is not containing the fiducial parameter values yet and just used here to illustrate the selection effects. The peak at -0.9 dex for the old MS is due to the global SFR peak and the pre-enriched gas mass G_0 from which the simulation starts.

These two selection effects should be the ones with strongest effect on the APOGEE RC sample, as the survey is designed to minimise observational biases in age and metallicity [Zasowski et al., 2013] and represent the Galactic giant star distribution.

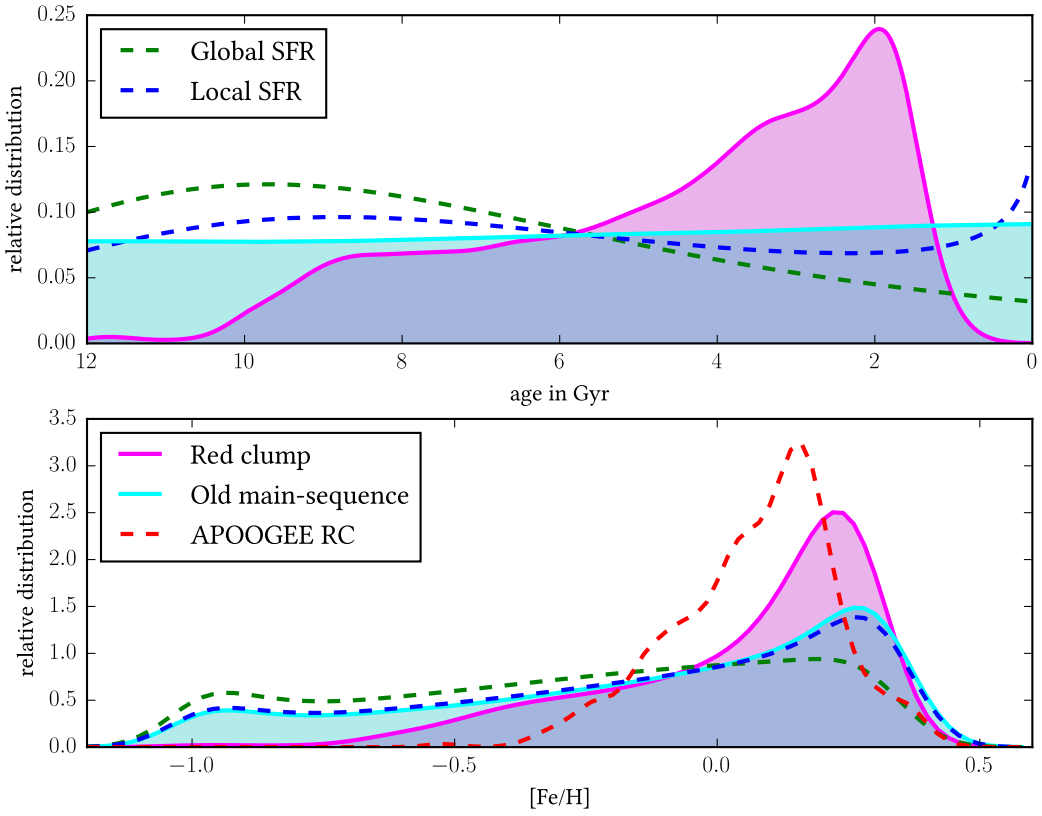

Figure 4.5: Distribution functions of RC stars in magenta, old MS stars in cyan as selected in figure 4.4, the global JJ-model in dashed green, and a local JJ-model representation in dashed blue. The upper panel shows the age distribution of the different selections and the lower panel the resulting iron distribution functions with an added Gaussian scatter of 0.1 dex. For comparison the local APOGEE RC sample distribution convoluted with its error is plotted. The chemical model parameter are the same as in figure 4.6, which are not the fiducial values.

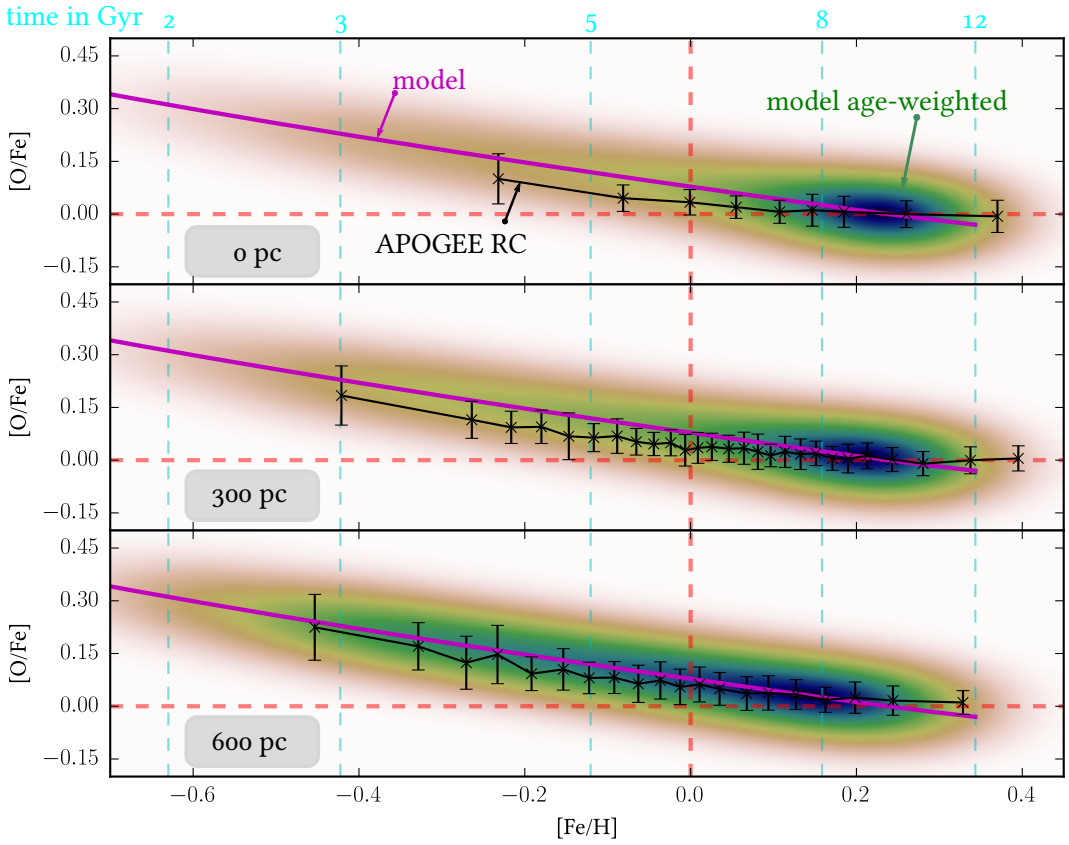

Figure 4.6: The changing α-enhancement with Galactic height is shown with the model in magenta and the 50 star average of the APOGEE RC sample. From upper to lower panel the height above the Galactic plane increases from 0 to 600 pc. The chemical model stays the same but its error-convoluted and age-weighted density distribution changes. The age distributions for RC stars and different heights above the Galactic plane from the JJ-model are used. In cyan the time evolution of the model is indicated. The model parameters are not the fiducial values from equation 74, but were randomly chosen, to illustrate the effect of the different age-distributions representing the spatial and stellar-type selection functions.

Table 9: The log-likelihood penalty for the model differing from the data, normed to standard deviations.

$\frac{m_i - d_i}{\sigma_i}$	0	1	2	3	4	5	6
$\ln\left(\frac{\mathcal{L}_i}{\mathrm{P}_{i,\max}}\right)$	0	-0.5	-2	-4.5	-8	-12.5	-18
$\frac{\mathcal{L}_i}{\mathrm{P}_{i,\max}}$	1	0.61	0.14	0.01	3.4×10^{-4}	3.7×10^{-6}	1.5×10^{-8}

4.4 POSTERIOR PRESCRIPTION

As Chempy is intended to extend the JJ-model and to further constrain its input parameters (especially the infall function ($\gamma_{\mathrm{infall}}, \lambda_{\mathrm{infall}}$), the high-mass index ($\alpha_3$), and the SN Ia parameters ($\mathrm{t}_{\mathrm{peak}}, \beta_{\mathrm{SNIa}}$), the used data sets need to be chosen accordingly.

4.4.1 LIKELIHOOD FROM DATA

Very few data are used in this first approach to determine the chemical evolution model parameters, because of the many subtleties involved in order to set the MCMC. In order to have a constraint on the infall and also on the supernova rates, the local present day gas mass fraction $\mathrm{G}_{\mathrm{p}} = 10.3 \pm 3$ [Kubryk et al., 2015] is used and the SN II over SN Ia ratio for MW like galaxies $\mathrm{SNII/SNIa} = 5 \pm 3$ based on Mannucci et al. [2005].
These quantities are assumed to be Gaussian distributed, which admittedly is an oversimplification, especially in the supernova rate case. In order to balance the likelihood penalty from different data sets as well as the penalty contribution from the priors easier, the Gauss approximation was chosen. The normalised log-likelihood (as well as the prior probability) for a model value (m_i) to represent the data value (d_i) with a standard deviation (σ_i), will be constructed as

$$\mathcal{P}_i = \ln\left(\frac{\mathcal{L}_i}{\mathrm{P}_{i,\max}}\right) = \ln\left(\frac{\mathcal{N}(m_i, d_i, \sigma_i)}{\mathcal{N}(d_i, d_i, \sigma_i)}\right) = \frac{(m_i - d_i)^2}{2\sigma^2}, \tag{70}$$

with $\mathcal{N}(x, \mu, \sigma)$ being the Gaussian distribution. The overall likelihood becomes a summation

$$\mathcal{P} = \sum_{i=1}^{n} \mathcal{P}_i \tag{71}$$

over all the data points. For reference the penalties for different standard deviations offset of observed values are given in table 9.

For the local sample of the APOGEE RC elemental abundances only four dimensions of the chemical space are used. The metal content ([M/H]) is the only abundance that is externally calibrated [Holtzman et al., 2015]. It is fitted, together with [α/M], [C/M] and [N/M], to the whole spectrum and treated as a stellar parameter, contrary to the other elements. Carbon and nitrogen are added because dredge up alters the C/N ratios, but the sum of both should remain relatively constant over the stellar lifetime of the star [Hawkins et al., 2015].
[C+N/M] constrains the AGB contribution to the chemical enrichment. [α/M] is mainly related to SN II, therefore [Fe/H] is added in order to have an element that is selectively

sensitive to SN Ia feedback.

The data points (for the Gaussian likelihood evaluation) are constructed from the element distribution function quantiles [5,25,50,75,95]. This yield five data points per elemental dimension, which is compared to the corresponding model value. For σ the median error given for the RC sample is taken.
Overall four times five correlated data points from elemental abundances are used to establish a statistic constraining the parameters. Together with the two data points G_0 and the supernova ratio they are intended to guide the MCMC parameter exploration into a position motivated by the observational data.

4.4.2 ASSIGNING PRIORS

Contrary to chapter 3, where flat priors are used, here the free parameters are constrained with relatively[2] relaxed Gaussian priors, taken into account realistic assumptions. For parameter like β_{SNIa} a prior distribution is not easy to anticipate a priori, so they were determined empirically through testing and also large σ values were chosen, in order avoid too tight parameter constraints. The Probability Density Functions (PDFs) representing the parameter priors are,

$$\begin{aligned}
\alpha_3 &= \mathcal{N}(\mu = 2.5,\, \sigma = 0.5)\,, && \text{(high-mass index)}\\
\beta_{\mathrm{SNIa}} &= \mathcal{N}(0.004,\, 0.002)\,, && \text{(number fraction of stars in the SN Ia mass range that explode)}\\
t_{\mathrm{peak}} &= \mathcal{N}(0.8\,\mathrm{Gyr},\, 0.3\,\mathrm{Gyr})\,, && \text{(time of peaking SN Ia occurrence)}\\
\gamma_{\mathrm{infall}} &= \mathcal{N}(0.8,\, 0.2)\,, && \text{(infall mass scaling factor)}\\
\lambda_{\mathrm{infall}} &= \mathcal{N}(-0.3,\, 0.2)\,. && \text{(infall decay rate)}
\end{aligned} \tag{72}$$

The MCMC is free to chose from the parameters, except when unphysical limits are violated, which results in Chempy returning a posterior of $-\infty$. Therefore the range of parameters is effectively confined to

$$\begin{aligned}
\alpha_3 &\geq 0\\
\beta_{\mathrm{SNIa}} &> 0\\
t_{\mathrm{peak}} &\geq 7.5\,\mathrm{Myr}\\
t_{\mathrm{peak}} &\leq 6\,\mathrm{Gyr}\\
\gamma_{\mathrm{infall}} &\geq 0.
\end{aligned} \tag{73}$$

As mentioned before $-\infty$ will also be returned when the gas mass becomes negative during the calculation.

2 The weight of the priors are five broad Gaussians, which compared to the likelihood with its 22 Gaussians from the data, contribute comparatively little to the final posterior probability.

4.4.3 REMARKS ON THE POSTERIOR SAMPLING

The log-posterior is obtained by adding the log-prior and the log-likelihood. It is returned to the MCMC, which requires the probability of a parameter position in logarithmic scale.

emcee is a Python implementation [Foreman-Mackey et al., 2013] of an affine invariant ensemble sampler for MCMC [Goodman and Weare, 2010]

As in chapter 3, *emcee* is used to sample the posterior PDF of the parameter space. In this specific case multiprocessing with 60 threads and walkers was used to speed up the calculation. On a small cluster with 16 modern processing units it takes about five hours to sample 10^5 values from the posterior, sufficient to approximate its distribution if the burn-in phase is not too long.
The initial parameters are assigned to each of the 60 walkers by drawing randomly from the Gaussian, $\mathcal{N}(\mu = \mu_{\text{prior}}, \sigma = \frac{1}{4}\mu_{\text{prior}})$, for each of the five parameters. Few walkers start with negative gas values, but the whole sample converges quickly to the equilibrium position of highest posterior probability.

4.5 RESULTS

The default model posterior PDF is approximated by the MCMC that is depicted in figure 4.7. Excluding the burn-in phase, which typically takes 50 steps with 60 walkers, a total of 26,000 samples were drawn from the posterior. The highest value is marked with a black cross in the 2D projections. The colour code spans from the best log-posterior value, -43.7 in red, to -51.7 in blue, which is the equivalent of a 4σ offset.

Overall the posterior distribution is well-behaved. Except for t_{peak} all marginalised parameter distributions are well approximated by a Gaussian with the highest value falling onto the mean of the distribution.
The strongest correlation is between β_{SNIa} and γ_{infall} because with increasing primordial gas mass also an increasing number of SN Ia is needed to match the metal and iron distribution. Similarly, but not as pronounced, α_3 is also correlated with the infalling gas mass. Minor correlations are between the number of SN Ia and the high-mass index, which is essentially the number of SN II. These correlate because the [α/M] distribution depends on their overall feedback matching. Also the infall time scale and t_{peak} are positively correlated, probably because if more gas is falling in earlier (e.g. λ_{infall} is smaller) then the metal enrichment need to act earlier as well.
The SN Ia peak time is, contrary to the other values, not tightly constraint by the used data. Maybe because the RC stars only sample a relatively young stellar population. Probably also because the DTD is a wide spread distribution. Shorter values are preferred, but the best posterior is obtained at 0.1 Gyr, though also shorter values could have been possible. In order to be easily comparable with other MCMC runs the Gaussian mean values of each parameter are adopted for the new fiducial model.

$$\begin{aligned} \alpha_3 &= 2.41 \pm 0.04, \\ \beta_{\text{SNIa}} &= 0.0056 \pm 0.0005, \\ t_{\text{peak}} &= 0.26\,\text{Gyr} \pm 0.17\,\text{Gyr}, \\ \gamma_{\text{infall}} &= 0.85 \pm 0.03, \\ \lambda_{\text{infall}} &= -0.44 \pm 0.05. \end{aligned} \tag{74}$$

When using these parameters the posterior obtains the following contributions. The log-

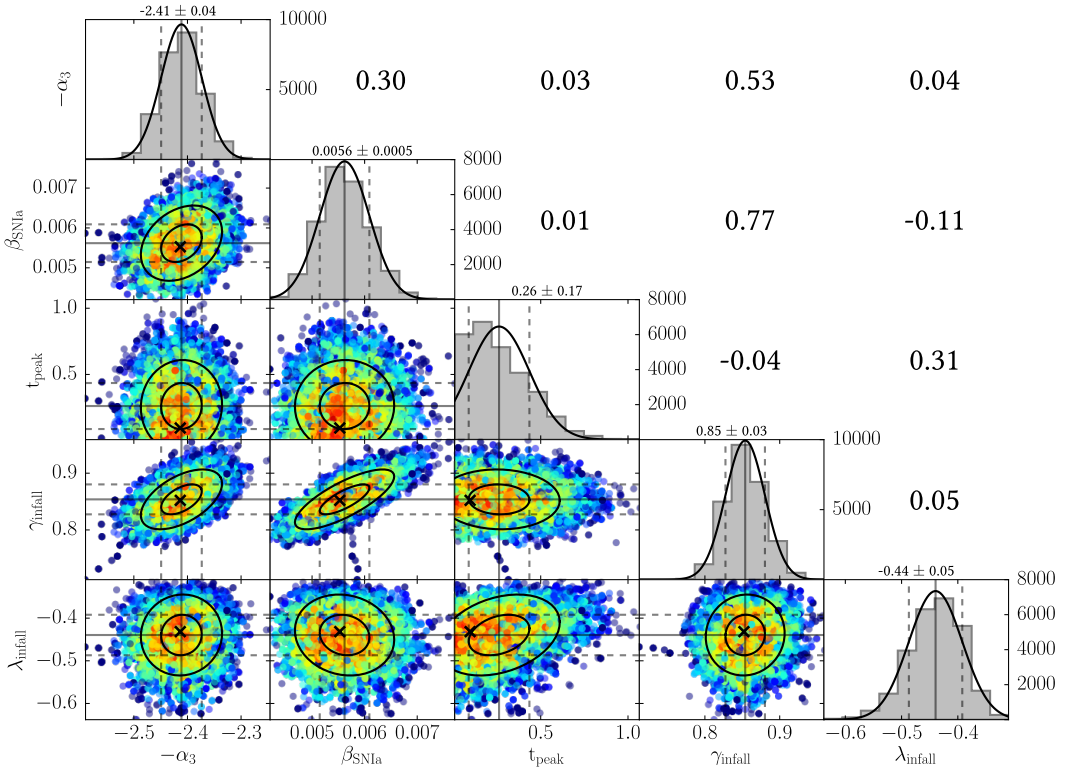

Figure 4.7: Marginalised parameter distribution of the MCMC sampling from the posterior. Each scatter plot shows the projected 2D parameter distribution with points colour-coded according to their posterior probability. The black cross indicates the position with highest posterior and ellipses encompass the 1σ and 2σ regions. The respective correlation coefficients are given at the position mirrored along the diagonal. Gaussian fits and histograms of the marginalised parameter distribution are given on the diagonal. The mean and standard deviation of each parameter is written above the histogram and are also indicated by solid and dashed grey lines.

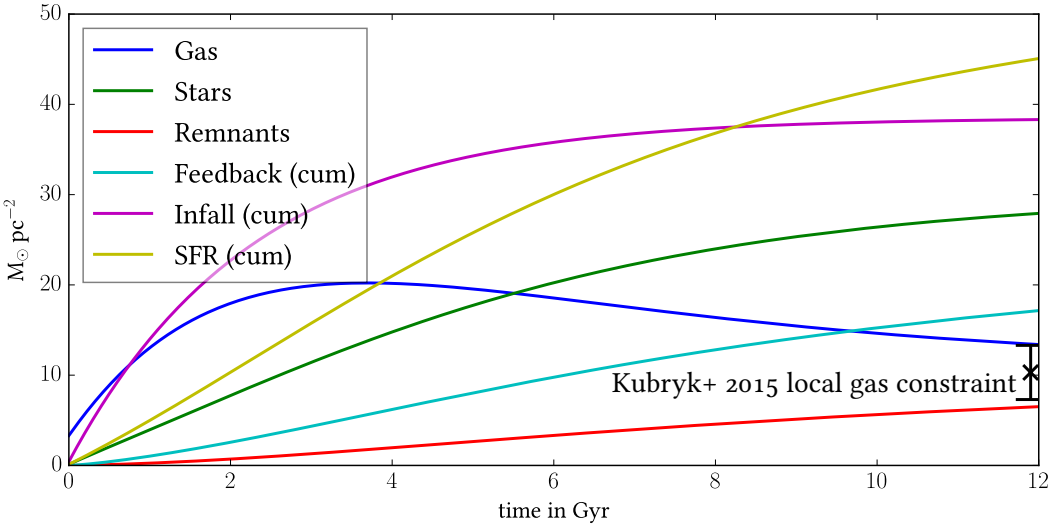

Figure 4.8: The fiducial model mass evolution over time. Gas mass, living stellar mass and remnant mass are shown in blue, green and red, respectively. The cumulative values of the stellar feedback, the infall and the SFR are indicated in cyan, magenta and yellow. The SFR is fixed by the JJ-model but the infall function parameters could vary freely (with respect to the priors) in the MCMC. The data constraint is indicated and the simulation settles at the upper end of the Kubryk et al. [2015] value.

priors add up to -2.2. The log-likelihood in total is -42.6. The gas mass at end, as indicated in figure 4.8 in blue together with other global model parameters, is 13.4 $M_\odot$ pc^{-2} contributing $\mathcal{P}_{gas}$ = -0.53. The SNII/SNIa ratio at the present day is also roughly one sigma off, with a value of 1.6 resulting in $\mathcal{P}_{SN}$ = -0.64. The abundance distributions from APOGEE RC stars yield log-likelihoods of

$$\begin{aligned} \mathcal{P}_{[Fe/H]} &= -14.82, \\ \mathcal{P}_{[M/H]} &= -14.05, \\ \mathcal{P}_{[\alpha/M]} &= -5.78, \\ \mathcal{P}_{[C+N/M]} &= -6.73. \end{aligned} \tag{75}$$

From these values it is clear that the main penalty, guiding the MCMC, is originating from the abundance data. This illustrates that the priors are not tightly constraining the parameter space, instead the abundance data has by far the largest impact on the posterior.
The compared metal distributions, together with the broken down likelihood contributions from each quantile, are illustrated in figure 4.9. The first four quantiles match quite well, with only minor likelihood penalties, as indicated at the top of the figure. The major penalty is contributed by the last 95 % quantile, ultimately originating from a metal-rich population, which could coincide with the α-rich young thin disc population found in recent spectroscopic surveys [Chiappini et al., 2015; Bergemann et al., 2014]. That indicates that the chemical enrichment of the MW disc is more complex than can be reproduced by the one zone model. Interestingly, the [Fe/H] matches quite well in the metal-rich part and also the [α/M] distribution fits very good.

Even though, other elemental abundances are not used to equilibrate the MCMC, the used metal, iron, *alpha* and C+N distributions should constrain the three feedback processes

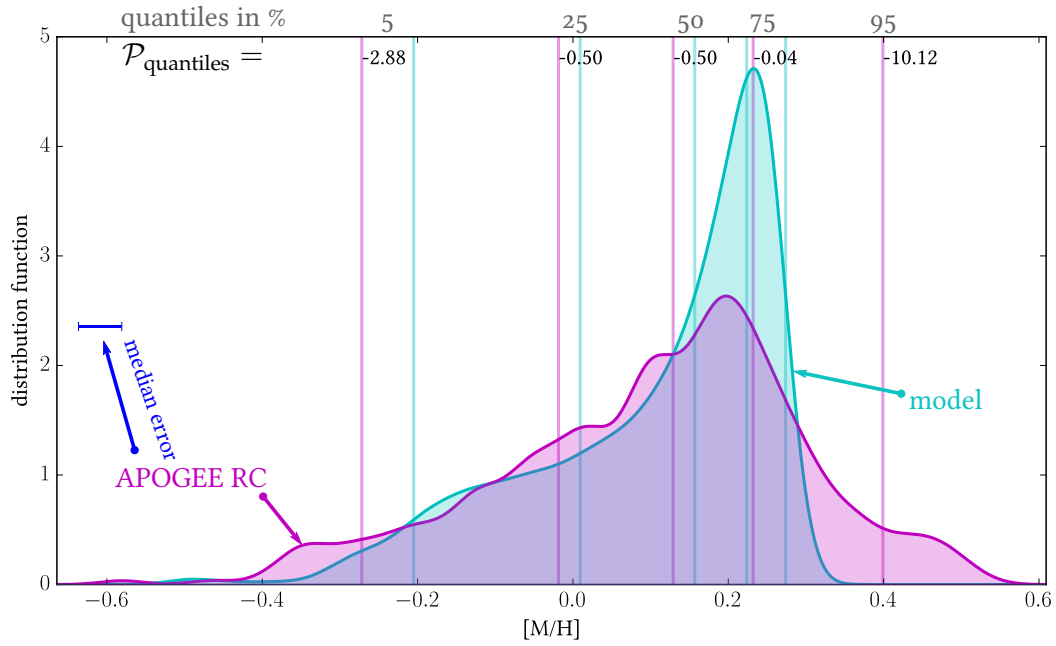

Figure 4.9: Metal distribution function of the fiducial model and the local APOGEE RC stars. The construction of the likelihood, from the difference of the quantiles, is indicated at the top.

well enough, to have reasonable abundance patterns for other elements, provided that the yield set is realistic. Two example elemental distributions, where it works well, are shown in figure 4.10 & 4.11. In figure 4.10 the sulphur-enhancement is shown for the age-weighted model and the local APOGEE RC sample. The correlation in the [S/Fe] - [Fe/H] plane is reproduced well, though the iron enrichment seems to be a little too strong in the model. A spurious effect can be seen in the beginning of the model, when the initial abundances for the gas at the beginning are lowered and then increase quickly. This happens due to the primordial gas infall and the metal-dependent stellar yields. After about one Gyr the dependence on the initial conditions seems to play a minor role and the model evolves smoothly.

Manganese is an element which, is also mainly produced in SN Ia. When plotting it with respect to the α-element magnesium, in the [Mn/Mg] - [Mg/H] plane, it should represent the increasing contribution of SN Ia. In figure 4.11 the model and the data are fitting quite well. Since the model was fitted using the iron and α over metal distribution, it is comforting that other elements representing the same processes are also fit quite well. Of course this is highly dependent on the yield sets used. Also not all elements are matched as good, since yields for some elements are not well determined and also the derived abundances from the APOGEE RC stars do have systematic biases. The hope is that, using modelling techniques like the one presented here, these discrepancies can be resolved.

4.5.1 DIFFERENT YIELDS

A major uncertainty, and also a source of potential bias, are the used yield sets for the different feedback processes. Therefore the MCMC was done repeatedly for various combinations of yields, leaving all the other parameters, observational constraints, initial conditions, and

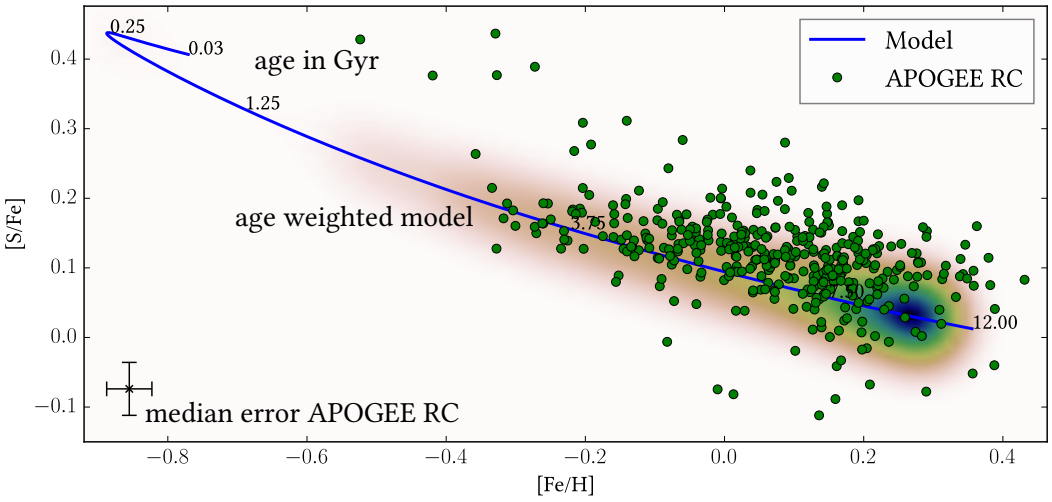

Figure 4.10: The [S/Fe] - [Fe/H] for the model and the local APOGEE rc stars is plotted. The age-weighted model, convolved with the observational error, is colour-coded in the background.

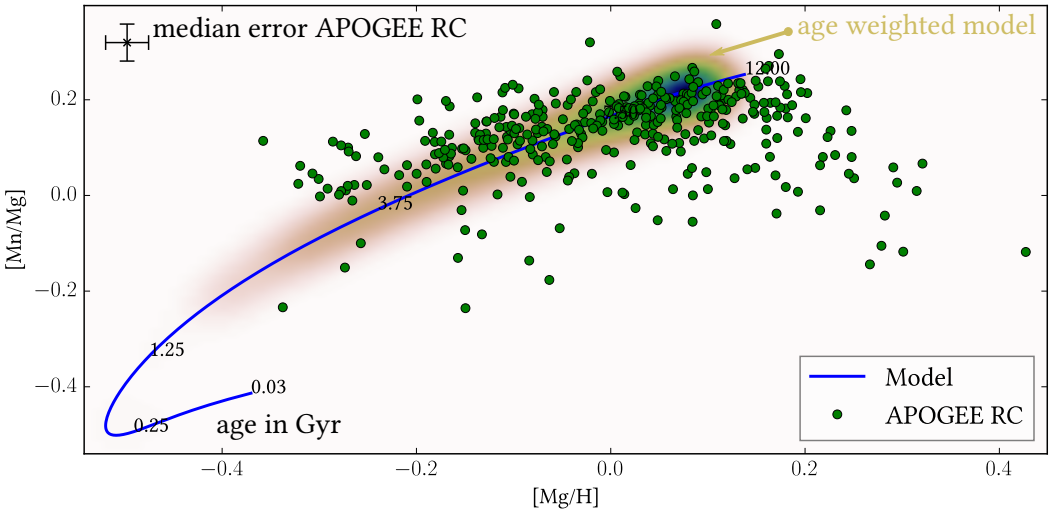

Figure 4.11: Same as figure 4.10 but for the [Mn/Mg] - [Mg/H] abundance plane.

Table 10: Equilibrium parameter positions and posterior values for MCMC runs using different yield sets

yield set		log-posterior	α_3		β_{SNIa}		t_{peak}		γ_{infall}		τ_{infall}	
AGB	SN II	maximum	μ	σ	μ	σ	μ	σ	μ	σ	μ	σ
Nugrid	Nomoto	-43.7	2.41	0.04	0.0056	0.0005	0.26	0.17	0.85	0.03	-0.44	0.05
Nugrid	Chieffi	-51.0	2.25	0.04	0.0056	0.0005	0.35	0.21	0.95	0.03	-0.51	0.06
Karakas	Chieffi	-63.2	2.15	0.04	0.0060	0.0007	0.35	0.21	0.96	0.04	-0.48	0.06
Karakas	Nomoto	-66.4	2.31	0.03	0.0062	0.0006	0.26	0.17	0.87	0.03	-0.44	0.05
Nugrid	Francois	-83.1	2.82	0.03	0.0041	0.0004	0.39	0.23	0.68	0.02	-0.35	0.03
Nugrid	Nugrid	-106.1	1.14	0.08	0.0085	0.0012	0.39	0.23	0.87	0.02	-0.58	0.07
median and sigma of all sets:			2.28	0.5	0.0058	0.0013	0.35	0.05	0.87	0.09	-0.46	0.07
Varying statistics for the model with Nugrid and Nomoto yields												
priors = $\sigma/2$		-47.9	2.42	0.04	0.0054	0.0004	0.57	0.15	0.84	0.02	-0.40	0.04
quantiles at [5,15,50,85,95]		-46.0	2.41	0.04	0.0056	0.0005	0.21	0.15	0.84	0.03	-0.43	0.04
Only [M/H] and [α/M]		-11.7	2.60	0.07	0.0044	0.0015	0.91	0.29	0.75	0.04	-0.60	0.08

priors the same. Each run samples at least 10,000 posterior values, excluding the burn-in. The results are listed in table 10. The best representation of the data is obtained when using the Nugrid [Pignatari et al., 2013] AGB yields together with Nomoto et al. [2013] yields for the high-mass stars.
When inspecting the whole table a good overview is gained about the preferred values of the parameters. The peak of the DTD at about 0.35 Gyr seems to be at lower values than a priori assumed. Maybe this is also due to the fixed delay time of 2.5 Gyr and the functional form of the DTD, which should be investigated in the future.
The high-mass index, which is most interesting with respect to the results from chapter 3 seems to favour the Salpeter [1955] value at about 2.3, where the four best yield set combinations are pointing. The last two yield sets, which are a bit off in terms of maximum posterior probability, favour a value at 2.8 and 1.1, respectively. Also for those the different correlations are at at work, as for example a lower SN Ia rate for less SN II as with the Francois et al. [2004] yields and the opposite with the Nugrid high-mass yields.

Overall, this shows that the model can find reasonable parameter values with different yield sets, without the necessity to tune the initial conditions of the MCMC. Other model ingredients should be tested as well and also the statistics should be further investigated. As a first small test, the MCMC runs were made, using the default model, but with changed quantiles, a reduced data set with only metallicity and α-enhancement, and priors with halved standard deviations. The results of these are shown in the lower part of table 10.
The *tightening* of the priors seems to have a minor effect, except for the loosely constraint t_{peak}. Changing the spacing of the quantiles has a very small effect on the best parameter values but decreases the maximum posterior obtainable. Probably because more weights are given on the tails of the distribution and getting more independent information from it, i. e. the summary statistic is more responsive, compared to two values that are directly next to each other. Only taking half of the elemental abundance data set significantly changes the parameter position of highest posterior. Of course the posterior also increases drastically as 10 values less are multiplied into the probability. In the α over iron plane a larger high-mass index and also later peak time for SN Ia is preferred, which traces the expected

time dependence of SN II to SN Ia feedback. This indicates that one of the other abundance distributions probably pushes the MCMC to a faster chemical enrichment. It also shows that with less data at hand the prior gets more important as its fractional contribution to the posterior increases.
The statistical tests show how sensitive the MCMC reacts on changing the used data sets. On the other hand, the priors and quantiles seemed to be well chosen as changing them has minor effects.

4.6 CONCLUSION

Chempy, a new, fast and versatile chemical enrichment code, intended for open-source publication, has been presented. A technique to use the output of Chempy and synthesise mock elemental abundances with the help of the JJ-model and Galaxia is introduced. An observational constraint is deduced, using the quantiles of abundance distributions as a summary statistic. This is then converted into a likelihood, assuming a Gaussian probability distribution for each quantile and applying it to the difference between mock and real data distributions. The four most important dimensions of the chemical abundance space data of APOGEE, [Fe/H], [M/H], [α/M] and [C+N/M], are turned into distribution functions, as inferred from Solar Neighbourhood RC stars. Together with observational constraints about the present-day local gas mass and the SN II over SN Ia ratio, they measure the model likelihood.
Five important parameters of the model, the IMF high-mass index (α_3), the number of SN Ia exploding (β_{SNIa}), the SN Ia peak time (t_{peak}), the infall mass fraction (γ_{infall}) and the infall time scale ($\lambda_{\mathrm{infall}}$), are given a reasonable prior distribution and an MCMC is used to sample the posterior PDF of the parameter space. This is done for six different combinations of yield sets with Nugrid [Pignatari et al., 2013] and Nomoto et al. [2013] giving the best results. Within that model the high-mass index of the IMF has a tightly constrained value of 2.41 with a standard deviation of only 0.04. When taking into account the systematics, with respect to the other four yield sets, best reproducing the observations, a value of 2.28 ± 0.09 is obtained.
In the future, other model parameters should also be tested for their impact on the obtained results. The model should be extended to track the thick disc evolution and to allow for multiple zones, which could be implemented using the isochrone formalism presented in Kubryk et al. [2015, eq. C3].

To the authors knowledge, this is the first time that the parameter space of a chemical enrichment model (in this case spanned by five main parameters) is explored, using Bayesian inference and an MCMC simulation to sample the posterior PDF, with respect to the likelihood of the chosen observational constraints. Similar approaches usually rely on a χ^2 minimal-distance-estimate and only sample a set of discrete parameter values (cf. Mollá et al. [2015]). The presented method here seems to be robust, as no change of initial parameters or further human supervision is necessary for the MCMC runs to converge, even for different yield sets. The chemical enrichment model is a good first-order approximation to the chemical evolution of the thin disc, as inferred parameters seem reasonable and other model outcome compares well with independent observations.
Overall, the forward modelling approach, using simple physical models and comparing

the outcome to real data, seems a promising way to infer crucial parameters of the MW evolution. With upcoming spectroscopic surveys the model parameters can be further constrained and it is intended to use dwarf abundances from Gaia-ESO [Gilmore et al., 2012] (GES), in order to be more sensitive to the early evolution of the MW disc.

5

SUMMARY

The stellar Initial Mass Function (IMF) was inferred from the local chemodynamical evolution model of the Milky Way (MW) disc of Just and Jahreiss [2010]. In a first attempt, volume-complete samples of Solar Neighbourhood stars from Hipparcos [Perryman et al., 1997] (Hipparcos) and low-mass star counts from Just et al. [2015], were used to constrain the IMF up to $6\,M_\odot$.
In order to infer the high-mass index, the modular chemical evolution code *Chempy*, was developed. Its outcome was mapped onto APO Galactic Evolution Experiment [Alam et al., 2015] (APOGEE) Red-Clump (RC) stellar elemental abundance distributions and their agreement was tested for different yield sets. The model favours a Salpeter-like high-mass slope and also determines infall and SuperNova of type Ia (SN Ia) parameters. The fiducial IMF values of the four-slope broken power-law are

$$\begin{aligned} \alpha_0 &= 1.26, \\ \alpha_1 &= 1.49 \pm 0.08, \\ \alpha_2 &= 3.02 \pm 0.06, \\ \alpha_2 &= 2.28 \pm 0.09, \\ m_0 &= 0.5, \\ m_1 &= 1.39 \pm 0.05, \\ m_2 &= 6, \end{aligned} \tag{76}$$

within the stellar mass regime, $0.08 < m/M_\odot < 100$. The errors given are derived from the Markov Chain Monte Carlo (MCMC) simulation and are valid within model assumptions, but observational biases or model systematics are not included. The values without errors, were fixed empirically, using observational constraints which were not included in the simulation.

The results were obtained with Bayesian statistics, applied to the forward modelling technique. Focus was laid on synthesising realistic mock samples and on the likelihood construction, which is a statistical measure, allowing MCMC algorithms to find model parameters, best representing the observational evidence. Vice versa the posterior Probability Density Function (PDF) can give insight on which data has the most discriminative power for the problem under investigation and also on the correlations between the different model parameters.
A desirable feature of the approach is that the likelihood of the abundance data is determined unsupervised. It is also much faster, than judging the matching of abundance patterns by eye. In the future it is intended to include two dimensional correlations of the data into the likelihood construction.
In conclusion, the presented technique is a valuable approach for the huge upcoming data sets which will increase the model complexity and, therefore, the demand for robust unsupervised parameter exploration.

6 OUTLOOK

With the dawn of Gaia [Lindegren et al., 2008] (Gaia) and the follow-up spectroscopic Gaia-ESO [Gilmore et al., 2012] (GES) survey, rich data sets are upcoming which will probe the chemical abundance and phase-space of the Milky Way (MW) in unprecedented detail. The analysis of these data and the incorporation of new-found structures will pose a huge challenge to Galaxy modelling. Techniques to lower the dimensionality of the data space, will become more important as shown by the first promising results from chemical tagging [Hawkins et al., 2015].
To account for the higher complexity, reflected by the data, the number of model parameters will increase. This will make parameter estimation techniques, which are able to incorporate lots of different data and at the same time capable of exploring a high-dimensional parameter space, a valuable asset.

It is planned to extend the local JJ-model to different Galactocentric radii. For the time being, the analysis of the parameter constraints, resulting from chemical abundances and possible extensions to *Chempy*, are considered. To compare the discriminative power and the highest posterior probability of different survey data like Bensby et al. [2014], APO Galactic Evolution Experiment [Alam et al., 2015] (APOGEE) or GES will be an interesting endeavour and might shed light on survey biases and selection functions.
A study of the Asymptotic Giant Branch (AGB) mass range and its impact on the mass-sensitive carbon and nitrogen abundances could further constrain the Initial Mass Function (IMF), independently from the approach in chapter 3. The inference of yield parameters should also be possible. It will be exciting to see the parameter constraints increasing, in parallel to the increase of observational data incorporated into the MW model analysis.

BIBLIOGRAPHY

Alam, S. et al. 'The eleventh and twelth data releases of the sloan digital sky survey: final data from SDSS-III'. *ApJS*, 219(1):12, 2015. URL http://adsabs.harvard.edu/abs/2015ApJS..219...12Ahttp://stacks.iop.org/0067-0049/219/i=1/a=12?key=crossref.9b82c10044d9c570d778627932bca465. (Cited on pages xv, 19, 76, 91, and 93.)

Albrecht, A. et al. 'Reheating an Inflationary Universe'. *PhRvL*, 48(20):1437–1440, 1982. URL http://adsabs.harvard.edu/abs/1982PhRvL..48.1437. (Cited on page 5.)

Alpher, R. A., Follin, J. W. and Herman, R. C. 'Physical Conditions in the Initial Stages of the Expanding Universe'. *PhR*, 92(6):1347–1361, 1953. URL http://adsabs.harvard.edu/abs/1953PhRv...92.1347A. (Cited on page 7.)

Anderson, E. and Francis, C. 'XHIP: An Extended Hipparcos Compilation'. *Astron. Lett.*, 38(5):331–346, 2012. URL http://adsabs.harvard.edu/abs/2012AstL...38..331A. (Cited on pages 47 and 48.)

Anderson, T. W. and Darling, D. A. 'Asymptotic Theory of Certain "Goodness of Fit" Criteria Based on Stochastic Processes'. *Ann. Math. Stat.*, 23(2):193–212, 1952. URL http://projecteuclid.org/euclid.aoms/1177729437. (Cited on page 30.)

Anguiano, B. et al. 'The GALAH survey'. *PIAU*, 9(S298):322–325, 2014. URL http://adsabs.harvard.edu/abs/2014IAUS..298..322A. (Cited on pages xvi and 19.)

Arenou, F. 'Simulating multiple stars in preparation for Gaia'. In J. A. Docobo, V. S. Tamazian and Y. Y. Balega, editors, 'AIP Conf. Proc.', volume 1346 of *American Institute of Physics Conference Series*, pages 107–121 (2011). URL http://adsabs.harvard.edu/abs/2011AIPC.1346..107A. (Cited on page 61.)

Arenou, F. et al. 'Zero-point and external errors of HIPPARCOS parallaxes'. *A&A*, 1995. URL http://adsabs.harvard.edu/abs/1995A%26A...304...52A. (Cited on page 24.)

Argast, D. et al. 'Metal-poor halo stars as tracers of ISM mixing processes during halo formation'. *A&A*, 2000. URL http://adsabs.harvard.edu/abs/2000A%26A...356..873A. (Cited on pages 69 and 73.)

Askey, R. *Book Review: The lost notebook and other unpublished papers*, volume 19 (Narosa Pub. House, New Delhi, 1988). URL http://www.ams.org/journal-getitem?pii=S0273-0979-1988-15741-2. (Cited on page 50.)

Asplund, M. et al. 'The Chemical Composition of the Sun'. *ARA&A*, 47(1):481–522, 2009. URL http://adsabs.harvard.edu/abs/2009ARA%26A..47..481A. (Cited on page 70.)

Aumer, M. and Binney, J. J. 'Kinematics and history of the solar neighbourhood revisited'. *MNRAS*, 397(3):1286–1301, 2009. URL http://mnras.oxfordjournals.org/cgi/doi/10.1111/j.1365-2966.2009.15053.x. (Cited on pages 16, 41, and 48.)

Baade, W. 'The Resolution of Messier 32, NGC 205, and the Central Region of the Andromeda Nebula.' *ApJ*, 100:137, 1944. URL http://adsabs.harvard.edu/abs/1944ApJ...100..137B. (Cited on page 10.)

Baade, W. 'A Search For the Nucleus of Our Galaxy'. *PASP*, 58:249, 1946. URL http://adsabs.harvard.edu/abs/1946PASP...58..249B. (Cited on page 15.)

Baglin, A. and COROT Team. 'Asteroseismology from space - The COROT experiment'. *IAUS*, 185:301, 1998. URL http://adsabs.harvard.edu/abs/1998IAUS..185..301B. (Cited on pages xvi and 20.)

Bailer-Jones, C. a. L. 'Estimating distances from parallaxes'. *PASP, in Press*, 2015. URL http://arxiv.org/abs/1507.02105. (Cited on pages vii, 23, 24, and 27.)

Balick, B. and Brown, R. L. 'Intense sub-arcsecond structure in the galactic center'. *ApJ*, 194:265, 1974. URL http://adsabs.harvard.edu/abs/1974ApJ...194..265B. (Cited on page 15.)

Bell, E. F. et al. 'The Accretion Origin of the Milky Way's Stellar Halo'. *ApJ*, 680(1):295–311, 2008. URL http://adsabs.harvard.edu/abs/2008ApJ...680..295B. (Cited on page 14.)

Bensby, T., Feltzing, S. and Oey, M. S. 'Exploring the Milky Way stellar disk'. *A&A*, 562:A71, 2014. URL http://adsabs.harvard.edu/abs/2014A%26A...562A..71B. (Cited on page 93.)

Bensby, T. et al. 'A first constraint on the thick disc scale length: differential radial abundances in K-giants at Galactocentric radii 4, 8, and 12 kpc'. *ApJ*, 735(2):L46, 2011. URL http://adsabs.harvard.edu/abs/2011ApJ...735L..46B. (Cited on page 17.)

Bergemann, M. et al. 'The Gaia-ESO Survey: radial metallicity gradients and age-metallicity relation of stars in the Milky Way disk'. *A&A*, 565:A89, 2014. URL http://adsabs.harvard.edu/abs/2014A&A...565A..89Bhttp://www.aanda.org/10.1051/0004-6361/201423456. (Cited on page 84.)

Bethe, H. a. 'Energy Procution in Stars'. *PhR*, 55(1):434–456, 1939. (Cited on page 7.)

Binney, J. and Tremaine, S. *Galactic Dynamics: Second Edition* (Princeton University Press, 2008). URL http://adsabs.harvard.edu/abs/2008gady.book.....B. (Cited on page 14.)

Blitz, L. and Spergel, D. N. 'Direct evidence for a bar at the Galactic center'. *ApJ*, 379:631, 1991. URL http://adsabs.harvard.edu/abs/1991ApJ...379..631B. (Cited on page 16.)

Borde, A. et al. 'New approach for precise computation of Lyman-α forest power spectrum with hydrodynamical simulations'. *JCAP*, 2014(07):005–005, 2014. URL http://adsabs.harvard.edu/abs/2014JCAP...07..005B. (Cited on page 6.)

Borucki, W. J. et al. 'The Kepler Mission: A Mission To Detennine The Frequency Of Inner Planets Near The Habitable Zone For A Wide Range Of Stars'. In 'ASPC', volume 119, page 153 (1997). URL http://adsabs.harvard.edu/abs/1997ASPC..119..153B. (Cited on pages xvi and 20.)

Bovy, J. et al. 'The spatial structure of mono-abundance sub-populations of the Milky Way disk'. *ApJ*, 753(2):148, 2012. URL http://adsabs.harvard.edu/abs/2012ApJ...753..148B. (Cited on page 17.)

Bovy, J. et al. 'The APOGEE red-clump catalogue: Precise distances, velocities, and high-resolution elemental abundances over a large area of the Milky Way's disk'. *ApJ*, 790(2):127, 2014. URL http://stacks.iop.org/0004-637X/790/i=2/a=127?key=crossref.28bb7efb839c0e6cbace4f8460eaca66. (Cited on page 76.)

Boylan-Kolchin, M. et al. 'Resolving cosmic structure formation with the Millennium-II Simulation'. *MNRAS*, 398(3):1150–1164, 2009. URL http://adsabs.harvard.edu/abs/2009MNRAS.398.1150B. (Cited on page 18.)

Bressan, A. et al. 'PARSEC: stellar tracks and isochrones with the PAdova and TRieste Stellar Evolution Code'. *MNRAS*, 427(1):127–145, 2012. URL http://mnras.oxfordjournals.org/cgi/doi/10.1111/j.1365-2966.2012.21948.x. (Cited on pages 10, 45, 60, and 76.)

Burbidge, E. M. et al. 'Synthesis of the Elements in Stars'. *RvMP*, 29(4):547–650, 1957. URL http://adsabs.harvard.edu/abs/1957RvMP...29..547B. (Cited on page 7.)

Carollo, D. et al. 'Two stellar components in the halo of the Milky Way.' *Nature*, 450(7172):1020–5, 2007. URL http://adsabs.harvard.edu/abs/2007Natur.450.1020C. (Cited on page 15.)

Chabrier, G. 'Galactic Stellar and Substellar Initial Mass Function'. *PASP*, 115(809):763–795, 2003. URL http://adsabs.harvard.edu/abs/2003PASP..115..763C. (Cited on pages xv, 41, 56, 62, and 70.)

Chandrasekhar, S. 'The Maximum Mass of Ideal White Dwarfs'. *ApJ*, 74:81, 1931. URL http://adsabs.harvard.edu/abs/1931ApJ....74...81C. (Cited on page 11.)

Chen, Y. et al. 'Improving PARSEC models for very low mass stars'. *MNRAS*, 444(3):2525–2543, 2014. URL http://mnras.oxfordjournals.org/cgi/doi/10.1093/mnras/stu1605. (Cited on pages 45 and 60.)

Chiappini, C., Matteucci, F. and Gratton, R. 'The Chemical Evolution of the Galaxy: The Two-Infall Model'. *ApJ*, 477(2):765–780, 1997. URL http://adsabs.harvard.edu/abs/1997ApJ...477..765C. (Cited on pages 19, 41, and 71.)

Chiappini, C. et al. 'Imprints of fast-rotating massive stars in the Galactic Bulge.' *Nature*, 472(7344):454–7, 2011. URL http://adsabs.harvard.edu/abs/2011Natur.472..454C. (Cited on page 8.)

Chiappini, C. et al. 'Young [α /Fe]-enhanced stars discovered by CoRoT and APOGEE: What is their origin?' *A&A*, 576:L12, 2015. URL http://adsabs.harvard.edu/abs/2015A%26A...576L..12C. (Cited on page 84.)

Chieffi, A. and Limongi, M. 'Explosive Yields of Massive Stars from Z = 0 to Z = Z $\odot$'. *ApJ*, 608(1):405–410, 2004. URL http://adsabs.harvard.edu/abs/2004ApJ...608..405C. (Cited on page 71.)

Churchwell, E. et al. 'The Spitzer /GLIMPSE Surveys: A New View of the Milky Way'. *PASP*, 121(877):213–230, 2009. URL http://adsabs.harvard.edu/abs/2009PASP..121..213C. (Cited on page 17.)

Curtis, H. D. 'Novae in the Spiral Nebulae and the Island Universe Theory'. *PASP*, 29:206, 1917. URL http://adsabs.harvard.edu/abs/1917PASP...29..206C. (Cited on page 4.)

Czekaj, M. A. et al. 'The Besançon Galaxy model renewed'. *A&A*, 564:A102, 2014. URL http://adsabs.harvard.edu/abs/2014A%26A...564A.102C. (Cited on pages xv, 41, 42, 45, 47, 55, 59, 61, and 63.)

Davis, M. et al. 'The evolution of large-scale structure in a universe dominated by cold dark matter'. *ApJ*, 292:371, 1985. URL http://adsabs.harvard.edu/abs/1985ApJ...292..371D. (Cited on page 5.)

Davis, T. M. and Lineweaver, C. H. 'Expanding Confusion: Common Misconceptions of Cosmological Horizons and the Superluminal Expansion of the Universe'. *PASA*, 21(01):97–109, 2004. URL http://adsabs.harvard.edu/abs/2004PASA...21...97Dhttp://www.journals.cambridge.org/abstract_S132335800000607X. (Cited on page 5.)

de Bruijne, J. H. J. 'Science performance of Gaia, ESA's space-astrometry mission'. *Ap&SS*, 341(1):31–41, 2012. URL http://adsabs.harvard.edu/abs/2012Ap%26SS.341...31D. (Cited on page 24.)

Dehnen, W. 'The Effect of the Outer Lindblad Resonance of the Galactic Bar on the Local Stellar Velocity Distribution'. *AJ*, 119(2):800–812, 2000. URL http://adsabs.harvard.edu/abs/2000AJ....119..800D. (Cited on page 16.)

Dib, S. 'Testing the universality of the IMF with Bayesian statistics: young clusters'. *MNRAS*, 444(2):1957–1981, 2014. URL http://adsabs.harvard.edu/abs/2014MNRAS.444.1957D. (Cited on page 41.)

Dicke, R. H. et al. 'Cosmic Black-Body Radiation.' *ApJ*, 142:414, 1965. URL http://adsabs.harvard.edu/abs/1965ApJ...142..414D. (Cited on page 5.)

Dommanget, J. and Nys, O. 'Catalog of Components of Double & Multiple stars'. *VizieR Online Data Cat.*, 1274:0, 2002. URL http://adsabs.harvard.edu/abs/2002yCat.1274....0D. (Cited on page 61.)

Dressler, A. 'Galaxy morphology in rich clusters - Implications for the formation and evolution of galaxies'. *ApJ*, 236:351, 1980. URL http://adsabs.harvard.edu/abs/1980ApJ...236..351D. (Cited on page 6.)

Eggen, O. J., Lynden-Bell, D. and Sandage, A. R. 'Evidence from the motions of old stars that the Galaxy collapsed.' *ApJ*, 136:748, 1962. URL http://adsabs.harvard.edu/abs/1962ApJ...136..748E. (Cited on page 18.)

Einstein, A. 'Die Feldgleichungen der Gravitation'. *Sitzungsberichte d. Königlich Preuß. Akad. d. Wissenschaften*, 1915. URL http://adsabs.harvard.edu/abs/1915SPAW.....844E. (Cited on page 4.)

Einstein, A. 'Kosmologische Betrachtungen zur allgemeinen Relativitätstheorie'. *Sitzungsberichte d. Königlich Preuß. Akad. d. Wissenschaften*, 1917. URL http://adsabs.harvard.edu/abs/1917SPAW.....142E. (Cited on page 5.)

Eisenstein, D. J. et al. 'Detection of the Baryon Acoustic Peak in the Large-Scale Correlation Function of SDSS Luminous Red Galaxies'. *ApJ*, 633(2):560–574, 2005. URL http://arxiv.org/abs/astro-ph/0501171http://stacks.iop.org/0004-637X/633/i=2/a=560http://adsabs.harvard.edu/abs/2005ApJ...633..560E. (Cited on page 6.)

ESA. 'The HIPPARCOS and TYCHO catalogues. Astrometric and photometric star catalogues derived from the ESA HIPPARCOS Space Astrometry Mission'. In 'ESA SP Ser. vol no 1200', (1997). URL http://adsabs.harvard.edu/abs/1997ESASP1200.....E. (Cited on page 47.)

Famaey, B. and McGaugh, S. S. 'Modified Newtonian Dynamics (MOND): Observational Phenomenology and Relativistic Extensions'. *Living Rev. Relativ.*, 15, 2012. URL http://adsabs.harvard.edu/abs/2012LRR....15...10F. (Cited on page 6.)

Fioc, M. and Rocca-Volmerange, B. 'PEGASE: a UV to NIR spectral evolution model of galaxies. Application to the calibration of bright galaxy counts.' *A&A*, 1997. URL http://adsabs.harvard.edu/abs/1997A%26A...326..950F. (Cited on page 45.)

Flynn, C. et al. 'On the mass-to-light ratio of the local Galactic disc and the optical luminosity of the Galaxy'. *MNRAS*, 372(3):1149–1160, 2006. URL http://mnras.oxfordjournals.org/cgi/doi/10.1111/j.1365-2966.2006.10911.x. (Cited on pages xvi and 58.)

Foreman-Mackey, D. et al. 'emcee : The MCMC Hammer'. *PASP*, 125(925):306–312, 2013. URL http://adsabs.harvard.edu/abs/2013PASP..125..306F. (Cited on pages 50 and 82.)

Francis, C. 'Calibration of RAVE distances to a large sample of Hipparcos stars'. *MNRAS*, 436(2):1343–1361, 2013. URL http://mnras.oxfordjournals.org/cgi/doi/10.1093/mnras/stt1651. (Cited on pages 26 and 48.)

Francois, P. et al. 'The evolution of the Milky Way from its earliest phases: Constraints on stellar nucleosynthesis'. *A&A*, 421(2):613–621, 2004. URL http://adsabs.harvard.edu/abs/2004A%26A...421..613F. (Cited on pages 71 and 87.)

Frebel, A. et al. 'Nucleosynthetic signatures of the first stars.' *Nature*, 434(7035):871–3, 2005. URL http://adsabs.harvard.edu/abs/2005Natur.434..871F. (Cited on page 8.)

Freedman, W. L. et al. 'Final Results from the Hubble Space Telescope Key Project to Measure the Hubble Constant'. *ApJ*, 553(1):47–72, 2001. URL http://adsabs.harvard.edu/abs/2001ApJ...553...47F. (Cited on page 6.)

Friedman, A. 'Ueber die Kruemmung des Raumes'. *Zeitschrift fuer Phys.*, 10(1):377–386, 1922. URL http://adsabs.harvard.edu/abs/1922ZPhy...10..377F. (Cited on page 4.)

Fuhrmann, K. 'Nearby stars of the Galactic disk and halo'. *A&A*, 1998. URL http://adsabs.harvard.edu/abs/1998A%26A...338..161F. (Cited on page 17.)

Gamow, G. 'Expanding Universe and the Origin of Elements'. *PhR*, 70(7-8):572–573, 1946. URL http://adsabs.harvard.edu/abs/1946PhRv...70..572G. (Cited on page 7.)

Genel, S. et al. 'Introducing the Illustris project: the evolution of galaxy populations across cosmic time'. *MNRAS*, 445(1):175–200, 2014. URL http://adsabs.harvard.edu/abs/2014MNRAS.445..175G. (Cited on page 19.)

Gerhard, O. 'Pattern speeds in the Milky Way.' *MmSAIS*, 2011. URL http://adsabs.harvard.edu/abs/2011MSAIS..18..185G. (Cited on page 16.)

Gillessen, S. et al. 'Monitoring stellar orbits around the massive black hole in the Galactic center'. *ApJ*, 692(2):1075–1109, 2009. URL http://adsabs.harvard.edu/abs/2009ApJ...692.1075G. (Cited on page 15.)

Gilmore, G. and Reid, N. 'New light on faint stars. III - Galactic structure towards the South Pole and the Galactic thick disc'. *MNRAS*, 202:1025–1047, 1983. URL http://adsabs.harvard.edu/abs/1983MNRAS.202.1025G. (Cited on page 16.)

Gilmore, G. et al. 'The Gaia-ESO Public Spectroscopic Survey'. *The Messenger*, 147(March):25, 2012. URL http://adsabs.harvard.edu/cgi-bin/nph-data_query?bibcode=2012Msngr.147...25G&link_type=ABSTRACT$\delimiter"026E30F$npapers://ada43e77-f677-4abf-a73e-6493805a76d2/Paper/p31557. (Cited on pages xvi, 19, 89, and 93.)

Golubov, O. et al. 'The asymmetric drift, the local standard of rest, and implications from RAVE data'. *A&A*, 557:A92, 2013. URL http://adsabs.harvard.edu/abs/2013A%26A...557A..92G. (Cited on page 16.)

Goodman, J. and Weare, J. 'Ensemble samplers with affine invariance'. *Commun. Appl. Math. Comput. Sci.*, 5(1):65–80, 2010. URL http://msp.org/camcos/2010/5-1/p04.xhtmlhttp://www.revista.ufpe.br/gestaoorg/index.php/gestao/article/view/460. (Cited on pages 50 and 82.)

Gratton, R. et al. 'The [Fe/O] Ratio in Field Stars and the History of Star Formation of the Solar Neighbourhood'. *ASPC*, 92:307, 1996. URL http://adsabs.harvard.edu/abs/1996ASPC...92..307G. (Cited on page 17.)

Green, G. M. et al. 'A Three-Dimensional Map of Milky-Way Dust'. *eprint arXiv:1507.01005*, 2015. URL http://adsabs.harvard.edu/abs/2015arXiv150701005G. (Cited on pages 36 and 48.)

Guedes, J. et al. 'Forming realistic late-type spirals in a ΛCDM Universe: the Eris simulation'. *ApJ*, 742(2):76, 2011. URL http://adsabs.harvard.edu/abs/2011ApJ...742...76G. (Cited on page 19.)

Guth, A. H. 'Inflationary universe: A possible solution to the horizon and flatness problems'. *PhRvD*, 23(2):347–356, 1981. URL http://adsabs.harvard.edu/abs/1981PhRvD..23..347G. (Cited on page 5.)

Hammersley, P. L. et al. 'Detection of the old stellar component of the major Galactic bar'. *MNRAS*, 317(3):L45–L49, 2000. URL http://adsabs.harvard.edu/abs/2000MNRAS.317L..45H. (Cited on page 16.)

Hawkins, K. et al. 'Using chemical tagging to redefine the interface of the Galactic disc and halo'. *MNRAS*, 453(1):758–774, 2015. URL http://adsabs.harvard.edu/abs/2015MNRAS.453..758H. (Cited on pages 80 and 93.)

Hayashi, C. 'Proton-Neutron Concentration Ratio in the Expanding Universe at the Stages preceding the Formation of the Elements'. *Prog. Theor. Phys.*, 5:224–235, 1950. URL http://adsabs.harvard.edu/abs/1950PThPh...5..224H. (Cited on page 7.)

Haywood, M., Robin, A. C. and Crézé, M. 'The evolution of the Milky Way disc. I. Vertical structure and local constraints.' *A&A*, 320:428, 1997. URL http://adsabs.harvard.edu/abs/1997A&A...320..428H. (Cited on page 41.)

Hodapp, K. W. et al. 'Design of the Pan-STARRS telescopes'. *AN*, 325(6-8):636–642, 2004. URL http://adsabs.harvard.edu/abs/2004AN....325..636H. (Cited on page xvii.)

Hoeg, E. et al. 'The Tycho-2 catalogue of the 2.5 million brightest stars'. *A&A*, 355:L27, 2000. URL http://adsabs.harvard.edu/abs/2000A%26A...355L..27H. (Cited on pages xvii and 42.)

Holberg, J. B. et al. 'a New Look At the Local White Dwarf Population'. *AJ*, 135(4):1225–1238, 2008. URL http://stacks.iop.org/1538-3881/135/i=4/a=1225?key=crossref.1adc3bf1c110d8ec1ffb638cc81327e9. (Cited on pages 57 and 58.)

Holmberg, J. and Flynn, C. 'The local density of matter mapped by Hipparcos'. *MNRAS*, 313(2):209–216, 2000. URL http://adsabs.harvard.edu/abs/2000MNRAS.313..209H. (Cited on page 59.)

Holmberg, J., Flynn, C. and Lindegren, L. 'Towards an Improved Model of the Galaxy'. In 'ESA SP-402', pages 721–726 (1997). URL http://adsabs.harvard.edu/abs/1997ESASP.402..721H. (Cited on page 58.)

Holtzman, J. A. et al. 'Abundances, Stellar Parameters, and Spectra From the SDSS-III/APOGEE Survey'. *eprint arXiv:1501.04110*, 2015. URL http://adsabs.harvard.edu/abs/2015arXiv150104110H. (Cited on page 80.)

Hoyle, F. and Fowler, W. A. 'Nucleosynthesis in Supernovae.' *ApJ*, 132:565, 1960. URL http://adsabs.harvard.edu/abs/1960ApJ...132..565H. (Cited on page 11.)

Hubble, E. 'A relation between distance and radial velocity among extra-galactic nebulae'. *PNAS*, 15(3):168–173, 1929. URL http://adsabs.harvard.edu/abs/1929PNAS...15..168H. (Cited on page 5.)

Hubble, E. P. 'Cepheids in spiral nebulae'. *Obs.*, 48:139–142, 1925. URL http://adsabs.harvard.edu/abs/1925Obs....48..139H. (Cited on page 4.)

Ibata, R., Mouhcine, M. and Rejkuba, M. 'An HST /ACS investigation of the spatial and chemical structure and sub-structure of NGC 891, a Milky Way analogue'. *MNRAS*, 395(1):126–143, 2009. URL http://adsabs.harvard.edu/abs/2009MNRAS.395..126I. (Cited on page 17.)

Iwamoto, K. et al. 'Nucleosynthesis in Chandrasekhar Mass Models for Type Ia Supernovae and Constraints on Progenitor Systems and Burning-Front Propagation'. *ApJS*, 125(2):439–462, 1999. URL http://adsabs.harvard.edu/abs/1999ApJS..125..439I. (Cited on pages 12 and 72.)

Jahreiss, H. and Wielen, R. 'The impact of HIPPARCOS on the Catalogue of Nearby Stars. The stellar luminosity function and local kinematics'. *HIPPARCOS '97*, pages 675–680, 1997. URL http://adsabs.harvard.edu/abs/1997ESASP.402..675J. (Cited on pages xvi, 32, 42, 45, 57, 58, 59, and 61.)

Jeans, J. H. 'The Stability of a Spherical Nebula'. *Philos. Trans. R. Soc. A Math. Phys. Eng. Sci.*, 199(312-320):1–53, 1902. URL http://adsabs.harvard.edu/abs/1902RSPTA.199....1J. (Cited on page 8.)

Jurić, M. et al. 'The Milky Way Tomography with SDSS. I. Stellar Number Density Distribution'. *ApJ*, 673(2):864–914, 2008. URL http://adsabs.harvard.edu/abs/2008ApJ...673..864J. (Cited on page 17.)

Just, A., Gao, S. and Vidrih, S. 'Towards a fully consistent Milky Way disc model - II. The local disc model and SDSS data of the NGP region'. *MNRAS*, 411(4):2586–2595, 2011. URL http://mnras.oxfordjournals.org/cgi/doi/10.1111/j.1365-2966.2010.17866.x. (Cited on pages xvii and 41.)

Just, A. and Jahreiss, H. 'Towards a fully consistent Milky Way disc model - I. The local model based on kinematic and photometric data'. *MNRAS*, 402(1):461–478, 2010. URL http://mnras.oxfordjournals.org/cgi/doi/10.1111/j.1365-2966.2009.15893.x. (Cited on pages v, xvi, xvii, 19, 32, 33, 41, 42, and 91.)

Just, A. and Rybizki, J. 'Dynamical and chemical evolution of the thin disc'. In C. Chiappini, J. Montalban and M. Steffen, editors, 'Heraeus 592 - AN, to be Publ.', page submitted (2015). (Cited on pages vii and 76.)

Just, A. et al. 'The local stellar luminosity function and mass-to-light ratio in the near-infrared'. *MNRAS*, 451(1):149–158, 2015. URL http://adsabs.harvard.edu/abs/2015MNRAS.451.4668J. (Cited on pages vii, 35, 47, 57, 58, 59, 64, 65, and 91.)

Kafle, P. R. et al. 'On the shoulders of giants: properties of the stellar halo and the Milky Way mass distribution'. *ApJ*, 794(1):59, 2014. URL http://adsabs.harvard.edu/abs/2014ApJ...794...59K. (Cited on pages 15 and 16.)

Karakas, A. I. 'Updated stellar yields from asymptotic giant branch models'. *MNRAS*, 403(3):1413–1425, 2010. URL http://adsabs.harvard.edu/abs/2010MNRAS.403.1413K. (Cited on pages 69 and 72.)

Keller, S. C. et al. 'A single low-energy, iron-poor supernova as the source of metals in the star SMSS J031300.36-670839.3.' *Nature*, 506(7489):463–6, 2014. URL http://adsabs.harvard.edu/abs/2014Natur.506..463K. (Cited on page 8.)

Kirkman, D. et al. 'The Cosmological Baryon Density from the Deuterium-to-Hydrogen Ratio in QSO Absorption Systems: D/H toward Q1243+3047'. *ApJS*, 149(1):1–28, 2003. URL http://adsabs.harvard.edu/abs/2003ApJS..149....1K. (Cited on page 7.)

Klypin, A. et al. 'Where Are the Missing Galactic Satellites?' *ApJ*, 522(1):82–92, 1999. URL http://adsabs.harvard.edu/abs/1999ApJ...522...82K. (Cited on page 6.)

Kobayashi, C., Karakas, A. I. and Umeda, H. 'The evolution of isotope ratios in the Milky Way Galaxy'. *MNRAS*, 414(4):3231–3250, 2011. URL http://adsabs.harvard.edu/abs/2011MNRAS.414.3231K. (Cited on page 73.)

Kroupa, P. 'The Dark Matter Crisis: Falsification of the Current Standard Model of Cosmology'. *PASA*, 29(04):395–433, 2012. URL http://adsabs.harvard.edu/abs/2012PASA...29..395Khttp://www.journals.cambridge.org/abstract_S1323358000001417. (Cited on page 6.)

Kroupa, P., Tout, C. A. and Gilmore, G. 'The distribution of low-mass stars in the Galactic disc'. *MNRAS*, 262:545–587, 1993. URL http://adsabs.harvard.edu/abs/1993MNRAS.262..545K. (Cited on pages xvi, 41, 55, and 70.)

Kubryk, M., Prantzos, N. and Athanassoula, E. 'Evolution of the Milky Way with radial motions of stars and gas'. *A&A*, 580:A126, 2015. URL http://adsabs.harvard.edu/abs/2015A%26A...580A.126K. (Cited on pages 75, 80, 84, and 88.)

Lallement, R. et al. '3D maps of the local ISM from inversion of individual color excess measurements'. *A&A*, 561:A91, 2014. URL http://www.aanda.org/10.1051/0004-6361/201322032. (Cited on pages 36 and 47.)

Larson, R. B. 'The Formation of the First Stars'. *ESA SP*, 445:13, 2000. URL http://adsabs.harvard.edu/abs/2000ESASP.445...13L. (Cited on page 8.)

Leavitt, H. S. '1777 variables in the Magellanic Clouds'. *AnHar*, 60, 1908. URL http://adsabs.harvard.edu/abs/1908AnHar..60...87L. (Cited on page 3.)

Lee, O. J. 'On a reason for the appearance of negative parallaxes in the determination of the distances of stars.' *AnDea*, 4, 1943. URL http://adsabs.harvard.edu/abs/1943AnDea...4....1L. (Cited on page 24.)

Lemaître, G. 'Un Univers homogène de masse constante et de rayon croissant rendant compte de la vitesse radiale des nébuleuses extra-galactiques'. *Ann. la Société Sci. Bruxelles*, pages 49–59, 1927. URL http://adsabs.harvard.edu/abs/1927ASSB...47...49L. (Cited on page 4.)

Lemaître, G. 'The Beginning of the World from the Point of View of Quantum Theory.' *Nature*, 127(3210):706–706, 1931. URL http://adsabs.harvard.edu/abs/1931Natur.127..706L. (Cited on page 5.)

Lindblad, B. 'On the state of motion in the galactic system'. *MNRAS*, 87, 1927. URL http://adsabs.harvard.edu/abs/1927MNRAS..87..553L. (Cited on page 16.)

Linde, A. 'Coleman-Weinberg theory and the new inflationary universe scenario'. *Phys. Lett. B*, 114(6):431–435, 1982. URL http://linkinghub.elsevier.com/retrieve/pii/0370269382900867. (Cited on page 5.)

Linde, A. 'Chaotic inflation'. *Phys. Lett. B*, 129(3-4):177–181, 1983. URL http://adsabs.harvard.edu/abs/1983PhLB..129..177L. (Cited on page 5.)

Lindegren, L. et al. 'Double star data in the HIPPARCOS Catalogue'. *A&A*, 323:L53–L56, 1997. URL http://adsabs.harvard.edu/abs/1997A&A...323L..53L. (Cited on page 61.)

Lindegren, L. et al. 'The Gaia mission: science, organization and present status'. *PIAU*, 3(S248):217–223, 2008. URL http://adsabs.harvard.edu/abs/2008IAUS..248..217L. (Cited on pages xvi, 19, 24, 63, and 93.)

Livio, M. 'Lost in translation: Mystery of the missing text solved.' *Nature*, 479(7372):171–3, 2011. URL http://adsabs.harvard.edu/abs/2011Natur.479..171L. (Cited on page 5.)

Lodders, K., Palme, H. and Gail, H.-P. *Solar System*, volume 4B of *Landolt-Börnstein - Group VI Astronomy and Astrophysics* (Springer Berlin Heidelberg, Berlin, Heidelberg, 2009). URL http://adsabs.harvard.edu/abs/2009LanB...4B...44Lhttp://materials.springer.com/bp/docs/978-3-540-88055-4. (Cited on pages 12 and 70.)

Luri, X. et al. 'Overview and stellar statistics of the expected Gaia Catalogue using the Gaia Object Generator'. *A&A*, 566:A119, 2014. URL http://www.aanda.org/10.1051/0004-6361/201423636. (Cited on page 24.)

Ly, C. et al. 'The Luminosity Function and Star Formation Rate between Redshifts of 0.07 and 1.47 for Narrowband Emitters in the Subaru Deep Field'. *ApJ*, 657(2):738–759, 2007. URL http://adsabs.harvard.edu/abs/2007ApJ...657..738L. (Cited on page 41.)

Mandelbaum, R. et al. 'Cosmological parameter constraints from galaxy-galaxy lensing and galaxy clustering with the SDSS DR7'. *MNRAS*, 432(2):1544–1575, 2013. URL http://adsabs.harvard.edu/abs/2013MNRAS.432.1544M. (Cited on page 6.)

Mannucci, F. et al. 'The supernova rate per unit mass'. *A&A*, 433(3):807–814, 2005. URL http://adsabs.harvard.edu/abs/2005A%26A...433..807M. (Cited on page 80.)

Maoz, D., Mannucci, F. and Brandt, T. D. 'The delay-time distribution of Type Ia supernovae from Sloan II'. *MNRAS*, 426(4):3282–3294, 2012. URL http://adsabs.harvard.edu/abs/2012MNRAS.426.3282M. (Cited on pages 72 and 73.)

Maoz, D. and Sharon, K. 'The supernova delay time distribution in galaxy clusters and implications for type-Ia progenitors and metal enrichment'. *ApJ*, 722(2):1879–1894, 2010. URL http://adsabs.harvard.edu/abs/2010ApJ...722.1879M. (Cited on pages 72 and 73.)

Marigo, P. et al. 'Evolution of asymptotic giant branch stars'. *A&A*, 482(3):883–905, 2008. URL http://adsabs.harvard.edu/abs/2008A%26A...482..883M. (Cited on pages 45 and 60.)

Marshall, D. J. et al. 'Modelling the Galactic interstellar extinction distribution in three dimensions'. *A&A*, 453(2):635–651, 2006. URL http://www.aanda.org/10.1051/0004-6361:20053842. (Cited on page 36.)

Martig, M. et al. 'A diversity of progenitors and histories for isolated spiral galaxies'. *ApJ*, 756(1):26, 2012. URL http://adsabs.harvard.edu/abs/2012ApJ...756...26M. (Cited on page 19.)

Mason, B. D. et al. 'The 2001 US Naval Observatory Double Star CD-ROM. I. The Washington Double Star Catalog'. *AJ*, 122(6):3466–3471, 2001. URL http://stacks.iop.org/1538-3881/122/i=6/a=3482http://stacks.iop.org/1538-3881/122/i=6/a=3466. (Cited on page 61.)

Matteucci, F. *Chemical Evolution of Galaxies*. Astronomy and Astrophysics Library (Springer Berlin Heidelberg, Berlin, Heidelberg, 2012). URL http://adsabs.harvard.edu/abs/2012ceg..book.....M. (Cited on page 67.)

May, J. et al. 'A deep CO survey of the third galactic quadrant'. *A&AS*, 99:105–165, 1993. URL http://adsabs.harvard.edu/abs/1993A%26AS...99..105M. (Cited on page 16.)

McMillan, P. J. 'Mass models of the Milky Way'. *MNRAS*, 414(3):2446–2457, 2011. URL http://adsabs.harvard.edu/abs/2011MNRAS.414.2446M. (Cited on page 14.)

Miller, G. E. and Scalo, J. M. 'The initial mass function and stellar birthrate in the solar neighborhood'. *ApJS*, 41:513, 1979. URL http://adsabs.harvard.edu/abs/1979ApJS...41..513M. (Cited on page 41.)

Minchev, I., Chiappini, C. and Martig, M. 'Chemodynamical evolution of the Milky Way disk'. *A&A*, 558:A9, 2013. URL http://adsabs.harvard.edu/abs/2013A%26A...558A...9M. (Cited on pages 17, 19, and 75.)

Mollá, M. et al. 'Galactic chemical evolution: stellar yields and the initial mass function'. *MNRAS*, 451(4):3693–3708, 2015. URL http://adsabs.harvard.edu/abs/2015MNRAS.451.3693M. (Cited on page 88.)

Momany, Y. et al. 'Outer structure of the Galactic warp and flare: explaining the Canis Major over-density'. *A&A*, 451(2):515–538, 2006. URL http://adsabs.harvard.edu/abs/2006A%26A...451..515M. (Cited on page 16.)

Mortlock, D. J. et al. 'A luminous quasar at a redshift of z = 7.085.' *Nature*, 474(7353):616–9, 2011. URL http://adsabs.harvard.edu/abs/2011Natur.474..616M. (Cited on page 8.)

Nieva, M.-F. and Przybilla, N. 'Present-day cosmic abundances'. *A&A*, 539:A143, 2012. (Cited on page 75.)

Nomoto, K., Kobayashi, C. and Tominaga, N. 'Nucleosynthesis in Stars and the Chemical Enrichment of Galaxies'. *ARA&A*, 51(1):457–509, 2013. URL http://adsabs.harvard.edu/abs/2013ARA%26A..51..457N. (Cited on pages 69, 71, 73, 87, and 88.)

Nomoto, K., Thielemann, F.-K. and Yokoi, K. 'Accreting white dwarf models of Type I supernovae. III - Carbon deflagration supernovae'. *ApJ*, 286:644, 1984. URL http://adsabs.harvard.edu/abs/1984ApJ...286..644N. (Cited on page 12.)

Nordström, B. et al. 'The Geneva-Copenhagen survey of the Solar neighbourhood'. *A&A*, 418(3):989–1019, 2004. URL http://adsabs.harvard.edu/abs/2004A%26A...418..989N. (Cited on pages xvi, 19, and 44.)

Oort, J. H. 'The Stars of High Velocity'. *PGro*, 40, 1926. URL http://adsabs.harvard.edu/abs/1926PhDT.....1O. (Cited on page 16.)

Oort, J. H. 'Observational evidence confirming Lindblad's hypothesis of a rotation of the galactic system'. *BAN*, 3, 1927. URL http://adsabs.harvard.edu/abs/1927BAN.....3..275O. (Cited on page 16.)

Oort, J. H. 'Dynamics of the galactic system in the vicinity of the Sun'. *BAN*, 4, 1928. URL http://adsabs.harvard.edu/abs/1928BAN.....4..269O. (Cited on page 16.)

Pagel, B. E. J. *Nucleosynthesis and Chemical Evolution of Galaxies* (CUP, 2009). URL http://adsabs.harvard.edu/abs/2009nceg.book.....P. (Cited on page 14.)

Parravano, A., McKee, C. F. and Hollenbach, D. J. 'An initial mass function for individual stars in Galactic disks. I. Constraining the shape of the initial mass function'. *ApJ*, 726(1):27, 2011. URL http://adsabs.harvard.edu/abs/2011ApJ...726...27P. (Cited on pages 41 and 62.)

Peebles, P. J. E. 'Large-scale background temperature and mass fluctuations due to scale-invariant primeval perturbations'. *ApJ*, 263:L1, 1982. URL http://adsabs.harvard.edu/abs/1982ApJ...263L...1P. (Cited on page 5.)

Peebles, P. J. E. and Yu, J. T. 'Primeval Adiabatic Perturbation in an Expanding Universe'. *ApJ*, 162:815, 1970. URL http://adsabs.harvard.edu/abs/1970ApJ...162..815P. (Cited on page 5.)

Penzias, A. A. and Wilson, R. W. 'A Measurement of Excess Antenna Temperature at 4080 Mc/s.' *ApJ*, 142:419, 1965. URL http://adsabs.harvard.edu/abs/1965ApJ...142..419P. (Cited on page 5.)

Perlmutter, S. et al. 'Measurements of Omega and Lambda from 42 High-Redshift Supernovae'. *ApJ*, 517(2):21, 1999. URL http://adsabs.harvard.edu/abs/1999ApJ...517..565P. (Cited on page 5.)

Perryman, M. A. C. et al. 'The HIPPARCOS Catalogue'. *A&A*, 1997. URL http://adsabs.harvard.edu/abs/1997A%26A...323L..49P. (Cited on pages v, xvi, 19, 24, 37, 38, 42, and 91.)

Pignatari, M. et al. 'NuGrid stellar data set. I. Stellar yields from H to Bi for stars with metallicities Z = 0.02 and Z = 0.01'. *eprint arXiv:1307.6961*, 2013. URL http://adsabs.harvard.edu/abs/2013arXiv1307.6961P. (Cited on pages 71, 72, 87, and 88.)

Planck Collaboration. 'Planck 2015 results. XIII. Cosmological parameters'. 2015. URL http://arxiv.org/abs/1502.01589. (Cited on pages 6 and 9.)

Putman, M., Peek, J. and Joung, M. 'Gaseous Galaxy Halos'. *ARA&A*, 50(1):491–529, 2012. URL http://adsabs.harvard.edu/abs/2012ARA%26A..50..491P. (Cited on page 15.)

Ragan, S. E., Bergin, E. A. and Gutermuth, R. A. 'Detection of structure in infrared-dark clouds with Spitzer : characterizing star formation in the molecular ring'. *ApJ*, 698(1):324–349, 2009. URL http://adsabs.harvard.edu/abs/2009ApJ...698..324R. (Cited on page 16.)

Raiteri, C. M., Villata, M. and Navarro, J. F. 'Simulations of Galactic chemical evolution. I. O and Fe abundances in a simple collapse model.' *A&A*, 1996. URL http://adsabs.harvard.edu/abs/1996A%26A...315..105R. (Cited on page 73.)

Reid, M. J. et al. 'Trigonometric parallaxes of high mass star forming regions: the structure and kinematics of the Milky Way'. *ApJ*, 783(2):130, 2014. URL http://adsabs.harvard.edu/abs/2014ApJ...783..130R. (Cited on page 16.)

Riess, A. G. et al. 'Observational Evidence from Supernovae for an Accelerating Universe and a Cosmological Constant'. *AJ*, 116(3):1009–1038, 1998. URL http://adsabs.harvard.edu/abs/1998AJ....116.1009R. (Cited on page 5.)

Robertson, H. P. 'On the foundations of relativistic cosmology'. *PNAS*, 15(11):822–829, 1929. URL http://adsabs.harvard.edu/abs/1929PNAS...15..822R. (Cited on page 4.)

Robin, A. C. et al. 'A synthetic view on structure and evolution of the Milky Way'. *A&A*, 409(2):523–540, 2003. URL http://www.edpsciences.org/10.1051/0004-6361:20031117. (Cited on pages xv, 41, and 45.)

Robin, A. C. et al. 'Gaia Universe model snapshot'. *A&A*, 543:A100, 2012. URL http://www.aanda.org/10.1051/0004-6361/201118646. (Cited on pages xv, 45, and 61.)

Robin, A. C. et al. 'Constraining the thick disc formation scenario of the Milky Way'. *A&A*, 569:A13, 2014. URL http://adsabs.harvard.edu/abs/2014A%26A...569A..13R. (Cited on pages xv, 30, and 45.)

Rubin, V. C. and Ford, W. K. 'Rotation of the Andromeda Nebula from a Spectroscopic Survey of Emission Regions'. *ApJ*, 159:379, 1970. URL http://adsabs.harvard.edu/abs/1970ApJ...159..379R. (Cited on page 5.)

Ryan, S. and Norton, A. *Stellar Evolution and Nucleosynthesis* (CUP, 2010). URL http://adsabs.harvard.edu/abs/2010sen..book.....R. (Cited on pages 7, 8, and 10.)

Rybizki, J. and Just, A. 'Towards a fully consistent Milky Way disc model - III. Constraining the initial mass function'. *MNRAS*, 447(4):3880–3891, 2015. URL http://adsabs.harvard.edu/abs/2015MNRAS.447.3880R. (Cited on pages vii, 33, 41, 62, and 72.)

Salpeter, E. E. 'The Luminosity Function and Stellar Evolution.' *ApJ*, 121:161, 1955. URL http://adsabs.harvard.edu/doi/10.1086/145971. (Cited on pages v, vi, 41, and 87.)

Scalo, J. 'The stellar initial mass function'. *FCPh*, 11:1–278, 1986. URL http://adsabs.harvard.edu/abs/1986FCPh...11....1S. (Cited on pages 41 and 45.)

Scheffler, H. and Elsässer, H. *Bau und Physik der Galaxis.* (BI-Wissenschaftsverlag, Mannheim, 1992). URL http://adsabs.harvard.edu/abs/1992bupd.book.....S. (Cited on pages 14, 36, and 48.)

Schlafly, E. F. et al. 'a Large Catalog of Accurate Distances To Molecular Clouds From Ps1 Photometry'. *ApJ*, 786(1):29, 2014. URL http://adsabs.harvard.edu/abs/2014ApJ...786...29S. (Cited on page 47.)

Schlegel, D. J., Finkbeiner, D. P. and Davis, M. 'Maps of Dust Infrared Emission for Use in Estimation of Reddening and Cosmic Microwave Background Radiation Foregrounds'. *ApJ*, 500(2):525–553, 1998. URL http://adsabs.harvard.edu/abs/1998ApJ...500..525S. (Cited on page 36.)

Schmidt, M. 'The Rate of Star Formation.' *ApJ*, 129:243, 1959. URL http://adsabs.harvard.edu/doi/10.1086/146614. (Cited on page 41.)

Schmidt, M. 'The Rate of Star Formation. II. The Rate of Formation of Stars of Different Mass.' *ApJ*, 137:758, 1963. URL http://adsabs.harvard.edu/abs/1963ApJ...137..758S. (Cited on page 69.)

Schönrich, R. and Binney, J. 'Chemical evolution with radial mixing'. *MNRAS*, 396(1):203–222, 2009a. URL http://adsabs.harvard.edu/abs/2009MNRAS.396..203S. (Cited on pages 19 and 75.)

Schönrich, R. and Binney, J. 'Origin and structure of the Galactic disc(s)'. *MNRAS*, 399(3):1145–1156, 2009b. URL http://adsabs.harvard.edu/abs/2009MNRAS.399.1145S. (Cited on page 17.)

Searle, L. and Zinn, R. 'Compositions of halo clusters and the formation of the galactic halo'. *ApJ*, 225:357, 1978. URL http://adsabs.harvard.edu/abs/1978ApJ...225..357S. (Cited on page 18.)

Shapley, H. 'Studies based on the colors and magnitudes in stellar clusters. VI. On the determination of the distances of globular clusters.' *ApJ*, 48:89, 1918. URL http://adsabs.harvard.edu/abs/1918ApJ....48...89S. (Cited on page 4.)

Sharma, S. et al. 'Galaxia: a code to generate a synthetic survey of the Milky Way'. *ApJ*, 730(1):3, 2011. URL http://stacks.iop.org/0004-637X/730/i=1/a=3?key=crossref.f2db9878c69921e214d4c640e39923e9. (Cited on pages xvi and 42.)

Shen, J. et al. 'Our Milky Way as a pure-disk galaxy—a challenge for Galaxy formation'. *ApJ*, 720(1):L72–L76, 2010. URL http://adsabs.harvard.edu/abs/2010ApJ...720L..72S. (Cited on page 16.)

Simon, J. D. and Geha, M. 'The Kinematics of the Ultra-faint Milky Way Satellites: Solving the Missing Satellite Problem'. *ApJ*, 670(1):313–331, 2007. URL http://adsabs.harvard.edu/abs/2007ApJ...670..313S. (Cited on page 6.)

Sion, E. M. et al. 'The white dwarfs within 25 pc of the Sun: kinematics and spectroscopic subtypes'. *AJ*, 147(6):129, 2014. URL http://stacks.iop.org/1538-3881/147/i=6/a=129?key=crossref.d86feb053bde4fc72b3cf812a3c5f3bd. (Cited on page 57.)

Skrutskie, M. F. et al. 'The Two Micron All Sky Survey (2MASS)'. *AJ*, 131(2):1163–1183, 2006. URL http://adsabs.harvard.edu/abs/2006AJ....131.1163S. (Cited on page xv.)

Slipher, V. M. 'Nebulae'. *Proc. Am. Philos. Soc.*, 56, 1917. URL http://adsabs.harvard.edu/abs/1917PAPhS..56..403S. (Cited on page 4.)

Smoot, G. F. et al. 'Structure in the COBE differential microwave radiometer first-year maps'. *ApJ*, 396:L1, 1992. URL http://adsabs.harvard.edu/abs/1992ApJ...396L...1S. (Cited on page 5.)

Soubiran, C. et al. 'Vertical distribution of Galactic disk stars'. *A&A*, 480(1):91–101, 2008. URL http://adsabs.harvard.edu/abs/2008A%26A...480...91S. (Cited on page 18.)

Sparke, L. and Gallagher, J. *Galaxies in the Universe: An Introduction* (CUP, 2007). URL http://adsabs.harvard.edu/abs/2007gitu.book.....S. (Cited on page 14.)

Springel, V. et al. 'Simulations of the formation, evolution and clustering of galaxies and quasars.' *Nature*, 435(7042):629–36, 2005. URL http://adsabs.harvard.edu/abs/2005Natur.435..629S. (Cited on page 18.)

Steinmetz, M. et al. 'The Radial Velocity Experiment (RAVE): First Data Release'. *AJ*, 132(4):1645–1668, 2006. URL http://adsabs.harvard.edu/abs/2006AJ....132.1645S. (Cited on pages xvii and 19.)

Stinson, G. S. et al. 'Cosmological galaxy formation simulations using smoothed particle hydrodynamics'. *MNRAS*, 408(2):812–826, 2010. URL http://adsabs.harvard.edu/abs/2010MNRAS.408..812S. (Cited on page 19.)

Sunyaev, R. A. and Zeldovich, Y. B. 'Small-Scale Fluctuations of Relic Radiation'. *Ap&SS*, 7(1), 1970. URL http://adsabs.harvard.edu/abs/1970Ap%26SS...7....3S. (Cited on page 5.)

Trumpler, R. and Weaver, H. 'Statistical astronomy'. *Dover Books Astron. Sp. Top.*, 1953. URL http://adsabs.harvard.edu/abs/1953stas.book.....T. (Cited on page 36.)

Trumpler, R. J. 'Preliminary results on the distances, dimensions and space distribution of open star clusters'. *LicOB*, 14:154–188, 1930. URL http://adsabs.harvard.edu/abs/1930LicOB..14..154T. (Cited on page 15.)

van den Bergh, S. 'The frequency of stars with different metal abundances.' *AJ*, 67:486, 1962. URL http://adsabs.harvard.edu/abs/1962AJ.....67..486V. (Cited on page 69.)

van den Bergh, S. and Sher, D. 'The luminosity functions of galactic star clusters'. *PDDO*, 2:203–251, 1960. URL http://adsabs.harvard.edu/abs/1960PDDO....2..203V. (Cited on page 41.)

van der Walt, S., Colbert, S. C. and Varoquaux, G. 'The NumPy Array: A Structure for Efficient Numerical Computation'. *Comput. Sci. Eng.*, 13(2):22–30, 2011. URL http://ieeexplore.ieee.org/lpdocs/epic03/wrapper.htm?arnumber=5725236. (Cited on page 75.)

van Dokkum, P. G. and Conroy, C. 'The Stellar Initial Mass Function in Early-Type Galaxies From Absorption Line Spectroscopy. I. Data and Empirical Trends'. *ApJ*, 760(1):70, 2012. URL http://iopscience.iop.org/0004-637X/760/1/70/article/. (Cited on page 64.)

van Dokkum, P. G. et al. 'The assembly of Milky-Way-like galaxies since z $\sim$ 2.5'. *ApJ*, 771(2):L35, 2013. URL http://adsabs.harvard.edu/abs/2013ApJ...771L..35V. (Cited on pages 18 and 41.)

van Leeuwen, F. 'Validation of the new Hipparcos reduction'. *A&A*, 474(2):653–664, 2007. URL http://www.nature.com/doifinder/10.1038/sj.onc.1200821. (Cited on pages xvi, 42, and 47.)

Vergely, J.-L. et al. 'The interstellar extinction in the solar neighbourhood. I. Statistical approach'. *A&A*, 340:543–555, 1998. URL http://adsabs.harvard.edu/abs/1998A&A...340..543V. (Cited on pages 34 and 48.)

Vogelsberger, M. et al. 'A model for cosmological simulations of galaxy formation physics'. *MNRAS*, 436(4):3031–3067, 2013. URL http://mnras.oxfordjournals.org/cgi/doi/10.1093/mnras/stt1789. (Cited on page 64.)

Vogelsberger, M. et al. 'Introducing the Illustris Project: simulating the coevolution of dark and visible matter in the Universe'. *MNRAS*, 444(2):1518–1547, 2014. URL http://adsabs.harvard.edu/abs/2014MNRAS.444.1518V. (Cited on page 18.)

von Weizsäcker, C. F. 'Über Elementumwandlungen im Innern der Sterne. I (Transformation of the elements in the interior of stars. I)'. *Phys. Zeitschrift*, 38:176–191, 1937. (Cited on page 7.)

Walker, A. G. 'On the formal comparison of Milne's kinematical system with the systems of general relativity'. *MNRAS*, 95, 1935. URL http://adsabs.harvard.edu/abs/1935MNRAS..95..263W. (Cited on page 4.)

Wang, J. et al. 'The missing massive satellites of the Milky Way'. *MNRAS*, 424(4):2715–2721, 2012. URL http://adsabs.harvard.edu/abs/2012MNRAS.424.2715W. (Cited on page 6.)

Wegg, C., Gerhard, O. and Portail, M. 'The structure of the Milky Way's bar outside the bulge'. *MNRAS*, 450(4):4050–4069, 2015. URL http://adsabs.harvard.edu/abs/2015MNRAS.450.4050W. (Cited on page 15.)

Weidner, C. and Kroupa, P. 'The Variation of Integrated Star Initial Mass Functions among Galaxies'. *ApJ*, 625(2):754–762, 2005. URL http://stacks.iop.org/0004-637X/625/i=2/a=754. (Cited on page 41.)

Weinberg, S. *Cosmology* (OUP, 2008). URL http://adsabs.harvard.edu/abs/2008cosm.book....W. (Cited on page 7.)

White, S. D. M. and Rees, M. J. 'Core condensation in heavy halos - A two-stage theory for galaxy formation and clustering'. *MNRAS*, 183:341–358, 1978. URL http://adsabs.harvard.edu/abs/1978MNRAS.183..341W. (Cited on page 18.)

Wielen, R. 'The kinematics and ages of stars in Gliese's catalogue'. *Highlights Astron.*, 3:395–407, 1974. URL http://adsabs.harvard.edu/abs/1974HiA.....3..395W. (Cited on page 57.)

Wielen, R. 'The diffusion of stellar orbits derived from the observed age-dependence of the velocity dispersion'. *A&A*, 60:263–275, 1977. URL http://adsabs.harvard.edu/abs/1977A%26A....60..263W. (Cited on page 18.)

Yanny, B. et al. 'Segue: a spectroscopic survey of 240,000 stars with g = 14-20'. *AJ*, 137(5):4377–4399, 2009. URL http://adsabs.harvard.edu/abs/2009AJ....137.4377Y. (Cited on pages xvii and 17.)

York, D. G. et al. 'The Sloan Digital Sky Survey: Technical Summary'. *AJ*, 120(3):1579–1587, 2000. URL http://stacks.iop.org/1538-3881/120/i=3/a=1579. (Cited on pages xvii, 17, and 41.)

Zasowski, G. et al. 'Target selection for the Apache Point Observatory Galactic Evolution Experiment (APOGEE)'. *AJ*, 146(4):81, 2013. URL http://adsabs.harvard.edu/abs/2013AJ...146...81Z. (Cited on page 77.)

Zoccali, M. et al. ‘Abundances in the Galactic Bulge: evidence for fast chemical enrichment’. *PIAU*, 2(S241), 2007. URL http://adsabs.harvard.edu/abs/2007IAUS..241...73Z. (Cited on page 16.)

Zwicky, F. ‘Die Rotverschiebung von extragalaktischen Nebeln’. *Helv. Phys. Acta*, 6:110–127, 1933. URL http://adsabs.harvard.edu/abs/1933AcHPh...6..110Z. (Cited on page 5.)

COLOPHON

This document was typeset in LaTeXusing a modified version of the typographical look-and-feel *classicthesis* developed by André Miede (GNU GPL).

Plots were created using *matplotlib* together with *inkscape*.